

Universität  
Rostock



Traditio et Innovatio



# Physical and Chemical Characterization of Nanosecond Pulsed Streamer Discharges in Water

**Kumulative Dissertation**

zur Erlangung des akademischen Grades

doctor rerum naturalium  
(Dr. rer. nat.)

am Institut für Physik  
der Mathematisch-Naturwissenschaftlichen Fakultät  
der Universität Rostock

in Kooperation mit dem  
Leibniz-Institut  
für Plasmaforschung und Technologie (INP)

vorgelegt von

Raphael Rataj

im September 2023



**Betreuer:**

Prof. Dr. Jürgen F. Kolb, Universität Rostock, Institut für Physik

**Gutachter:**

Prof. Dr. Jürgen F. Kolb, Universität Rostock, Institut für Physik

Prof. Dr. Andreas A. Neuber, Texas Tech University, Department of Electrical & Computer Engineering

Prof. Ph.D. Zdenko Machala, Comenius University, Department of Environmental Physics

**Dekan:**

Prof. Dr. Klaus Neymeyr, Universität Rostock, Institut für Mathematik

**Datum der Einreichung:**

14. September 2023

**Datum der Verteidigung:**

01. März 2024





““Difficult” takes a few seconds, “impossible” a few minutes.”

RODNEY MCKAY



## Abstract

Pulsed streamer discharges submerged in water are already employed in several applications, e.g. synthesis of platform chemicals, water purification, and functionalization of nanoparticle-surfaces. The underlying mechanisms commonly are related to the chemistry that is induced by the discharges and can be characterized by the hydrogen peroxide production. Accordingly, the production of hydrogen peroxide has been studied in a variety of experiments and has been found to depend primarily on the pulse parameters, e.g. pulse duration, pulse amplitude and pulse steepness, as well as the conductivity of the water. While the relation between discharge development, pulse parameters and induced chemistry has been extensively investigated for longer pulse durations, i.e. in the range of microseconds to seconds, there is still disagreement for pulse durations in the nanosecond range. Therefore, the objective of this work is to characterize the discharge development for pulse durations in the range of a few hundred nanoseconds and to correlate it with the generation of hydrogen peroxide.

A system for generating pulsed streamer discharges with positive polarity was constructed. Pulses with a duration of (100-300) ns, an amplitude of (50-64) kV, and three different rise and fall times between (19-35) ns and (20-43) ns were applied to a needle-to-plate geometry submerged in water. For conductivities in the range of (1-280)  $\mu\text{S}\cdot\text{cm}^{-1}$ , electro-optical, i.e. monitoring voltage, current, light intensity and imaging with a fast framing ICCD, and electrochemical single-discharge diagnostics were used to investigate discharge development and hydrogen peroxide production.

The discharge onset was statistically studied and found to be closely related to the pulse shape. Afterwards, for the rest of the pulse duration, the filaments of the discharge propagated with a constant velocity of  $30\text{ km}\cdot\text{s}^{-1}$ , which was independent of pulse amplitude and pulse steepness. During the trailing edge of the voltage pulse, the discharge initially decayed prior to the onset of reillumination, a phenomenon in which the preexisting discharge channels are again traversed by an ionization front. For the steepest pulses, reillumination occurred simultaneously, while, for the longest fall times, the previously formed filaments were ignited subsequently. This process was used to determine the charge of the streamer heads, based on which a single streamer model could be developed to describe the propagation of discharge combining the highly filamentous structure in a single streamer.

The hydrogen peroxide production of the discharges was initially studied accumulated for several hundred discharges for the different pulse parameters. In the investigated range of parameter, the production rate increased with higher pulse amplitude, which was attributed to a larger number of filaments of the discharges. Discharges initiated by shorter pulses produced hydrogen peroxide with higher rate and efficiency, which was also the highest efficiency observed in this study with  $9.2\text{ g}\cdot\text{kWh}^{-1}$ . Early stopping of the filaments during the propagation phase and resistive losses in longer filaments were identified as reasons for the reduced production rate and lower efficiency for longer pulse durations.

In water with increased conductivity, hydrogen peroxide production could be studied for individual discharges. With increasing propagation time, the amount of hydrogen peroxide increased quadratically and was not affected by the conductivity. Hence, for the considered conductivities, it was concluded that the observed higher energy dissipation was associated with resistive losses in the liquid and was correlated to the dielectric time constant.



# Inhaltsverzeichnis

<b>1 Motivation and Background</b>	<b>1</b>
1.1 Streamer Discharges in Gas and Water . . . . .	2
1.2 Microsecond versus Nanosecond Pulsed Discharges . . . . .	4
1.3 Chemistry Induced by Discharges in Water . . . . .	6
1.4 Scope of this Work . . . . .	7
<b>2 Temporal Development of Pulsed Discharges in Water (A1-A2)</b>	<b>9</b>
2.1 Experimental Setup . . . . .	9
2.2 Discharge Inception Statistics . . . . .	12
2.3 Streamer Propagation . . . . .	14
2.4 Channel Reillumination . . . . .	17
2.5 Single Streamer Propagation Model . . . . .	21
<b>3 Hydrogen Peroxide Production of Nanosecond Pulsed Discharges (A2-A3)</b>	<b>25</b>
3.1 Flow Injection Analysis with Chronoamperometry . . . . .	26
3.2 Hydrogen Peroxide Production Rate and Efficiency . . . . .	27
3.3 Peroxide Production of Individual Discharges . . . . .	30
<b>4 Summary and Outlook</b>	<b>35</b>
<b>Bibliography</b>	<b>36</b>
<b>Original Publications</b>	<b>43</b>
Article 1 . . . . .	45
Article 2 . . . . .	61
Article 3 . . . . .	77
<b>Publications and Conference Contributions</b>	<b>87</b>
<b>Appendix</b>	<b>91</b>
A1 Precision sharpening of tungsten needles . . . . .	91
A2 Determine streamer lengths from ICCD images and 2D mapping error . . . . .	93
A3 Calibration method of the electrochemical hydrogenperoxide measurement . . . . .	96
<b>Curriculum Vitae</b>	<b>99</b>
<b>Statutory Declaration</b>	<b>101</b>
<b>Acknowledgment</b>	<b>103</b>



# Abbreviations

$\cdot\text{H}$       Hydrogen radical  
 $\cdot\text{O}$       Oxygen radical  
 $\cdot\text{OH}$      Hydroxyl radical  
 $\cdot\text{OOH}$    Hydrogen superoxide radical

FWHM    Full width at half maximum

$\text{H}_2$       Hydrogen molecule  
 $\text{H}_2\text{O}$      Water  
 $\text{H}_2\text{O}_2$    Hydrogen peroxide

$\text{O}_2$       Oxygen molecule





# Symbols

$\alpha$	First Townsend ionization coefficient
$\mu$	Dobrynin ionization coefficient
$\phi$	Angular coordinate describing a position relative to needle axis and tip location
$\delta$	Infinitesimal time step
$\tau$	Dielectric time constant
$\sigma$	Conductivity
$\Delta t$	Time of discharge propagation
$A_s$	Cross-sectional area of a streamer
$C$	Capacitance of a discharge
$C_i$	Capacitance of an individual streamer head
$E$	Electric field strength
$E_{\text{ex}}$	External electrical field, i.e. field between needle and plate electrodes without discharge
$I$	Discharge current
$I_L$	Emitted light intensities
$L_s$	Streamer length
$R$	Universal gas constant
$R_s$	Streamer radius
$T$	Temperature
$U_{\text{head}}$	Streamer head potential
$U_{\text{mean}}$	Mean pulse amplitude
$U_{\text{needle}}$	Needle electrode potential
$a_E$	Proportionality constant between streamer radius and external electric field
$b$	Proportionality constant between streamer head charge and length
$d$	Distance between electrodes
$i_e$	Electron current originating at the streamer head
$k$	Production rate of hydrogen peroxide
$k_1$	Rate coefficient of water to hydroxyl radicals by collisions
$k_2$	Rate coefficient of hydrogen peroxide by the combination of two hydroxyl radicals
$k_{\text{OH}}$	Production rate of hydroxyl radicals
$n$	Particle density
$n_{\text{H}_2\text{O}_2}$	Amount of hydroxyl radicals

## *Symbols*

---

$n_{\text{OH}}$	Amount of hydroxyl radicals
$n_{\text{head}}$	Space charge density forming the streamer head
$q$	Streamer head charge
$q_r$	Charge transferred during reillumination
$r$	Radial coordinate originating at the needle tip
$r_n$	Tip curvature radius of the needle electrode
$t$	Time variable
$t_{\text{fall}}$	Pulse fall time (90 % to 10 % of the maximum pulse amplitude)
$t_{\text{min}}$	Time of minimum light emission and current inversion before reillumination
$t_{\text{pulse}}$	Pulse duration
$t_{\text{rise}}$	Pulse rise time (10 % to 90 % of the maximum pulse amplitude)
$t_{\text{start}}$	Time of discharge initiation
$v_s$	Streamer propagation velocity
$z$	Coordinate along needle axis

# 1 Motivation and Background

Pulsed discharges in water have been extensively studied for more than a century and several applications have been developed during this time. For example, it is possible to create functionalized nanoparticles from precursors that can be used as photocatalysts or electrode material in batteries [1–3]. Discharges in water are also applied to the treatment of algae suspensions, where shock waves destroy the cell wall of microorganisms, releasing valuable substances [4, 5]. The disruptive properties of discharges in water are also advantageous for the sustainable production of platform chemicals from organic matter [6, 7]. Finally, the combination of physical and chemical properties of such discharges can be utilized to degrade toxic pollutants for water treatment technologies [8–12].

Particularly, pulsed streamer discharges were studied extensively for applications in recent decades. For instance, the degradation of contaminants by such discharges in surface water or wastewater has made significant progress. It has been shown that streamer discharges effectively dissociate naturally occurring organic compounds such as cylindrospermopsin, which pose a health hazard in drinking water supplies [13–15]. Also, anthropogenic contaminants such as pharmaceutical residues or pesticides have been mineralized, potentially eliminating their environmental threat [12, 16–19].

In addition to an effective degradation, treatment methods based on pulsed streamer discharges in water have the advantage that no additional and possibly toxic chemicals are required, which would necessitate additional purification of the treated water, thus making discharge technologies environmentally friendly. Chemically active species, e.g.  $\cdot\text{OH}$ ,  $\cdot\text{H}$ ,  $\cdot\text{O}$ ,  $\cdot\text{OOH}$ ,  $\text{H}_2\text{O}_2$ , etc., are generated directly in the contaminated solution. In addition, physical effects of the discharges, such as UV radiation, temperature, electric fields, and shock waves, promote the degradation of pollutants. Due to the number of possible treatment pathways, extensive studies have been conducted to characterize the chemical and physical properties of pulsed streamer discharges in water [18–29]. However, it remains unknown how the pulse characteristics affect the discharge physics and chemistry, and how differences in the discharge physics alter the induced chemistry.

For this reason, this thesis first describes general properties of discharges in water in Sections 1.1 to 1.3, from which the thesis scope and structure are motivated in Section 1.4. Secondly, detailed findings on the development of positive streamer discharges for pulses with durations in the order of 100 ns are presented in Chapter 2 and, afterwards, associated with discharge chemistry, which is evaluated by the production of hydrogen peroxide in Chapter 3. Finally, the results are summarized and a recommendation for further research is provided in Chapter 4.

## 1.1 Streamer Discharges in Gas and Water

A streamer discharge is an electrically driven plasma formed, i.e. ignited, by a sufficiently strong primary electron avalanche, i.e. the electrons multiply to such an extent that the resulting space charge generates secondary avalanches. For that, the space charge must alter its surrounding electric field to locally exceed the breakdown field strength. Newly formed electrons drift faster than corresponding positive ions, so the charge carriers separate and maintain the space charge. As a result, an ionization front propagates through the neutral medium in the wake of its secondary electron avalanches. The tail of the ionized but electrically quasi-neutral plasma is called the filament/streamer channel, and the space charge is called its streamer head. During propagation, a streamer can branch which results in several streamer heads and a characteristic filamentous morphology [30–34].

For asymmetric electrode configurations, i.e. configurations with a highly inhomogeneous electric field such as needles or razor edges, two different types of streamer discharges can be observed. When the streamer head propagates away from a negatively charged electrode, it is called a negative or anode-directed streamer. The streamer head is negatively charged and propagation is mainly based on electron impact ionization in the vicinity of the space charge. As a result, negative streamers have a lower propagation velocity and wider filaments [34]. If the streamer originates from an electrode of positive polarity, it is called a positive or cathode-directed streamer. Electrons are mainly generated by photoionization of atoms and molecules in the direction of propagation. Since the ionization cross section of

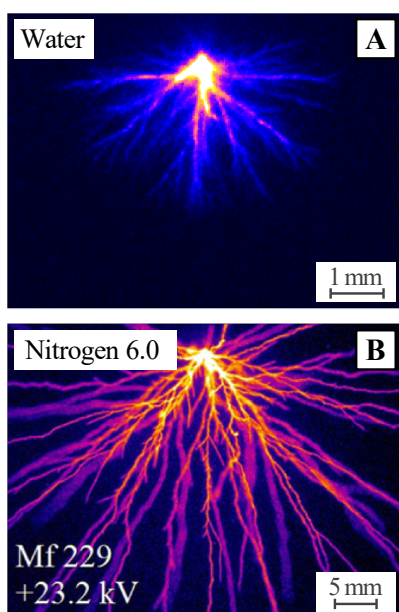


**Abbildung 1.1:** Streamer discharges ignited with nanosecond pulses at the positive electrode in pure nitrogen (panel A) and deionized water (panel B) at atmospheric pressure. Panel B reprinted from [35].

photons is usually smaller than that of electrons, the propagation velocities of positive streamers are higher and the channels are thinner than their negative counterparts [30, 34].

This description applies to both liquid and gaseous media. In fact, they share a common history, as both phenomena were described at about the same time [36] and some scientific advances in one medium were transferable to the other. This is evident when comparing exemplary discharges for both media. Figure 1.1 shows a discharge in water (panel A) and in pure nitrogen (panel B) at atmospheric pressure, instigated by a positive nanosecond high-voltage pulse at a needle electrode [35]. Both discharges show a filamentous morphology, have several branched channels, and propagate in the space between the needle and the counter electrode. Because of this apparent similarity, it is not surprising that a phenomenological description of the discharge development with the Raether-Meek criterion applies in both media (Equation 1.1).

$$\alpha d \geq \text{const} \quad (1.1)$$

Originally, the criterion described whether an electron originating at the high-voltage electrode causes a breakdown

in the gas between the electrodes by relating the ionization coefficient,  $\alpha$ , (ions generated per unit length) to the distance between the electrodes,  $d$ . If  $\alpha d$  is greater than unity, an electron avalanche can be observed, but to obtain a streamer-type discharge,  $\alpha d \geq 20$  must be fully filled [31, 32]. The criterion is also valid in liquids, although it must be corrected by an additional ionization coefficient  $\mu$  that accounts for density variations in the liquid, so the modified criterion is  $(\alpha + \mu)d \geq 20$  [37].

Discharges in liquids are more similar to gas discharges than just in their structural appearance. For example,  $\alpha$  depends on the reduced electric field  $E/n$ , where  $E$  is the electric field strength and  $n$  is the particle density, while  $\alpha$  reduces with increasing  $E/n$ . Consistently, the breakdown voltage for gases and liquids decreases with reducing particle density. Also,  $\alpha$  changes for different ionization processes, e.g. electron impact or photoionization, which can be observed in asymmetric electrode configurations for both liquid and gaseous discharges. When a positive streamer is ignited, long and narrow channels can be observed (mainly photoionization), while shorter, more diffuse filaments are formed with increased inception voltages in negative discharges (mainly electron impact ionization) [21, 30, 33, 34, 36].

However, discharges in gas and liquid also show fundamental differences. Referring again to Figure 1.1, streamer discharges in liquids appear smaller than gas discharges. While filaments in gases reach several centimeters in length and a few hundred micrometers in diameter, liquid discharges are limited to a few millimeters in length and tens of micrometers in width [20, 21, 35–51]. This is associated with a smaller propagation velocity, which is of the order of  $10 \text{ km}\cdot\text{s}^{-1}$  in liquids and  $1000 \text{ km}\cdot\text{s}^{-1}$  in gases [38–41, 44, 45, 47, 49]. Due to the increased particle density in liquids, an increased electron density of up to  $10^{19} \text{ cm}^{-3}$  is reached in liquid discharge channels compared to densities in the order of  $10^{14} \text{ cm}^{-3}$  electrons in typical gas discharges [20, 21, 36, 38, 40–46, 51–53].

In addition, liquids have unique characteristics that affect discharges which are not relevant in gases, namely density fluctuations, high dielectric constants, lower ion mobilities and higher electrical conductivities. Density fluctuations, e.g. bubbles of dissolved gas, not only change the electric field in the electrode gap, but also lead to branching of the discharge filaments and deviation of the propagation direction [54]. Also, the density and dielectric constant of a dielectric liquid, i.e. liquids with relatively high dielectric constants such as water, are related to the electric field. Ponderomotive force and Joule heating create regions of low density, which decrease the dielectric “constant” of a liquid. Strong and inhomogeneous electric fields have the same effect [11, 54–57, 57–62]. The conductivity of a liquid is another parameter that changes the electric field, as dissolved ions in the liquid can shield the electrodes and the propagating streamer. Whether such shielding is significant depends on the concentration and mobility of the ions, which in itself is relevant for ion propagation within a streamer. Finally, the particle density, electric field, conductivity and ion mobility lead to unique phenomena in discharges in liquids, such as reillumination (see Section 1.2) [37, 44, 45, 47–50, 63].

This thesis focuses on streamer discharges generated by positive high-voltage pulses in water in a needle-to-plate geometry at atmospheric pressure. This choice is motivated, as several effective water treatment applications were developed using positive streamer discharges and because the needle-to-plate geometry is best suited for optical investigations. It is known from the literature that pulse duration has a fundamental influence on discharge characteristics. Hence, a brief review of the influence of pulse duration on the discharges seems appropriate.

## 1.2 Microsecond versus Nanosecond Pulsed Discharges

The development of positive, pulsed streamer discharges in water can be divided into four phases: inception, propagation, decay, and post-discharge [48]. As shown schematically in Figure 1.2, streamer inception summarizes the mechanisms by which a discharge is ignited at the high-voltage needle electrode and subsequently propagates into the medium between the electrode gap. During this phase and due to branching, the characteristically filamentous structure of the discharge is established. When further propagation of the streamer heads is no longer promoted, the filaments begin to decay and several post-discharge phenomena may follow after the decay.

This subdivision can be made independently of a specific high-voltage pulse, but the characteristics of each individual phase are sensitive to pulse parameters such as amplitude, duration, or rise/fall time. For this reason, results that contradict each other were published, even if, for example, the pulse duration is similar in several experiments [36]. The following paragraphs summarize phenomena related to the pulse parameter that are generally accepted.

Discharges initiated during pulses of at least microseconds up to seconds duration, are generally agreed to be ignited by the so-called bubble mechanism. Due to the high particle density, which results in a mean free path of a few nanometers for electrons, and isotropic elastic scattering of electrons in water, which randomizes their propagation direction and thus reduces the possibility to gain ionization energies, a low density region has to form prior to the streamer discharge [21, 36, 58]. There are several different mechanisms that can create such a “bubble” or “crack”. For example, the electric fields of several megavolts per centimeter drive a current in the liquid, which raises the temperature by Joule heating. It has been found that a few microseconds are sufficient to evaporate water in a small cavity at the electrodes under typical experimental conditions. In addition, mechanical stress is created by strong, inhomogeneous electric fields, e.g. Maxwell stress or ponderomotive force, which either create or expand pre-existing low-density regions, but especially for short pulse durations [21, 36, 48, 64].

The generation of usually non-luminous low-density regions is observable by shadowgraphy, and it was shown in experiments with microsecond pulses that a cluster of bubbles appears within 300 ns of the applied voltage, grows within 1  $\mu$ s to a size of about 50  $\mu$ m, and forms protrusions [43, 48]. It was therefore concluded that the bubbles are formed by Joule heating and a gaseous discharge is generated inside the bubble, leading to the formation of needle-like protrusions. However, it also seems plausible that these protrusions are formed by the

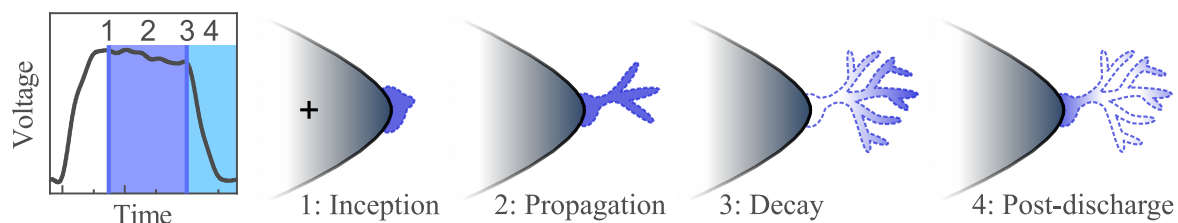


**Abbildung 1.2:** Schematic visualization of a developing streamer discharge instigated during a rectangular high-voltage pulse of nanosecond to microsecond duration.

above-mentioned electromechanical forces, which can elongate small protrusions into needle-like shapes.

At the tip of a single protrusion a filamentary structure forms, which is usually not luminous, but is nevertheless called "primary streamer". These streamers propagate at about  $(2-3) \text{ km}\cdot\text{s}^{-1}$ , reach lengths of up to  $300 \mu\text{m}$ , and are associated with repetitive current pulses in the order of a few tens of milliamperes [48, 65].

A few tens of nanoseconds later, a bright filamentary structure begins to propagate at the tip of a primary streamer, called a "secondary streamer" [21, 36, 43, 48, 65]. This marks the transition to the propagation phase of a discharge in water (cf. Figure 1.2), where several filaments extend. These start at the same time and location with a constant velocity of  $(25-30) \text{ km}\cdot\text{s}^{-1}$ . The channel length therefore increases linearly with time,  $t$ , while a positive current is transferred to the discharge [47, 48, 65]. The channel diameter steadily increases proportional to  $\sqrt{t}$  [43]. During propagation, the filaments bifurcate several times, which is thought to result from density fluctuations in the fluid [36, 54]. Alternatively, it has been suggested that branching is part of a self-regulatory effect that causes the stable propagation velocity [47].

As the voltage pulse decays, the electrode potential decreases and streamer propagation stops, marking the transition to the discharge decay. The light emission decreases to a minimum synchronously with the discharge current. However, for discharges in water, this does not necessarily end the discharge development, as individual channels may reignite if the electrode potential is still sufficient. This process is called "reillumination" (fourth phase in Figure 1.2), which causes positive current spikes associated with light emission, leads to additional filament propagation, and occurs only at low water conductivities [47, 48, 65]. No conclusive explanation for why and how reillumination occurs has been reported, but it has been suggested that it is a result of expanding channel diameters as well as the decreasing temperature, which would decrease the pressure within a filament. In addition, the preionized gas in the filament would lower the voltage threshold for a second discharge along the preexisting channel. However, this explanation still lags, since reignition starts some nanoseconds into the discharge decay. Thus, the expansion of the channel diameter is negligible, which is why the condition for reignition does not seem to be achievable by pressure and temperature alone [43, 66]. Furthermore, within this theoretical framework, it is not possible to explain why increased water conductivity suppresses reignition.

When pulses of tens of nanoseconds instead of microseconds are used to initiate discharges in water, the discharge development is significantly different. To date, no conclusive theory of discharge initiation has been developed. The electric field strength for initiation is at least one order of magnitude higher than for microsecond pulses, ranging from  $15 \text{ MV}\cdot\text{cm}^{-1}$  to  $40 \text{ MV}\cdot\text{cm}^{-1}$  [37, 44, 45, 51–53, 67]. Experimental evidence has been reported for different initiation mechanisms, although it is generally accepted that Joule heating does not contribute significantly due to the short pulse duration. Instead, a low-density region at the positive needle electrode was postulated to be formed by ponderomotive forces, for which experimental evidence was found using shadowgraphy. Several possible shapes of the low-density region are discussed, i.e. a number of nanometer-sized pores, a single shock front, or non-luminous tree-like channels [37, 44, 45, 57, 62, 68–75]. Alternatively, either direct ionization of the liquid or the formation of a micrometer-sized bubble containing supercritical water was observed

and interpreted by a cavitation theory [51–53, 76].

After ignition, experimental results regarding streamer propagation are also inconclusive. On the one hand, it has been reported that streamers propagate only during the rising edge of a voltage pulse with velocities up to  $5000 \text{ km}\cdot\text{s}^{-1}$  and then decay during the pulse plateau [37, 67, 74–77]. On the other hand, a constant propagation with velocities in the range of  $(25\text{--}46) \text{ km}\cdot\text{s}^{-1}$  during the whole pulse duration was observed [44, 45, 52, 53, 76].

There are also inconsistencies in experiments on post-discharge development. Reignition - also called reillumination- of channels was observed, although it was not coherent whether all channels reignite or only individual filaments [37, 45, 53, 67]. In contrast to reignition in microsecond discharges, a negative current is observed during reignition. Controversially, some publications did not report any post-discharge phenomena [74–77]. Thus, the mechanism of reillumination in nanosecond discharges remains unclear.

### 1.3 Chemistry Induced by Discharges in Water

Studies of chemical processes in and induced by discharges in water usually focus on hydrogen peroxide production. Although simulations have shown that other, short-lived species, e.g.  $\cdot\text{O}$ ,  $\cdot\text{OH}$  or  $\cdot\text{OOH}$ , are formed in the discharges, hydrogen peroxide ( $\text{H}_2\text{O}_2$ ) is used as a marker because it is the only long-living molecule in the sample when pure water is used. It decomposes slowly enough to allow accurate measurements and its concentrations can be related to the other species [21, 26, 78].

It was found that increasing pulse amplitude, duration, and repetition frequency resulted in higher hydrogen peroxide concentrations, while increasing the electrode gap decreased peroxide production. Changing the pH and electrode geometry had no effect [18, 23, 25, 29, 78–83]. As most applications ignite discharges in water with various additives, water conductivity is likely the most interesting parameter for the investigation of the discharge chemistry. However, studies have not yet yielded conclusive results. Investigations observing an increasing, decreasing or non-monotonically changing  $\text{H}_2\text{O}_2$  concentrations with increasing conductivities have been reported [16, 24–26, 84–86]. Interestingly, when comparing the energy efficiency of nanosecond and microsecond discharges, shorter discharges with  $2 \text{ g}\cdot\text{kWh}^{-1}$  are twice as efficient as long discharges with ca.  $1 \text{ g}\cdot\text{kWh}^{-1}$  [21, 29].

For each pulse parameter, a possible mechanism has been proposed for how hydrogen peroxide production is affected. For example, an increased amplitude should increase the power density within a streamer, thereby increasing the local temperature, which would lead to increased  $\text{H}_2\text{O}_2$  production [23, 79]. A longer pulse duration increases the length of the filaments and the total energy dissipated in the discharge, also increasing the  $\text{H}_2\text{O}_2$  production [16]. A larger gap reduces the electric field, which effectively corresponds to a lower pulse amplitude and therefore reduces the yield of hydrogen peroxide. However, a major challenge remains to experimentally correlate individual physical discharge characteristics, such as streamer length, time delay, or dissipated energy, with chemical species production, because studies typically measure  $\text{H}_2\text{O}_2$  production from multiple discharges and average the production characteristics of individual discharges. However, each additional discharge affects previously produced hydrogen peroxide molecules, as emitted UV radiation and metal ions eroded from



the electrodes potentially dissociate  $\text{H}_2\text{O}_2$  [25, 26]. Finally, in commonly used capacitance-based pulsed power systems, pulse parameters such as amplitude, duration, and steepness cannot be varied individually and are affected by load characteristics, i.e. conductivity of the liquid or interelectrode distance [16, 24, 25]. For example, increasing conductivity lowers the impedance of such a discharge system and thus shortens the pulse duration while increasing the steepness of the falling pulse edge. Therefore, it is not possible to disentangle the influence of conductivity, pulse duration or pulse steepness on hydrogen peroxide production in these systems.

## 1.4 Scope of this Work

The primary objective of this thesis is to correlate the characteristics of the development of pulsed streamer discharges in water with the chemistry they induce in the liquid. In particular, the study focuses on positive pulsed streamer discharges in water initiated at a needle electrode by high-voltage pulses in the range of (100-300) ns. Pulses of positive polarity, which induce streamer discharges and no breakdown, were chosen because they are preferred for the majority of applications. The discharges could be ignited reproducibly at the same location in a needle-to-plate electrode geometry, which makes this configuration most suitable for optical analysis of the discharge development. The range of pulse durations was selected because it is intermediate between the better understood microsecond discharges and the controversially discussed nanosecond discharges.

The results are structured as shown in Figure 1.4. First, a pulsed power system was configured to allow precise adjustment of each pulse parameter and diagnostic of individual discharges

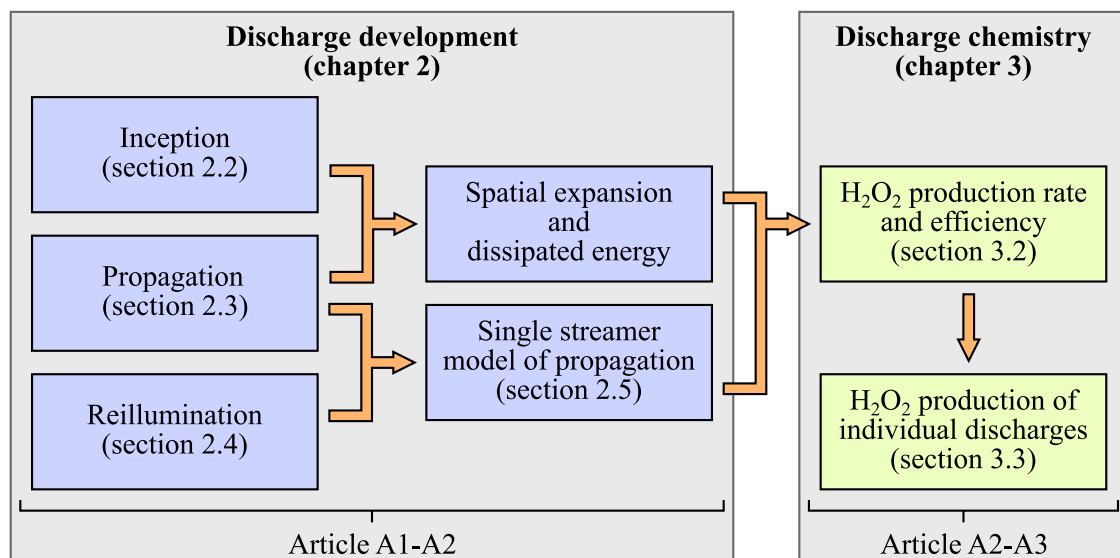


Abbildung 1.3: Structure of this thesis.

(cf. Section 2.1). Presented in Sections 2.2-2.4, the discharge inception, propagation, and reillumination were observed with respect to the open research questions presented in Section 1.2 to clarify the inception behavior, to specify the propagation velocity, to observe the discharge morphology, and to detail the discharge decay, i.e. filament stopping and reillumination. A theoretical model of streamer propagation was derived to explain the observations of the discharge development (cf. Section 2.5). The results of these sections, in particular the information on energy dissipation and spatial expansion, were then related to the hydrogen peroxide production of the discharges.

A novel electrochemical method for analyzing hydrogen peroxide concentrations in the range of nanomoles per liter was developed, which is described in Section 3.1. Hydrogen peroxide production for each pulse parameter was determined and associated with the results of Chapter 2, thereby identifying correlations between discharge development and induced chemistry and explaining effects on  $\text{H}_2\text{O}_2$  production rate and efficiency (cf. Section 3.2). Special emphasis was placed on the influence of the conductivity of the liquid on hydrogen peroxide production. Therefore, the amount of  $\text{H}_2\text{O}_2$  formed by single discharges was determined for different conductivities and explained in terms of discharge expansion, energy dissipation and the theoretical model for streamer propagation (cf. Section 3.3).

Finally, the results of this work were summarized in Chapter 4 and an outlook for further research was provided.

## 2 Temporal Development of Pulsed Discharges in Water (A1-A2)

In order to integrate 100 ns and 300 ns discharges into the general scheme of micro- and nanosecond pulsed discharges, and in particular to identify typical characteristics, an in-depth study of discharge initiation, propagation and reignition with respect to the main pulse parameters, i.e. amplitude, duration and steepness, is necessary. This requires a precisely controllable pulsed power system, electrical and optical diagnostics, and automated data analysis for individual discharges. In the past, the pulsed power system has been a major obstacle, as most system designs did not allow individual control of the pulse parameters, resulting in either cross-correlations or a reduced range of possible parameters in previous studies.

Therefore, within the framework of this thesis, a pulse generator based on a Blumlein-line design was developed, which was capable of generating high-voltage pulses with a low repetition frequency, but with individual control of the pulse parameters. The resulting setup is described in Section 2.1, but in short, the pulsed power system was coupled with optical and electrical diagnostics to observe individual discharge events. The discharge development was then characterized chronologically: First, a statistical study of discharge inception (cf. Section 2.2) was performed. Second, the subsequent discharge propagation was observed to measure the propagation time, to clarify the existence of a dark phase, and to determine a filament stopping length (cf. Section 2.3). Finally, the decay phase of the discharges was recorded to characterize reillumination effects (cf. Section 2.4). The observations were then used to develop a theoretical model to explain reillumination based on streamer propagation (cf. Section 2.5).

### 2.1 Experimental Setup

A schematic overview of the experimental setup consisting of discharge chamber, pulse generator and electrical as well as optical diagnostics is given in Figure 2.1. For all experiments published in Article 1 to Article 3, an insulated tungsten needle was used as positive electrode, which was electrochemically sharpened to a tip radius,  $r_n$ , of (35-40)  $\mu\text{m}$  and resharpener after no more than 1000 discharges. At a gap distance,  $d$ , ranging from 5 mm to 14 mm, the plane titanium counter-electrode with a diameter of 46 mm was located. Both electrodes were mounted, if not stated otherwise, in a polymethylmethacrylate chamber with a volume of 100 ml and three quartz glass windows. The chamber was completely filled with water, which was circulated with a flow of  $120 \text{ ml}\cdot\text{min}^{-1}$ . Specifically, experiments described in Article 1 and Article 2 were conducted with deionized water, while sodium chloride was added for experiments reported in Article 3. A  $250 \Omega$  resistor in parallel with both electrodes completed the discharge chamber so that the chamber resistance was adjusted to approximately  $245 \Omega$ ,

which matched the pulse generator.

A custom-built stacked Blumlein-line generator was used to apply rectangular pulses with a repetition frequency of 1 Hz, an amplitude,  $U_{\text{mean}}$ , of (50-64) kV, and a duration,  $t_{\text{pulse}}$ , of either 100 ns or 300 ns (FWHM, see Figure 2.1(A)). Due to an adjustable inductance of the generator's spark gap switch, the rise time,  $t_{\text{rise}}$ , and fall time,  $t_{\text{fall}}$ , could be set between (16-35) ns and (20-43) ns, respectively. Due to the matched resistance of chamber and pulse generator, no reflections were observed, though amplitudes dropped into the negative, reaching about -20% of the maximum applied amplitude. This was a result of the parasitic impedances of the waveguide shielding. A trigger signal was derived at the spark gap, and for 100 ns pulses, a delay line was connected between the generator and the plasma chamber to increase the trigger time to 177 ns.

Since the output connectors of the pulse generator were not intentionally grounded, both electrodes were biased with a high electrical potential. Hence, two calibrated passive voltage probes (P6015A, 70 MHz, *Tektronix*) differentially measured the pulse amplitudes applied to the electrode gap and a Rogowski coil (CT-E2.5, 500 MHz, *Magnelab*) monitored the current at the counter electrode. An oscilloscope (WaveSurfer 10, 1 GHz, LeCroy) recorded all synchronized signals.

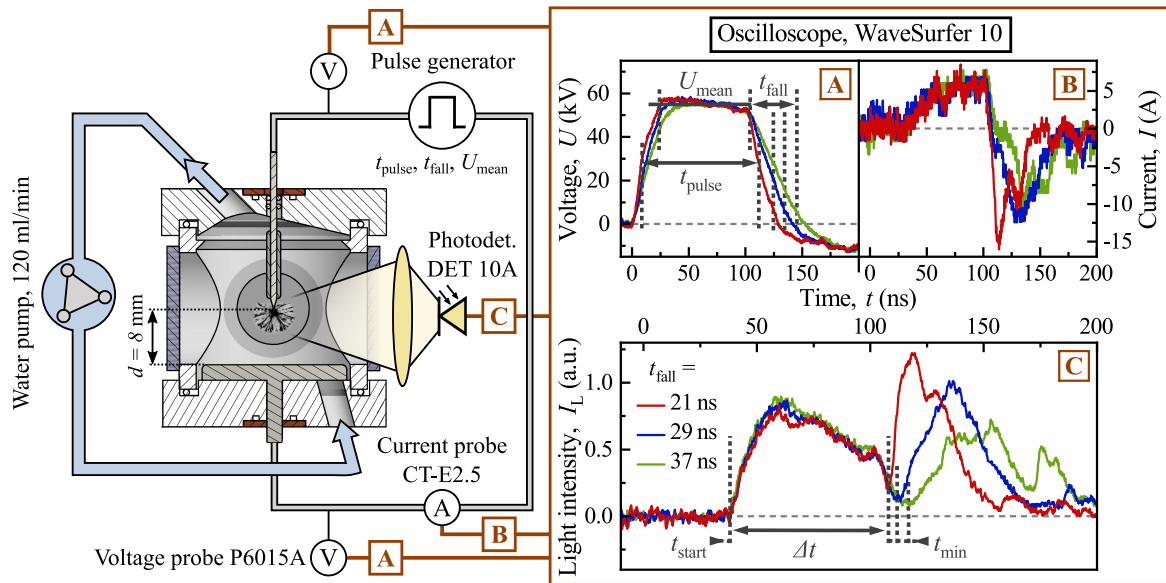


**Abbildung 2.1:** Schematic of the experimental setup, consisting of discharge chamber, pulse generator and diagnostics. Discharges were ignited in a needle-to-plate electrode configuration (submerged in water) with an interelectrode distance,  $d$ , and instigated by high-voltage pulses provided by a Blumlein line generator. Deionized water was circulated through the system by a peristaltic pump. Pulse amplitude,  $U_{\text{mean}}$ , pulse duration,  $t_{\text{pulse}}$ , pulse rise time,  $t_{\text{rise}}$ , and fall time,  $t_{\text{fall}}$ , were recorded in a differential measurement with two high-voltage probes (A), a Rogowski coil (B), and a photodetector (C). Typical signals for voltage (Panel (A)), discharge current (Panel (B)) and emitted light intensity (Panel (C)) are shown for pulse steepnesses characterized by fall times of 21 ns, 29 ns and 37 ns. Images of every discharge event were recorded with an ICCD camera. Reprinted from Article 2.

Light emission was detected by a photodetector (DET 10A, *ThorLabs*) with a temporal resolution of 1 ns, and images were recorded by two different cameras. A fast framing camera (SIM D8, *Specialised Imaging Ltd.*) was able to take three images in short succession (minimum delay of 0 ns) with a minimum gate width of 3 ns, so multiple fast-gated images could be obtained from an individual discharge event, which was mainly used for the experiments described in Article 1. For the investigations reported in Article 2 and Article 3, an ICCD (4Picos, *Stanford Computer Optics*) was used to obtain time-integrated images of single discharges, hence a gate width of 200 ns and 600 ns was set for 100 ns and 300 ns pulses, respectively.

Typical measurements of discharge currents,  $I$ , for 100 ns pulses with fall times of 21 ns, 29 ns, and 37 ns are shown in Figure 2.1(B). Noticeably, the signals were corrected and no longer contain the displacement currents normally associated with pulsed voltages, which are about an order of magnitude larger. For the correction, fifty pulses were applied with reduced amplitude so that no discharge was initiated, the voltage and current signals were averaged as a reference signal, an amplitude scaling factor was calculated from the discharge pulse amplitude and the reference, and finally the scaled reference current was subtracted from each measured current signal to obtain the discharge current. In general, the resulting current started to increase during the application of high-voltages, but never earlier than 15 ns after the pulse started. The currents increased to about 6 A within 30 ns and, with the end of the voltage pulse, the currents decreased to a minimum with reversed polarity while the potential at the needle electrode was still positive. The minima were more pronounced and narrower for shorter fall times and longer pulse durations, while longer fall times resulted in shallower minima.

The light intensity signals,  $I_L$ , are shown in Figure 2.1(C). Similar to the current measurement, the signals were corrected by a reference measurement recorded in parallel to the current reference with an additional screen to block the optical path between the needle tip and the photodetector. This correction was necessary because the spark gap switch, the waveguides, and the discharge chamber emitted considerable electromagnetic noise that was coupled into the photodetector. Fortunately, this noise was linearly dependent on the pulse amplitude, thus allowing for the subtraction of a reference signal.

Closely related to the current development, light intensities began to increase as soon as discharge currents were observed, defining the start time of a luminous discharge,  $t_{\text{start}}$ . The intensities rose to a maximum within 20 ns, after which the intensity gradually decreased, showing the same oscillations as voltage and current. At the time when the currents reversed polarity,  $t_{\text{min}}$ , the light intensities reached a minimum and then rose rapidly to a maximum synchronized with the current minima. As the fall time increased, the light intensity maxima became shallower, wider, and more localized.

By combining signals of current and light intensity, the discharge development was divided into two phases. The propagation phase included the discharge initiation and development up to  $t_{\text{min}}$ , while the reillumination phase included all subsequent phenomena (cf. Section 2.4). This denomination is motivated by the voltage pulse, as the discharge was expected to propagate after ignition during the highest applied potentials, while a reillumination usually occurs during the trailing edge of the pulses. Accordingly, the discharge propagation time,  $\Delta t$ , was defined as the time between  $t_{\text{start}}$  and  $t_{\text{min}}$ .

## 2.2 Discharge Inception Statistics

The start of discharge propagation is marked by its inception, which was defined as the time of first light emission and increasing discharge current flow. Figure 2.2 shows a probability

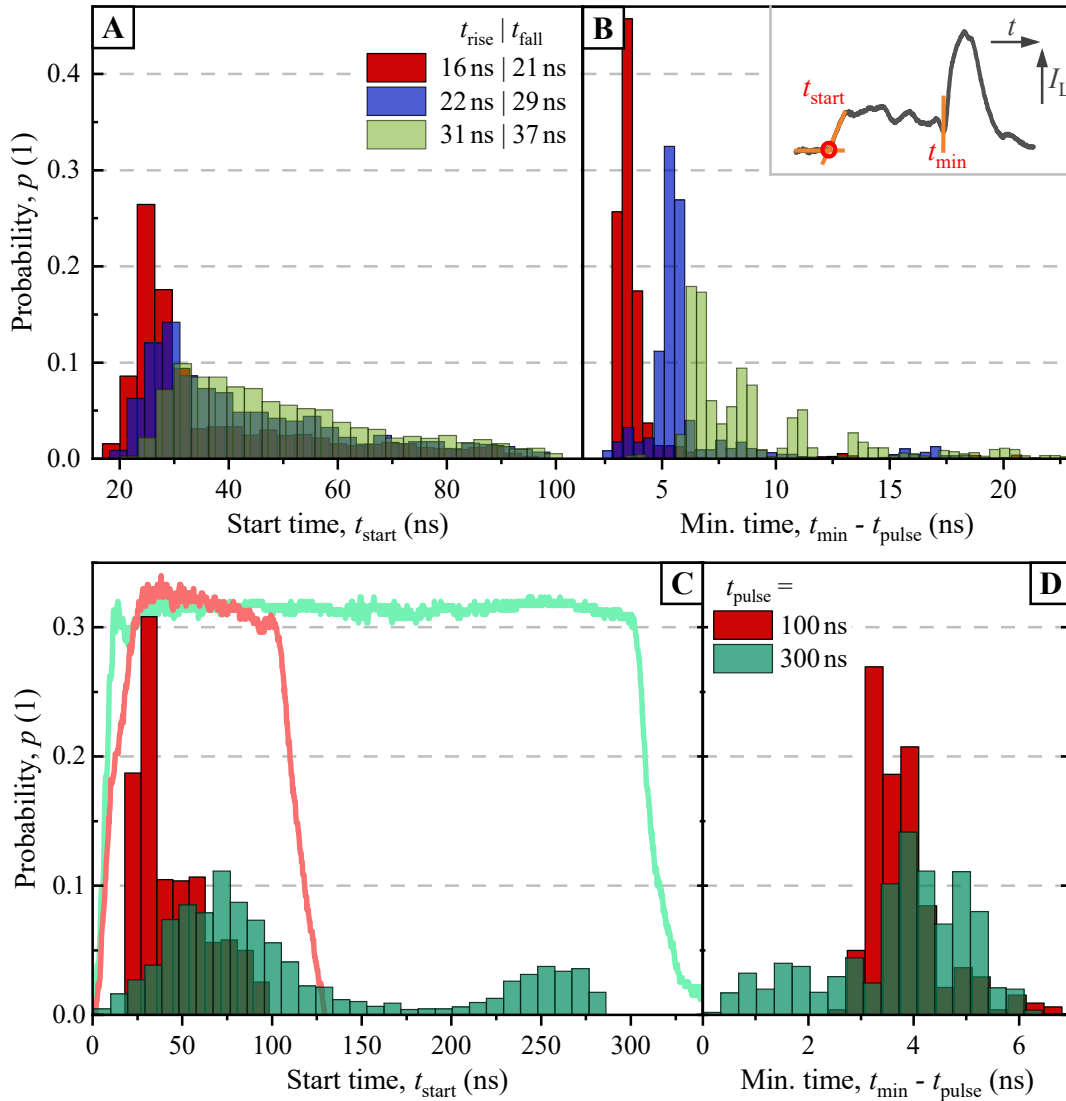


**Abbildung 2.2:** Histogram of inception and reillumination time probability ( $n = 2700$  discharges). Discharge inception time is described by the time of first observable light emission,  $t_{start}$ , while the beginning of reillumination can be associated with the time,  $t_{min}$ , when the discharge current changes polarity. For comparison,  $t_{pulse}$  is subtracted from  $t_{min}$ . Panel A and B show probability distributions for an electrode distance,  $d$ , of 8 mm, pulse amplitude,  $U_{mean}$ , of 56 kV and fall times of 21 ns (red), 29 ns (blue) as well as 37 ns (green). Panel C and D show the inception and reillumination time probability distributions, respectively, for pulses with durations,  $t_{pulse}$ , of 100 ns (red) and 300 ns (green) and a pulse amplitude of 61 kV applied to a 14 mm gap. Adapted from Article 2.

distribution of the inception delay of a discharge, i.e. the start time,  $t_{\text{start}}$ , for different pulse steepnesses, characterized by start and fall times, and two different pulse durations of 100 ns and 300 ns. Each histogram contains data from 2700 discharges. Notably, the discharge expansion for 300 ns discharges was expected to exceed 8 mm, so a gap distance,  $d$ , of 14 mm was set and the pulse amplitude was increased so that the electric field at the needle tip was similar for all experiments. Figure 2.2(A) shows the results for different pulse steepnesses, and in general the probability distributions resemble the development of the pulse amplitudes. For the start of the discharge propagation, a pronounced statistical frequency of 27 % was observed for the steepest pulses, and the respective start time corresponds to the time of maximum pulse amplitude. For an inception later in the high-voltage pulse, the probabilities decreased and did not exceed 5 % after 35 ns. Inceptions were observed throughout the high-voltage application, even as late as 95 ns, just before the pulse decay began. For shallower pulse edges, the maximum of the probability distribution decreased and was shifted to later times. Figure 2.2(B) shows the probability distribution for the start of reillumination, ( $t_{\text{min}} - t_{\text{pulse}}$ ). Since the reillumination started during the trailing edge of the pulses, which is only a few nanoseconds long, the maximum of the probability distribution was generally higher than for the start of propagation. For the steepest pulse, with a fall time of 21 ns, the start of the reillumination were distributed over 2 ns with a maximum probability of 45 %. For longer fall times, the probability distribution was delayed and broadened.

The overall inception probabilities are not included in Figure 2.2(A), but can be calculated by comparing the total number of applied pulses with the number of detected discharges. A decreasing ignition probability of 58 %, 33 % and 29 % was observed with increasing rise and fall time. Thus, the time required to ignite a given number of discharges increased with the fall time.

The mean propagation time, which is reflected in the time between discharge onset and start of reillumination,  $\Delta t$ , was not affected by pulse steepness. Since the discharges started later relative to the start of the voltage pulse, the reillumination was also delayed due to longer fall times, so the averaged propagation time was determined to be 71 ns, 69 ns, and 69 ns for increasing fall times.

Figure 2.2(C) shows the probability distributions for pulse durations of 100 ns and 300 ns, and normalized pulse shapes are given for comparison. In general, the 300 ns pulses show a more stable plateau, resulting in a wider distribution of inception times. The highest probability was observed at 71 ns, which corresponds to the time, when the highest amplitudes are applied. The high-voltage pulse had a second local maximum in pulse amplitude around 250 ns, and the inception probability peaked at the same time. A similar association is observed for 100 ns pulses, which had a maximum amplitude at 25 ns and a corresponding maximum inception probability.

Comparing the trailing edge of both pulses, similar fall times of 21 ns and 23 ns were observed for the short and long pulses, respectively. Accordingly, the inception time distribution of the reillumination, shown in Figure 2.2(D), was nearly equal for 100 ns and 300 ns pulses and peaked around 3 ns into the trailing edge.

Two conclusions can be drawn from the presented inception distributions. First, the inception mechanisms of discharges in water seem to be independent of the pulse rise time within the investigated range, as a significantly sharper 300 ns pulse resulted in a delayed inception.

Instead, the overall pulse shape determines the inception distribution, resulting in a maximum inception probability synchronized with the maximum pulse amplitude. Therefore, the discharges do not seem to be initiated by the same mechanism as the nanosecond discharges reported in the literature, as they were found to ignite only during the rising pulse edge, while the inception probability was associated with the change in amplitude  $dU/dt$  [37, 67, 71]. Second, the onset of reillumination depends only on the pulse steepness during the falling edge, i.e. onset was independent of pulse duration and discharge propagation time. For a more detailed discussion, see Sections 2.4 and 2.5.

#### Major findings for the investigated pulse parameter

- Timing of discharge inception in water is independent of pulse rise time in the range of (10-31) ns
- Probability of discharge inception is increased for higher pulse amplitudes; hence local maxima in the voltage signal correspond to highest inception probabilities
- The overall probability to ignite a discharge by a high-voltage pulse increases for shorter rise times

## 2.3 Streamer Propagation

Between the two inception events of initial light emission and reillumination, the streamer propagates in the liquid medium. Figure 2.3 shows images of typical discharges ignited during a 100 ns pulse with increasing  $t_{\text{fall}}$ , i.e. 20 ns (Panel 2.3(A)), 26 ns (Panel 2.3(B)), 43 ns (Panel 2.3(C)). For these images, the fast framing camera gate was set to the end of the propagation phase to capture the fully expanded discharge. In general, the intensity of the discharge light emission peaked at the needle tip, from which the filaments spread radially. With greater distance from the needle, the filaments became increasingly branched and the light intensity increased again at the end of the filaments. Comparing discharges for different pulse steepnesses, the overall structure remained similar. Additionally, this was observed in

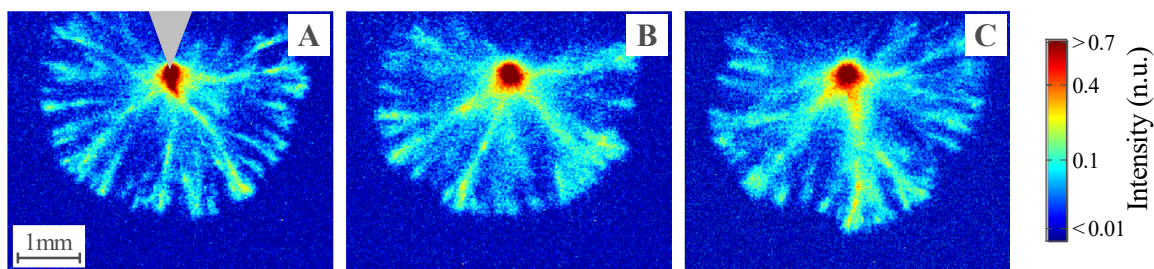


**Abbildung 2.3:** Discharges in water generated at a 40- $\mu\text{m}$  needle tip by the application of positive 100 ns pulses with different fall times of 20 ns (Panel A), 26 ns (Panel B), 43 ns (Panel C). All images were recorded with a 3 ns gate width and intensities were normalized with respect to the maximum possible pixel value (12 bit). Adapted from Article 1.



the investigations reported in Article 2 for a different electrode gap,  $d$ , and an extended pulse duration of 300 ns, where the images also show the same overall discharge morphology. Therefore, the discharge propagation mechanism seems to be unaffected by the pulse shape, i.e. rise time, plateau shape and pulse duration, within the investigated parameter range.

In Article 2, a detailed analysis of the filamentary structure was described. Time-integrated images were taken with the ICCD camera and an algorithm was developed to determine the outer contour of a discharge from which streamer ends and their position relative to the needle tip were derived. The results are shown in Figure 2.4.

Typical examples for identified streamer ends, streamer lengths,  $L_s$ , and angular positions,  $\phi$ , are presented in Figure 2.4(A) for a 100 ns pulse. The angular distribution of streamer lengths was derived by averaging the enveloping contour of selected discharges with a propagation time,  $\Delta t$ , in the ranges from (70-90) ns and (240-260) ns, the latter only for 300 ns pulses. The results are shown in 2.4(B). For shorter propagation times, the contours are similar for both pulse durations and resemble approximately a semicircle with a radius of 2.5 mm around the tip, indicating a spherically symmetric distribution. Only a slight decrease in streamer length was observed for angles of more than  $\pm 50^\circ$ . However, the uniform distribution changed significantly when the discharges propagated for a longer time of (240-260) ns. Only filaments propagating towards the counterelectrode within a  $\pm 20^\circ$  range exceeded a filament length of 7.5 mm. For larger angles, the streamers ended at shorted distances from the needle, and for angles larger than  $\pm 70^\circ$ , the streamers had a length of only 2.5 mm. Thus, the streamers

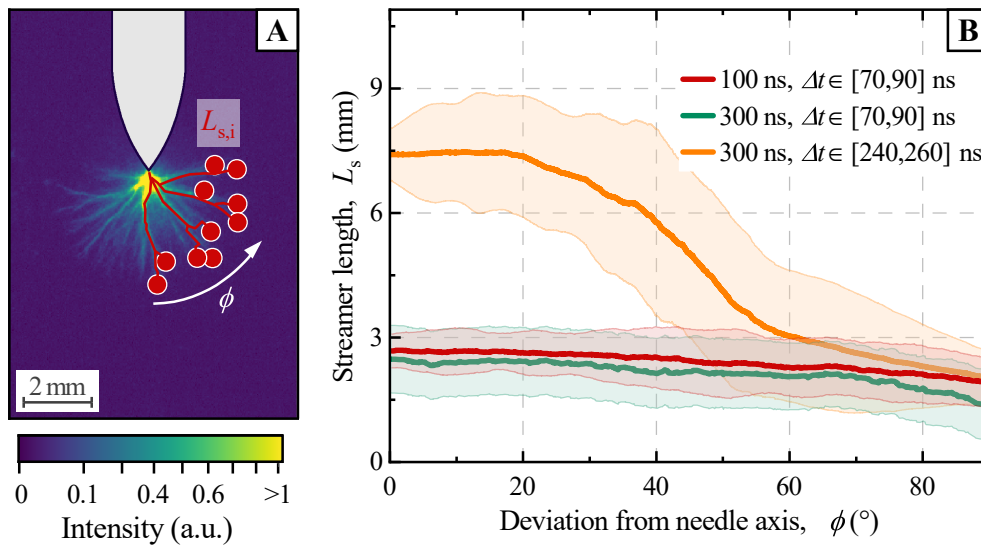


**Abbildung 2.4:** Automated determination of filament ends in ICCD-images (Panel A) and the resulting angular distribution of streamer lengths,  $L_s$ , (Panel B). The spatial structure of an individual discharge is visualized and the streamer length is defined, which is automatically determined for all visible filament ends (for visibility, only half of the detected streamers are shown). The angular distribution of streamer lengths relative to the needle axis is shown for propagation times,  $\Delta t$ , of approx. (80 and 250) ns. Filaments are homogeneously distributed around the needle tip for the first 90 ns, but propagation stops for  $\phi > 50^\circ$  afterwards. Adapted from Article 2.

seem to have stopped propagating early during the pulse. This effect is plausible when considering the electric field between the needle and plate. For a constant distance to the needle tip, the field strength is strongest along the needle axis and weakens for increasing angles,  $|\phi|$ . Therefore, filaments propagating perpendicular to the needle axis extend into areas with a reduced external electric field. Experiments for microsecond discharges have also shown that streamer stop propagating when the electric field between the electrodes weakens to a critical value [47, 49]. In this experiment, the first filaments propagated into regions, where the electrical field strength was below this critical value, after (70-90) ns corresponding to streamer lengths around 2 mm directed at an angle greater than  $\pm 70^\circ$ . This was, therefore, not observed for the majority of discharges initiated by 100 ns pulses, as they propagated only for 70 ns on average, but is important to consider when determining propagation velocities for longer pulse durations.

Two different methods were used to measure the propagation velocity,  $v_s$ , of streamer discharges in water, and the results of both are shown in Figure 2.5. For the first measurement, shown in Figure 2.5(A) and published in Article 1, the fast framing camera was set to capture three consecutive images of an individual discharge event. Due to the radial symmetric distribution of the streamer ends, the light intensities were averaged in semicircles around the needle tip and plotted against radius. From these profiles, shown in the three smaller plots in Figure 2.5(A), an averaged streamer length,  $L_s$ , was determined. The increase in streamer length for a given delay between two image acquisitions provided the averaged velocity. Since three images were recorded per discharge, the velocities between the first two and last two recor-

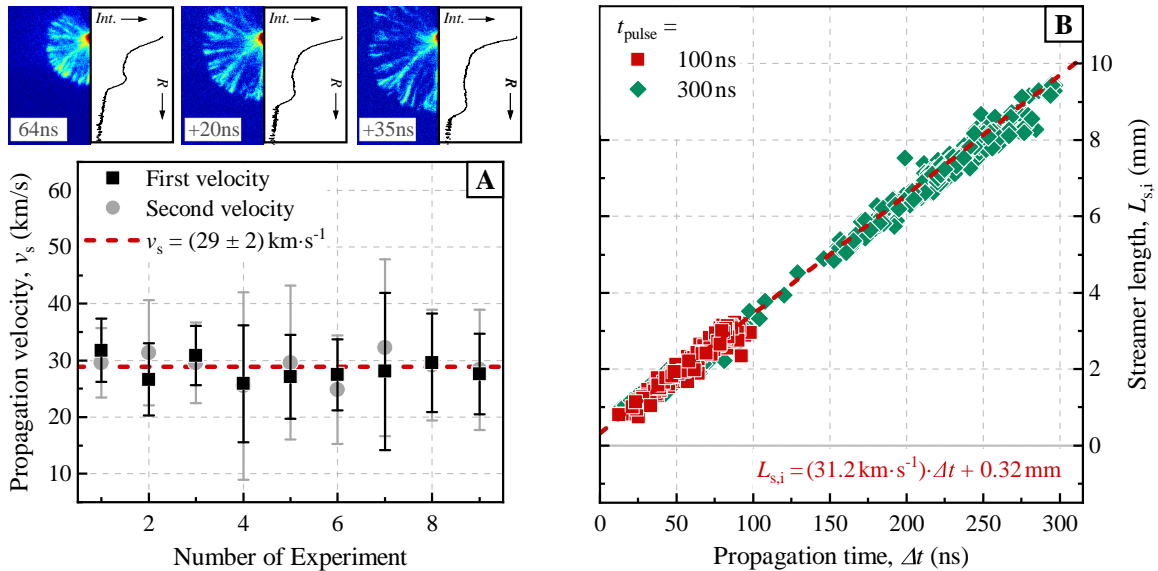


**Abbildung 2.5:** Determination of streamer propagation velocity, firstly, with subsequent framing camera images for individual discharge events (Panel A, gate opening time of 3 ns) and, secondly, with streamer lengths,  $L_s$ , as well as propagation times,  $\Delta t$  (Panel B). Both, the direct measurement and the averaged method, result in a propagation velocity of about  $31 \text{ km}\cdot\text{s}^{-1}$ . Adapted from Article 1 and Article 2.

ding times were calculated. For the steepest pulses, the resulting propagation velocity was constant at  $(29\pm 2)$  km·s<sup>-1</sup>. The procedure was also applied to fall times of 26 ns and 43 ns, resulting in velocities of  $(28\pm 1)$  km·s<sup>-1</sup> and  $(29\pm 1)$  km·s<sup>-1</sup>, respectively. These values confirm experiments from literature and show that the pulse steepness had no effect on the discharge propagation within the parameter range of this study [45, 47, 48, 65].

A second method to measure the propagation velocities for 100 ns and 300 ns pulses was applied for the experiments reported in Article 2 and the results are shown in Figure 2.5(B). The streamer lengths determined by the algorithm analyzing the ICCD images (see Figure 2.4(A)) were associated with the corresponding propagation time (shown in Figure 2.2(C)), which yields the mean propagation velocity of a filaments during its propagation phase. Since a filament that did not propagate along the axis of the needle might have stopped due to a locally weaker electric field, the maximum length of the streamer was determined for each discharge.

The streamer length increased linearly with longer propagation times, reaching a maximum of about 9 mm. Again, this indicates a constant propagation velocity, which was inferred to be  $(31.2\pm 0.6)$  km·s<sup>-1</sup> from the slope of a linear fit. This result is similar to the first method, validating the indirect approach to investigate propagation velocities. The velocity was the same for both pulse lengths, implying that the propagation process is independent of propagation time or streamer length as long as the external electric field strength exceeds a critical value.

#### Major findings for the investigated pulse parameter

- The discharge structure is independent from pulse steepness
- Filaments that are not directed towards the counter electrode stop propagating for propagation times longer than 90 ns
- Streamer propagation velocity is about 30 km·s<sup>-1</sup> for all considered pulse parameters

## 2.4 Channel Reillumination

Due to the decreasing amplitude at the end of the high-voltage pulse, the discharge propagation stops. Contrary to intuition, discharges in water do not decay completely, but increase light emission again during the trailing edge of the pulse, reaching intensities higher than during propagation (see Figure 2.1(C)). Therefore, this reignition process is commonly called reillumination [45, 47]. However, reilluminations during nanosecond pulses are different from those ignited during microsecond pulses because they are accompanied by negative current polarity instead of positive current spikes (cf. Section 1.2). Therefore, a fundamentally different reillumination mechanism seems to be relevant for short pulses.

In the investigation described in Article 1, the reillumination process was studied for pulse durations of 100 ns. Consecutive images of the same individual discharges were recorded to observe the development of reillumination with temporal and spatial resolution. For pulse durations of 20 ns and 43 ns, the results are presented in Figures 2.6(A) and 2.6(B), respec-

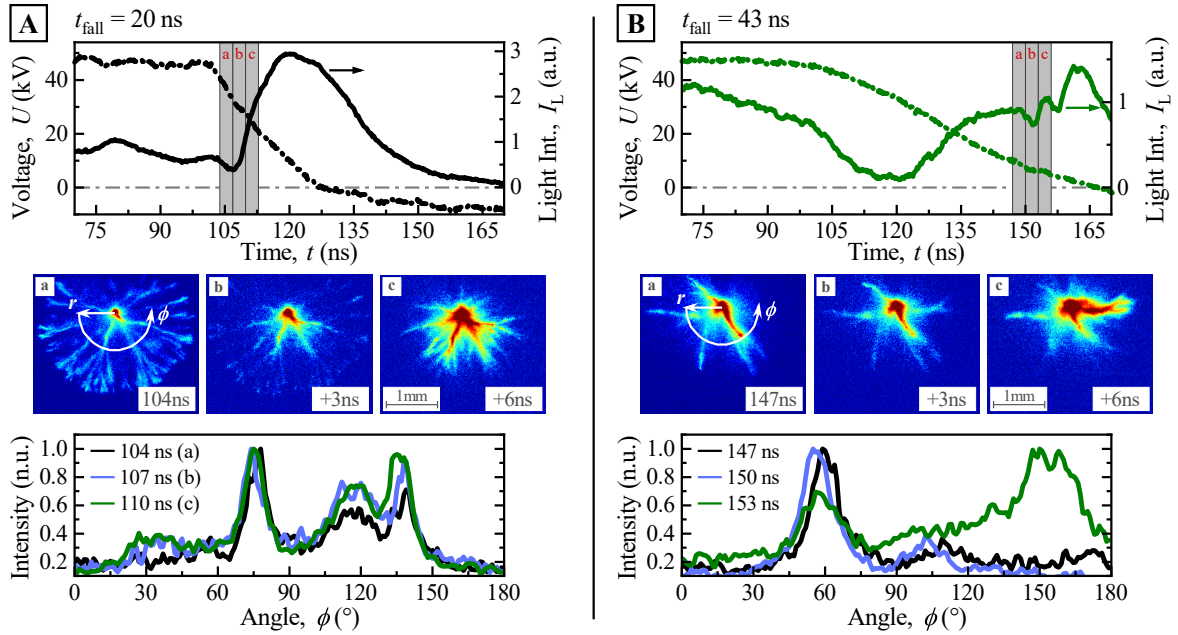


**Abbildung 2.6:** Detailed image analysis of the onset of the discharge reillumination for a fall time of 20 ns (Panel A) and 43 ns (Panel B). For altogether 9 ns, three individual consecutive images were recorded. Respective measurements for voltage and light intensity are presented together with the acquired images (a), (b) and (c), according to the timing information (gray bars) shown in the upper panel. The angular intensity profiles (lower panel) were derived for a semi-circle with a radius of 0.7 mm around the needle tip. For the shorter fall time, the images describe the discharge at the end of its propagation (a), the reignition of filaments starting from the needle tip (b) and, eventually, the propagating reillumination (c). Therefore, the angular intensity profile show no significant difference confirming the instantaneous reillumination of all pre-existing channels. Contrarily, a channel that was not visible in the first image was reilluminated (b-c) within 6 ns for a longer fall time. Adapted from Article 1.

tively. The upper panel shows the pulse voltage and light intensity and the gate time of the fast framing camera. The resulting images for a typical discharge are displayed in the middle panel, from which angular intensity profiles were derived and plotted in the bottom panel to illustrate intensity changes individually for the filaments over the period covered by the images.

For the shortest fall time, the camera gate was set to observe the beginning of the again increasing light emission. With a gate width of 3 ns, the images recorded a period of 9 ns, as the gate time of each ICCD was chosen at the end of the gate of a preceding camera. The first image (a) shows the fully expanded discharge similar to Figure 2.3. As the light intensity passed through a minimum, the next image (b) was taken. The streamer ends from the previous image are still faintly visible, but the origin of the increasing light emission was the bright discharge center at the needle tip. Generally, the channels increased in intensity compared to image (a). While the original filament heads were no longer visible, the intense reillumination discharge expanded during the recording of image (c). The structure of the preexisting discharge is clearly preserved in the new discharge. If the gate times were delayed further, the

reillumination continued along the preexisting channels until it reached the original discharge expansion, which corresponded to the maximum in total light intensity (data not shown). To emphasize which channels were reignited, the light intensity was plotted along a semicircle of fixed radius,  $r$ , of 0.7 mm around the needle tip. The bottom panel of Figure 2.6 shows the normalized intensity profiles relative to the angle,  $\phi$ . The profiles of the decaying and reilluminating discharges almost overlap, while the three prominent peaks correspond to the brightest filaments. Therefore, each discharge channel was reilluminated while the reignition front propagated with a velocity in the order of  $10^2 \text{ km}\cdot\text{s}^{-1}$ , which is an order of magnitude faster than the original discharge propagation. Due to this speed and the negative current flowing during the reignition, the reillumination was most likely an electron-driven ionization front expanding into the preexisting, preionized and gaseous filaments of the preceding discharge to balance the charge accumulated at their ends.

A different reillumination process was observed for a fall time of 43 ns, as shown in Figure 2.6(B). Due to the extended fall time, the gate times of the framing camera were delayed to account for the deferred development of the light intensity maximum. For presentation purposes, a discharge with a local intensity spike was chosen as an example. The images cover the intensity development of an already reignited discharge starting at a local minimum. Image (a) shows one bright and two less intense filaments, which are diffuse and peak in intensity at the needle tip, similar to the reillumination for shorter fall times. In Article 1 it was additionally reported that the reignition develops within the preexisting discharge channels. However, not every channel is reignited at the same time, as shown in images (b)

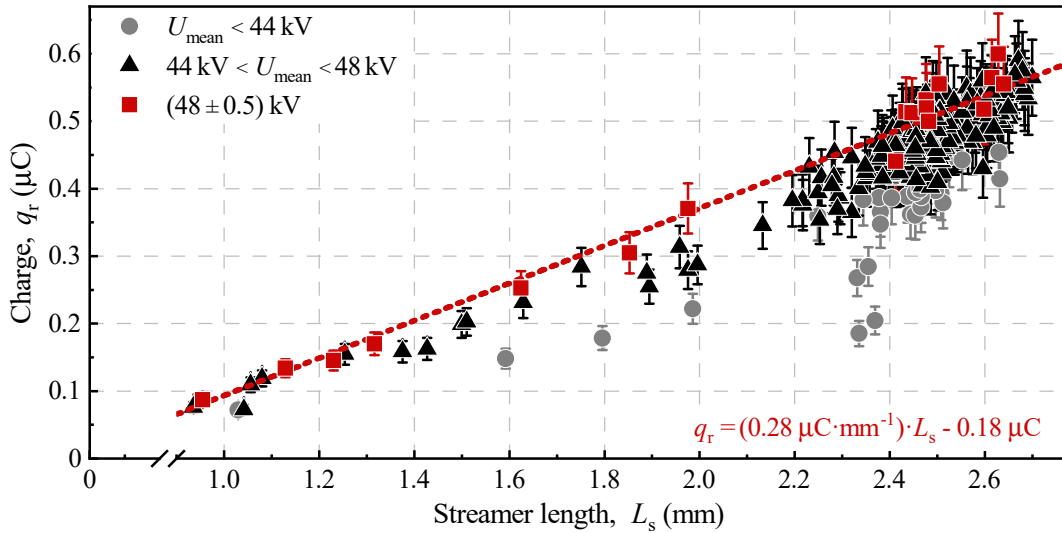


**Abbildung 2.7:** Charge backflow,  $q_r$ , into the filaments during the trailing edge of applied voltage pulses depending on the spatial expansion,  $L_s$ , of discharges with respect to pulse amplitudes, as described by  $U_{\text{mean}}$ . Each data point represents a single discharge event. A linear dependency can be assumed for the highest amplitudes (dashed red line) while for lower amplitudes a stronger variation of results and a deviation from this proportionality was observed that is likely reflecting the more erratic initiation of discharges. Adapted from Article 1.

and (c) of Figure 2.6(B). A filament that was not visible in image (a) developed toward the right corner of the image, while in image (c) it was the brightest filament; the other channels also reduce their intensity. This phenomenon is more apparent in the intensity profiles in the bottom panel (see Figure 2.6(B)). For the profiles derived from images (a) and (b), a filament at an angle of  $60^\circ$  was dominant, while the filament at  $150^\circ$  was the most intense in image (c). The spatially integrated light intensity peaked simultaneously, indicating that the single reilluminated channel mainly contributed to the intensity maximum. This was also observed for other discharges investigated in this experiment, and in addition, multiple peaks for a single discharge suggest that all preexisting channels were subsequently reignited.

So far, the study revealed the general phenomenology of reillumination and how it is affected by the shape of the pulse. In addition, it was hypothesized in Article 1 that the reillumination could be valuable as a diagnostic to characterize the charge stored in nanosecond pulsed discharges. As mentioned earlier, the head charge of the filaments is balanced during reillumination and, hence, the charge transferred during reillumination,  $q_r$ , can be used as an approximation of the head charge. To emphasize the use as a diagnostic tool, the streamer length,  $L_s$ , was associated to the transferred charge, which was obtained by integrating the current from  $t_{\min}$  until no current was observed. The results are shown in Figure 2.7 with respect to three different ranges of pulse amplitudes,  $U_{\text{mean}}$ .

In general,  $q_r$  increased with the streamer length, while for all three groups of amplitudes  $L_s$  covered a reasonable range. For smaller pulse amplitudes, however, the charges were distributed more erratic, so the recorded discharges were grouped according to the amplitude lower than 44 kV, between 44 kV and 48 kV, and higher than 48 kV. The charges within the first group were scattered in a range up to 0.3 C, while the charges for the highest amplitudes were linearly dependent on  $L_s$ . Therefore, a linear fit was performed only for the highest pulse amplitudes, as shown in Figure 2.7. Interestingly, this linear approximation was independent of the fall time, even though the time to transfer  $q_r$  was nearly doubled and the channel reillumination was different for shallower pulses, i.e. subsequent channel reignition as opposed to synchronized reillumination (see Figure 2.6). Therefore, the charge transferred during reillumination must be associated with the propagating streamers, which were not affected in velocity or morphology when the pulse shape was changed. In Article 1 a model has been developed to characterize streamer propagation by the charge transferred during reillumination, which is summarized in the next section.

### Major findings for the investigated pulse parameter

- Reillumination is an reignition of preexisting discharge channels by an ionization front extending with  $200 \text{ km}\cdot\text{s}^{-1}$  from the needle tip
- Reillumination occurs simultaneously in all filaments for the shortest fall time and subsequently in individual filaments for the longest fall times
- The transferred charge during reignition is directly proportional to the streamer length and independent on fall time



## 2.5 Single Streamer Propagation Model

So far, the discharge development has been described on the basis of an experimental approach, but the interpretation of several findings, i.e. the influence of different fall times on the reillumination phase, the upper limit of  $q_f$  proportional to  $L_s$ , and the reduced charge transfer during reillumination for smaller pulse amplitudes, requires a theoretical approach. Hence, an analytical model relating streamer head charge, electric potential and propagation length has been developed and described in Article 1. Initially, a simplified approach describing a single, unbranched streamer was chosen, and subsequently the model was extended to include multiple branches.

The fundamental correlation used to formulate a model for the description of streamer propagation in water in terms of the accumulated charge of filament heads was recently published by Qin *et al.* [87]. The group simulated streamer propagation in gases and liquids and found (analytically and numerically) that the radius of propagating streamers depend on the external electric field generated by the electrodes. This correlation was described analytically by the following Equation:

$$R_s \propto \frac{1}{E_{\text{ex}}} \quad (2.1)$$

The radius of the filament head,  $R_s$ , is inversely proportional to the external electric field,  $E_{\text{ex}}$ . Notably, the authors stated that this correlation is valid not only for gaseous media, but also for dielectric fluids such as deionized water. The resulting model is shown in Figure 2.8, where all relevant variables are defined.

A streamer with radius  $R_s$ , length  $L_s$ , and head potential  $U_{\text{head}}$  propagates at a constant velocity,  $v_s$ , in an external electric field. Without loss of generality,  $E_{\text{ex}}$  is generated by a positively charged electrode of potential  $U_{\text{needle}}$  and is strong enough to sustain the streamer

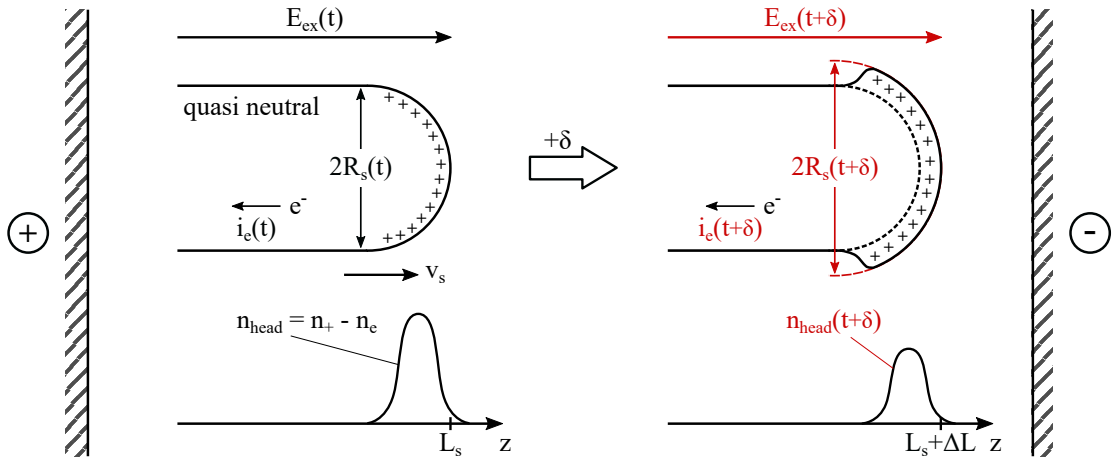


**Abbildung 2.8:** Illustration of the single streamer propagation model. A quasi-neutral channel of radius,  $R_s$ , with a head charge corresponding to a charge density,  $n_{\text{head}}$ , extends with a velocity,  $v_s$ . The strength of the external applied electric field,  $E_{\text{ex}}$ , decreases at the streamer head during a time step,  $\delta$ . Hence, the streamer radius grows resulting in smaller values for  $n_{\text{head}}$ . Reprinted from Article 1.

expansion. At the observed time,  $t$ , a charge density,  $n_{\text{head}}$ , has accumulated due to a backflow of electrons,  $i_e$ , and continuous ionization during streamer propagation.

When the streamer propagates for an infinitesimal time step,  $\delta$ , it is assumed to have extended by  $\Delta L = v_s \cdot \delta$  while the external electric field has been reduced to  $E_{\text{ex}}(t+\delta)$ . According to Equation 2.1,  $R_s$  increases, which means that  $n_{\text{head}}$  decreases. The head charge,  $q$ , of an ideally conducting streamer is correlated to  $R_s$  and  $U_{\text{head}}$  by Equation 2.2 [31].

$$q = 4\pi\epsilon_0 U_{\text{head}} R_s \quad (2.2)$$

Thus,  $q$  is related to the external electric field due to the relation described in Equation 2.1. In a needle-to-plate electrode configuration, the external electric field,  $E_{\text{ex}}$ , along the needle axis with coordinate  $z$  is approximated by the following Equation

$$E_{\text{ex}} = \frac{2U_{\text{needle}}}{z \ln\left(\frac{4d}{r_n}\right)} \propto \frac{U_{\text{needle}}}{z}, \quad (2.3)$$

with the needle radius,  $r_n$ , and the distance between the electrodes,  $d$  [88]. The proportionality expressed by Equation 2.1 can be quantified by a respective constant,  $a_E$ , which yields

$$q = 2\pi\epsilon_0 \cdot a_E \ln\left(\frac{4d}{r_n}\right) \cdot \frac{U_{\text{head}}}{U_{\text{needle}}} \cdot z = b \cdot z. \quad (2.4)$$

As long as the streamer is ideally conductive, the ratio of head and needle potential reduces to unity. Accordingly, the head charge is linearly dependent on the position,  $z$ , of the streamer head, which is directly related to the streamer length,  $L_s$ .

So far, this model does not account for the branching observed in water streamer discharges. With two reasonable assumptions, it is still possible to interpret the experimental results with this single streamer model. As mentioned in Section 1.2, all of the filaments observed in Figure 2.3 actually originate from the same location on the needle tip and can, therefore, be considered fragments of a single, strongly branched streamer [37, 48, 53]. In addition, the charge accumulated at a streamer head is assumed to be conserved during branching, which was confirmed in gas streamer discharges [40]. Hence, the total charge of a discharge is independent of the number of branches, so it can be described as a single filament.

To combine the filaments, a discharge can be described in an equivalent electrical circuit model by capacitances,  $C_i$ , connected in parallel to the needle electrodes through ideally conductive channels. Thus, the individual capacitances can be combined into a single capacitance. According to Loeb *et al.*, the capacitance of a streamer head is related to the streamer radius; therefore, the total capacitance,  $C$ , of a discharge can be expressed by Equation 2.5 [31]:

$$C = \sum_i C_i = 4\pi\epsilon_0 R_s. \quad (2.5)$$

Capacitance and charge of a streamer are closely correlated, and therefore the total charge of a branched discharge also depends linearly on the streamer length (see Equation 2.4).

While measurement of the spatial extent of the discharge is accessible by fast imaging, direct measurement of the accumulated charge of a discharge of defined length is more challenging.



However, the charge that is transferred during reillumination can be used as an approximation. The ionization front within the preexisting channel transfers negative charges into the channel as long as there is a space charge at the filament head, and is thus proportional to the head charge. Of course, this is an approximation, since the head charge can diffuse and its ions can recombine before and during reillumination. However, diffusion does not reduce the total charge, and the recombination cross sections should be similar for different head charges. Thus,  $q_f$  may be smaller than, but proportional to, the head charge. Evidently, the relation between head charge and streamer length in Equation 2.4 was experimentally confirmed with the data shown in Figure 2.7 for the highest needle potentials, as  $q_f$  grew proportional to the streamer length. Inherently, this implies that the assumption of ideally conducting channels is valid for the applied pulse amplitudes.

However, it is noticeable that charges for lower pulse amplitudes deviate from the linear relation described in Equation 2.4. In particular, discharges initiated during pulses with amplitudes below 44 kV accumulated up to 60% lower head charges. This indicates that the filaments were not ideally conductive for these pulse amplitudes, resulting in a decrease of the parameter  $b$ , as the ratio between  $U_{\text{head}}$  and  $U_{\text{needle}}$  reduces with increasing channel resistance.

The development of the ionization front of the reillumination can be interpreted in particular with the single streamer model. For decreasing fall times, the reillumination changes from an immediate reignition of each preexisting filament to a sequential process, as shown in Figure 2.6. In Equation 2.5 it is assumed that the head charge is conserved during the branching of a filament, i.e. the combined head charge of filaments propagating after the branching is equal to the charge of the predecessor. While this assumption is necessary to translate the single streamer model to a real discharge, it is not required to define how the charge is divided during branching. Thus, the tips of each branch may be charged slightly differently. During the trailing edge of the pulse, the residual head charge generates the electric field within a channel that drives the ionization front causing the reillumination. This electric field is dependent on the head charge, with a higher charge producing a stronger electric field. Due to the potentially different head charges resulting from branching, this yields a different threshold potential at the needle for which the field in the channel is high enough for reignition. For fast fall times, the different thresholds for reillumination seem insignificant, but for longer fall times, a lower head charge may be responsible for delayed reillumination, resulting in successive channel reillumination (see Figure 2.6).

#### Major findings for the investigated pulse parameter

- A single streamer model can describe the experimental results, e.g. streamer head charge and reillumination, based on the streamer radius and external electric field
- The head charge of a single streamer is directly proportional to the length of a filament, which was confirmed experimentally
- Filaments that are not ideally conductive have a reduced head potential resulting in smaller head charges



### 3 Hydrogen Peroxide Production of Nanosecond Pulsed Discharges (A2-A3)

After the physical characterization of positive pulsed streamer discharges in water, in this section, the findings are related to the chemistry induced by the discharges, which is crucial for most applications [11, 13, 15, 18, 19, 36, 42]. A streamer discharge has several pathways to produce chemically active species, e.g. by ions, electrons, excited neutrals, radicals, radiation, temperature, and cavitation and a number of different species, e.g.  $\cdot\text{O}$ ,  $\cdot\text{OH}$  or  $\cdot\text{OOH}$ , are produced either directly by the discharge or in secondary reactions. Most of these species are highly reactive and, therefore, challenging to quantify directly. For discharges in pure water, however, it was discovered that eventually all short lived species react to  $\text{H}_2$ ,  $\text{O}_2$  and  $\text{H}_2\text{O}_2$ , while only hydrogen peroxide remains dissolved in the liquid [21, 78]. Hence, the hydrogen peroxide production of pulsed streamer discharge in water can be utilized to characterize the induced chemistry. In the past, the  $\text{H}_2\text{O}_2$  production was studied and optimized in terms of pulse parameters, i.e. amplitude, duration, and repetition frequency, and material properties such as pH, conductivity, and electrode material [16, 18, 23–26, 29, 29, 78–86]. However, a major difficulty is that the production parameters are interdependent. For example, in common the Marx-type pulse generators, as conductivity increases, pulse duration and amplitude decrease, so no study has examined the influence of each pulse parameter separately on hydrogen peroxide production.

However, the pulsed power system presented in Section 2.1 is able to apply pulses, whose pulse shape is independent of the properties of the discharge chamber, such as geometry and conductivity (within reasonable limits), while the pulse parameters can be adjusted individually.

A typical hydrogen peroxide production rate of a water discharge has been reported to be  $1 \text{ g}\cdot\text{kWh}^{-1}$  [89], and in this thesis a typical discharge had an energy on the order of tens of millijoule, resulting in an estimated amount of hydrogen peroxide on the order of hundreds of picomoles. Due to the limited repetition rate of the pulsed power system, colorimetric methods for determining hydrogen peroxide concentrations are not sensitive enough for this study. Accordingly, an electrochemical method was developed, which is described in Section 3.1. A detection limit of  $0.05 \mu\text{mol}\cdot\text{l}^{-1}$  and a recovery of 98.4% was achieved.

Using the custom-built pulsed power system and the sensitive method for determining  $\text{H}_2\text{O}_2$  concentration, it was possible to study hydrogen peroxide production for each pulse parameter separately. The results were published in Article 2 and are summarized in Section 3.2 of this thesis. With slight methodological modifications, it was found that the electrochemical system was even suitable to measure the hydrogen peroxide concentration produced by individual discharges, which was studied for different conductivities and published in Article 3. The main outcomes of this article are presented in Section 3.3.

### 3.1 Flow Injection Analysis with Chronoamperometry

Hydrogen peroxide concentrations were measured by an electrochemical, chronoamperometric method using a flow injection analysis technique. An overview of the developed method is given in Figure 3.1. It consists of a scheme of the experimental setup in Figure 3.1(A), a typical measurement in Figure 3.1(B), and a calibration in Figure 3.1(C). Overall, the setup consisted of two separate lines for buffer and sample solution connected by a 6-port valve. Initially, the buffer ( $13.4 \text{ g}\cdot\text{l}^{-1} \text{ KH}_2\text{PO}_4 + 0.27 \text{ g}\cdot\text{l}^{-1} \text{ Na}_2\text{HPO}_4 + 7.5 \text{ g}\cdot\text{l}^{-1} \text{ KCl}$  in deionized water) was pumped at  $1.3 \text{ ml}/\text{min}$  through the valve into the measuring chamber onto a 3-electrode screen-printed chip (DRP-710, *Metrohm*) and from there into the waste container. The 3-electrode system consisted of a Prussian blue functionalized carbon working electrode,

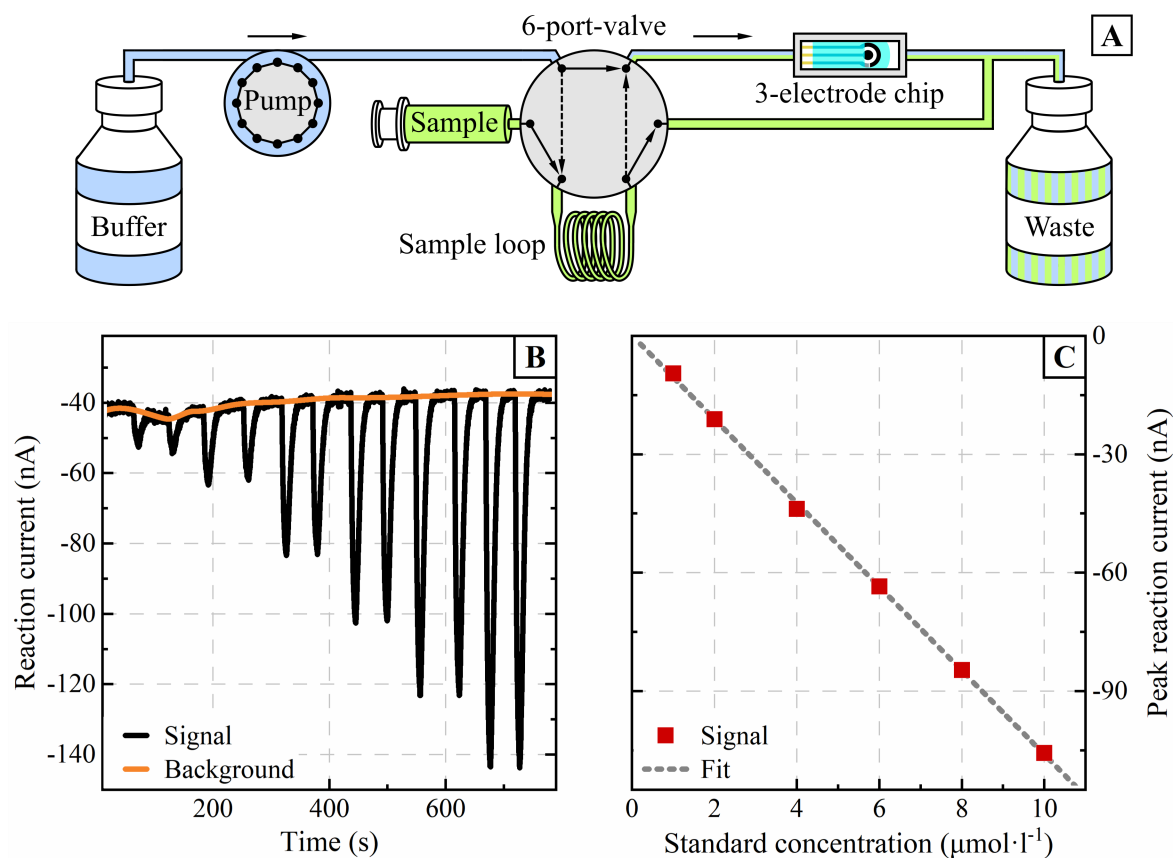


**Abbildung 3.1:** Schematic of the experimental setup to electrochemically determine hydrogen peroxide concentration (Panel A), a representative chronoamperogram with a background fit (Panel B), and a typical calibration measurement (Panel C) derived from the chronoamperogram. A buffered sample is loaded with a syringe into a sample loop and, if the 6-port-valve is switched, pumped into a measurement chamber. The sample flows through the measurement chamber and reacts with the functionalized surface of a 3-electrode chip. The temporal development of the reaction current is recorded by a potentiostat. For the association of reaction currents and the hydrogen peroxide concentration of the sample, peak reaction currents are determined and related to concentrations by a calibration.

a carbon counter electrode, and a silver reference electrode. Samples were manually loaded into the sample loop, while any excess was discarded. To analyze a sample, the 6-port valve was turned to allow the pump to flush the sample loop into the measurement chamber. A potentiostat (PGSTAT101, *Metrohm*) measured the reaction current at a potential of -0.1 V with a sampling rate of 20 S·s<sup>-1</sup>.

A typical measurement for calibration is shown in Figure 3.1(B). Each of the six different samples of adjusted hydrogen peroxide concentrations were injected twice. Hence, the presented signal consists of pairs of current peaks proportional to the H<sub>2</sub>O<sub>2</sub> concentration in the respective samples, which are superimposed by a background current. The background current was fitted with a spline, subtracted from the signal, all current peaks belonging to a single sample were averaged, and the peak amplitude of the averaged signal was extracted. The peak currents were correlated with the known hydrogen peroxide concentration in the samples. The result is shown as an example in Figure 3.1(C), which also shows a linear fit that was used as calibration function. As the reference electrode was made of silver, which is susceptible to oxidation, an additional reference sample with known H<sub>2</sub>O<sub>2</sub> concentration was injected after each measurement to guarantee the validity of the calibration. A detection limit of 0.05 μmol·l<sup>-1</sup> and a recovery of 98.4% (for a concentration of 1 μmol·l<sup>-1</sup>) was achieved.

An analysis of hydrogen peroxide production from one or more discharges always consisted of at least measurements of two samples. A reference sample was taken before and a treated sample was taken after the desired number of discharge events were applied. Both had a volume of 4.5 ml and were immediately mixed with 0.5 ml of a 10-times concentrated buffer solution so that the conductivity, pH and ion concentration of the samples matched the running buffer.

For the lowest hydrogen peroxide concentrations, i.e. for the production of individual discharges, the method was slightly adjusted. Since the treated volume was reduced to 0.8 ml, a sample of 0.75 ml was mixed with 0.05 ml concentrated buffer and the reference was collected separately every ten samples.

## 3.2 Hydrogen Peroxide Production Rate and Efficiency

Rate and efficiency of hydrogen peroxide production were determined from the total amount of hydrogen peroxide, which was accumulated for several hundred discharges, and was studied for different pulse amplitudes, durations, and steepnesses, characterized by  $t_{\text{fall}}$ . While the results for energy efficiency are presented in Article 2, the production rates are shown in Figure 3.2. This Figure is divided into three panels: Panel 3.2(A) shows the production rate,  $k$ , as a function of  $t_{\text{fall}}$ , Panel 3.2(B) illustrates the influence of  $U_{\text{mean}}$  and Panel 3.2(C) describes the difference depending on  $t_{\text{pulse}}$ . The production rate was calculated from the hydrogen peroxide concentrations and the accumulated propagation time of all individual discharges, so that a change in inception probabilities is included in the rate coefficients (see Figure 2.2).

There are no actual differences in production rates for different fall times, as shown in 3.2(A). Instead, an averaged production rate of  $(0.145 \pm 0.005) \text{ mol} \cdot \text{l}^{-1} \cdot \text{s}^{-1}$  was derived for fall times of 21 ns, 29 ns, and 37 ns. Accordingly, the energy efficiency was also the same with  $(5.8 \pm 0.1) \text{ g} \cdot \text{kWh}^{-1}$ . These similar rates and efficiencies seem reasonable since neither the

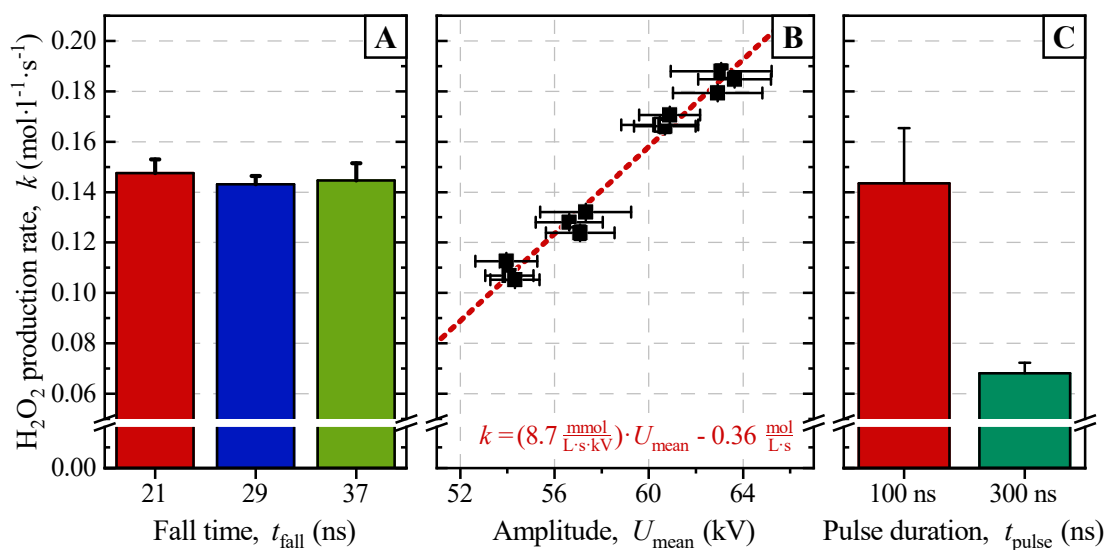


**Abbildung 3.2:** Hydrogen peroxide production rates,  $k$ , for each tested pulse steepness represented with the fall time,  $t_{\text{fall}}$ , (Panel A), pulse amplitudes,  $U_{\text{mean}}$ , between (54-64) kV (Panel B), and pulse durations,  $t_{\text{pulse}}$  of 100 ns and 300 ns (Panel C). Different pulse steepnesses did not affect  $\text{H}_2\text{O}_2$  production, a linear increasing production rate was observed for higher amplitudes, and a decreasing pulse duration increased the amount of produced hydrogen peroxide. Adapted from Article 2.

morphology nor the mean expansion of the discharges were affected by  $t_{\text{fall}}$  (as described in Sections 2.2 and 2.3). Thus, the same amount of energy was dissipated in a similar discharge volume, resulting in a similar temperature, radiation, and radical production, leading to a constant  $\text{H}_2\text{O}_2$  production.

However, as already mentioned in Section 2.2, the probability to ignite a discharge during a pulse depended on the pulse steepness and decreased with increasing  $t_{\text{fall}}$ . From the point of view of studies without a single discharge diagnosis, this would result in a lower hydrogen peroxide production relative to the number of high-voltage pulses applied, again highlighting the importance of observing individual discharge events. In addition, for any application, every pulse that does not ignite a discharge reduces process efficiency, which is why steeper pulses should be preferred for process development.

A more pronounced effect on hydrogen peroxide production was observed for different pulse amplitudes, as shown in Figure 3.2(B). Rates were determined for pulse amplitudes of (54-64) kV and a linear increase was observed for higher amplitudes. For this relatively small range of amplitudes, rates nearly doubled to approximately  $0.19 \text{ mol}\cdot\text{l}^{-1}\cdot\text{s}^{-1}$ , resulting in a slope of  $8.7 \text{ mmol}\cdot\text{l}^{-1}\cdot\text{s}^{-1}\cdot\text{kV}^{-1}$ . Similarly, the accumulated energy dissipated in all discharges was doubled to 16 J, resulting in a constant energy efficiency (see Article 2). Earlier discharge ignition was observed at higher amplitudes, reducing the averaged  $t_{\text{start}}$  from 39 ns to 32 ns; thus, discharges typically expanded for longer times as amplitudes increased.

However, the method of calculating the production rate using the accumulated propagation time of all discharges already includes different delay times, so it does not explain the increasing hydrogen peroxide production rates. More likely, the increased energy dissipation was

associated with the formation of more discharge filaments and the energy density within these filaments was constant [16]. While proof of this interpretation requires a 3D reconstruction of the entire discharge structure, it is supported by the increased light emission of the discharges at higher amplitudes, which indicates that more filaments were formed. The additional filaments led to increased radical formation, resulting in increasing  $\text{H}_2\text{O}_2$  concentrations per discharge. However, since the energy efficiency is stable, it is unlikely that the fundamental pathways of hydrogen peroxide generation, e.g. discharge temperature, density, or radiation, changed with increasing pulse amplitude.

Similar to the pulse steepness, an increase in pulse amplitude resulted in a rising probability to ignite a discharge at any time during a pulse. Ignition probabilities started at 47 % for an amplitude of 54 kV and increased to 87 % for the highest amplitudes, making pulses with higher amplitudes more relevant for any later application.

Figure 3.2(C) shows the effect of pulse duration on the hydrogen peroxide production rate. It is noteworthy that an electrode spacing of 14 mm was used in this experiment, as the discharges extended up to 10 mm from the needle for a pulse duration of 300 ns, resulting in sparking for the 8 mm gap otherwise used for the experiments described in this thesis. Accordingly, the pulse amplitude was increased to 61 kV so that the electric field strength at the needle tip was similar to the 8 mm-experiments. The production rates are shown for pulse durations of 100 ns and 300 ns. The shorter pulses yielded a nearly doubled rate of  $(0.14 \pm 0.02) \text{ mol} \cdot \text{l}^{-1} \cdot \text{s}^{-1}$ , while the energy efficiency increased from  $(6.2 \pm 0.6) \text{ g} \cdot \text{kWh}^{-1}$  to  $(9.2 \pm 0.9) \text{ g} \cdot \text{kWh}^{-1}$ .

The increasing production rate and efficiency with shorter pulses is associated with a decreasing active volume of the discharge. As discussed in Section 2.3, filaments stopped propagating perpendicular to the needle axis about 100 ns after inception, while the discharge continued to propagate along the axis (see Figure 2.4). However, the stopping filaments were not reflected in the dissipated energy, which increased proportionally with the propagation time,  $\Delta t$ . Energy dissipation and  $\text{H}_2\text{O}_2$  production are again related to discharge volume and can be explained by the single streamer propagation model. When a discharge is interpreted as a single streamer, each end of a filament is connected by a conductive channel to all other channel ends. When an individual filament stops expanding, it seems reasonable that the energy dissipated in that filament is instead distributed to the other active channels. To keep the total charge of the channel heads constant, branching is most likely induced, as reported in Article 2, and the current density of the channels with additional heads is increased. While this results in a constant energy dissipation, the limited conductivity of the filaments must be taken into account to explain the reduced hydrogen peroxide production [21, 49]. As shown in Figure 2.7, the channel conductivity is indeed limited, while the resistive losses are proportional to the filament length and scale quadratically with the current density within a channel. Therefore, the energy available for propagation is reduced with each stopping filament, resulting in a lower growth rate of the discharge volume and reduced hydrogen peroxide production.

**Major findings for the investigated pulse parameter**

- Hydrogen peroxide production rates are not affected by pulse steepness, since discharge morphology and mean propagation time are not influenced
- An increased energy dissipation results in higher production rates due to an increased number of discharge filaments
- The stopping of filaments that are directed perpendicular to the needle axis results in the branching of the other filaments, which increases resistive losses in the discharge and lowers  $\text{H}_2\text{O}_2$  production rates as well as efficiencies

### 3.3 Peroxide Production of Individual Discharges

Studying hydrogen peroxide production by treating a sample with multiple discharges is common because it is convenient to increase the  $\text{H}_2\text{O}_2$  concentration in a sample to obtain a better signal-to-noise ratio. Inevitably, only the average hydrogen peroxide production of a discharge can be measured in this way, which leads to systematic errors due to interactions between discharges. For example, each discharge event leads to erosion of the tungsten electrode, resulting in an increasing concentration of tungstates in solution, which dissociate hydrogen peroxide [18, 25, 78]. Also, UV radiation emitted by a discharge cleaves  $\text{H}_2\text{O}_2$  and  $\text{H}_2\text{O}$ , potentially changing the hydrogen peroxide concentration [24].

Thus, the method of electrochemical measurement of hydrogen peroxide presented in Section 3.1 has been optimized to detect concentrations as low as  $0.05 \mu\text{mol}\cdot\text{l}^{-1}$ , which is sufficient to investigate individual discharge events. The results are presented in Figure 3.3(A), where discharges were ignited in water of three different conductivities  $1 \mu\text{S}\cdot\text{cm}^{-1}$ ,  $140 \mu\text{S}\cdot\text{cm}^{-1}$ , and  $280 \mu\text{S}\cdot\text{cm}^{-1}$ , as a parameter of relevance to most applications. In addition, streamer lengths, energy dissipated during propagation, and reillumination energies are presented in Figure 3.3(B-D), respectively.

The amount of  $\text{H}_2\text{O}_2$ ,  $n_{\text{H}_2\text{O}_2}$ , increased non-linearly with time (cf. Figure 3.3(A)). The maximum amount was  $(1.0 \pm 0.1) \text{ nmol}$ , which corresponded to a concentration of  $1.25 \mu\text{mol}\cdot\text{l}^{-1}$  for a single event. Notably, increasing conductivity did not affect hydrogen peroxide production, which was why the measurements were combined for fitting. As motivated later, a parabola could be fitted to the combined data and the fit yielded a slope of  $99 \text{ nmol}\cdot\mu\text{s}^{-2}$ . The streamer length shown in Figure 3.3(B) grew linearly with propagation time, confirming the results presented in Section 2.3. Discharge propagation was not affected by conductivity, so the data sets were combined again to fit a linear function. The result was a propagation velocity of  $31.1 \text{ km}\cdot\text{s}^{-1}$ , which agrees well with the previously measured velocities [49, 50].

Conversely, propagation energies increased with propagation time and conductivity. For deionized water, energy dissipation increased linearly with propagation time and a maximum of  $24 \text{ mJ}$  was dissipated. When discharges were ignited in water with elevated conductivity, the energy dissipation grew superlinearly with propagation time and increased with conductivity. A maximum of  $53 \text{ mJ}$  was dissipated at a conductivity of  $280 \mu\text{S}\cdot\text{cm}^{-1}$ .



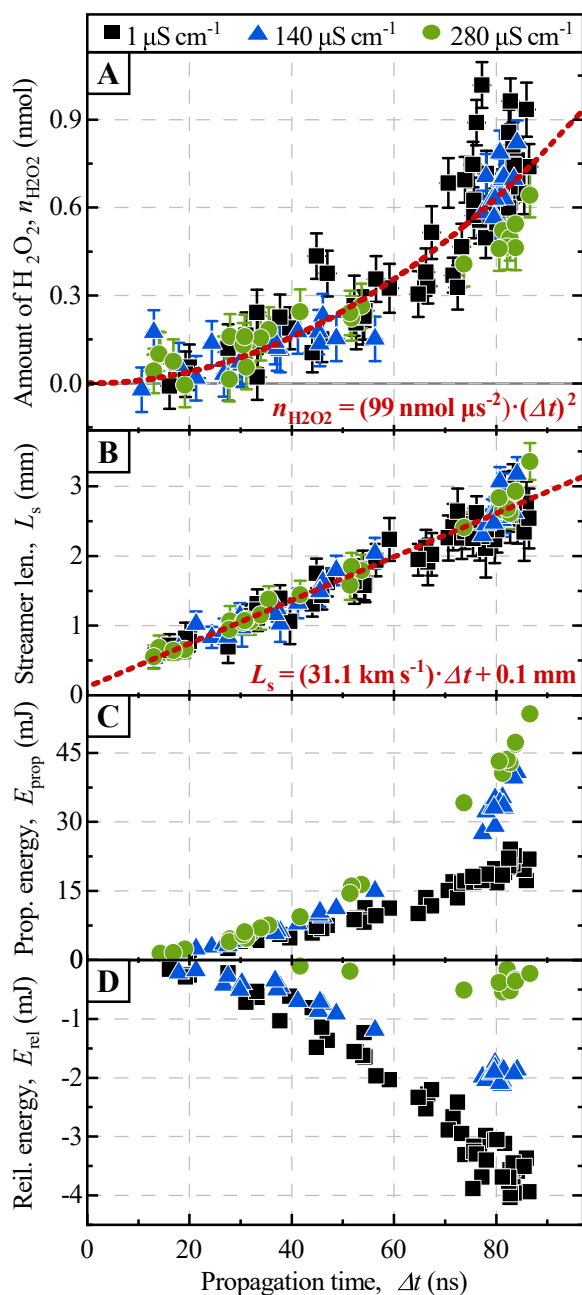


**Abbildung 3.3:** Amount of  $\text{H}_2\text{O}_2$  (Panel A), streamer lengths (Panel B), propagation energies (Panel C) and reillumination energies (Panel D) for different conductivities. The amount of hydrogen peroxide increased with propagation time, which can be described by a parabola (dashed line), and streamer lengths grew linearly. Reprinted from Article 3.

In addition, the amount of energy regained during reillumination, which increased overall with propagation time, decreased for higher conductivities. While approximately 4 mJ were recovered for the longest propagation time in deionized water, 0.5 mJ were regained for a similar propagation time and a conductivity of  $280 \mu\text{S}\cdot\text{cm}^{-1}$ . Thus, the total energy dissipated during a discharge event, which is the combination of propagation and reillumination energy, increased. Combined with hydrogen peroxide production, this resulted in a decrease in production efficiency from  $6.1 \text{ g}\cdot\text{kWh}^{-1}$  to  $1.4 \text{ g}\cdot\text{kWh}^{-1}$ .

As mentioned in the introduction of this chapter, hydrogen peroxide is commonly used to describe the chemistry induced by underwater discharges, because it is the only relatively stable product remaining in the liquid [21, 78]. However, hydroxyl production ( $\cdot\text{OH}$ ) is causative in the formation of  $\text{H}_2\text{O}_2$ , which is formed from water molecules at a rate of  $k_1 = 5.8 \cdot 10^{-9} \cdot \exp(-440 \text{ kJ}/RT)$  and then reacts with itself to form hydrogen peroxide at a rate of  $k_2 = 1.51 \cdot 10^{-11} \cdot (T/298 \text{ K})^{-0.37}$  (both rates in units of  $\text{cm}^3\cdot\text{molecule}^{-1}\cdot\text{s}^{-1}$ ,  $R$  is the universal gas constant, and  $T$  is the temperature). This means that the production of hydroxyl radicals and hydrogen peroxide is only temperature dependent, i.e. the temperature of the heavy particles (primarily neutrals) in the streamer. The production of  $\cdot\text{OH}$  increases with temperature, while the production of  $\text{H}_2\text{O}_2$  decreases. Therefore, it is generally assumed that  $\cdot\text{OH}$  is formed during the discharge expansion, while  $\text{H}_2\text{O}_2$  is produced as the channel cool. To understand hydrogen peroxide production of a discharge, it is useful to focus on  $\cdot\text{OH}$  production first. Assuming a constant production rate,  $k_{\text{OH}}$ , within a single radially symmetric streamer with an

crosssectional area,  $A_s$ , growing at velocity  $v_s$  (similar to the model in Section 2.5), the number of hydroxyl radicals,  $n_{OH}$ , produced is equal to

$$\begin{aligned} n_{OH} &= \int_0^{\Delta t} \int_0^{L_s} \int_0^{A_s} k_{OH} dAdLdt \\ &= k_{OH} A_s v_s \int_0^{\Delta t} dt \\ &= k_{OH} A_s v_s (\Delta t)^2. \end{aligned}$$

The amount of hydrogen peroxide produced in such a discharge,  $n_{H_2O_2}$ , is then proportional to  $n_{OH}$ . Assuming that hydrogen peroxide and hydroxyl radicals are linearly correlated, a proportionality factor  $c_{OH \rightarrow H_2O_2}$  can be defined and Equation 3.1 refers to  $n_{H_2O_2}$ :

$$\begin{aligned} n_{H_2O_2} &= c_{OH \rightarrow H_2O_2} \cdot k_1 \cdot A_s \cdot v_s \cdot (\Delta t)^2 \\ &= k_{H_2O_2} \cdot A_s \cdot v_s \cdot (\Delta t)^2 \end{aligned} \quad (3.1)$$

This equation was fitted to the data shown in Figure 3.3(A) and gave good agreement. Thus, the production of hydrogen peroxide can be described solely by the streamer expansion.

It is surprising that the  $H_2O_2$  production did not increase with conductivity, since an increase in energy dissipation would be expected to increase the temperature of the discharge, which would increase the production rate of  $k_1$ . As this was not observed, the temperature of the neutrals in the discharge must be similar for the different conductivities, and the additional energy must be dissipated by some other mechanism. An explanation can be motivated by the dielectric time constant,  $\tau$ , which is the ratio between the dielectric constant  $\epsilon\epsilon_0$  and the conductivity,  $\sigma$ . The constant thus represents the characteristic time at which a lossy dielectric changes between a resistive and a dielectric response. In deionized water,  $\tau$  is 7080 ns, which decreases to 50 ns and 25 ns for conductivities of  $140 \mu S \cdot cm^{-1}$  and  $280 \mu S \cdot cm^{-1}$ , respectively. Therefore, an aqueous load responds like a capacitance when a 100 ns pulse is applied for the lowest conductivity, while it shows a resistive behavior at the highest conductivity. In particular, the value of  $280 \mu S \cdot cm^{-1}$  has been chosen as  $\tau$  approximately matches the rise and fall time of the steepest pulses of 16 ns and 21 ns, respectively.

Due to a more resistive behavior, less energy can be capacitively stored in the discharge, so the reillumination energy decreases with conductivity. Therefore, no significant reillumination is observed once  $\tau$  matches the pulse fall time. This increases the energy dissipation during a discharge event and shows the importance of the dielectric time constant for discharge development. The conductive liquid surrounding the discharge could therefore be used to explain the superlinear relation between propagation time and energy dissipation in Figure 3.3(C). For short propagation times (streamer lengths  $< 1$  mm), the distance between streamer and counterelectrode was relatively large and the discharge still had a small boundary surface to the surrounding water. Therefore, the resistive losses were limited and the energy dissipation was similar for all discharges. With longer propagation, the discharges crossed up to 70% of the gap and the boundary between discharge and water increased due to strong branching. Thus, a substantial part of the increased propagation energy was dissipated into the surrounding conductive liquid, and since the hydrogen peroxide production of a discharge

was not affected, the temperatures within the discharge filaments could not have increased significantly.

#### Major findings

- For individual discharges, the concentration of hydrogen peroxide, which is unaffected by water conductivity, increases quadratically with streamer propagation time
- Constant hydroxyl radical production and constant streamer propagation velocity explain the quadratic increase in hydrogen peroxide concentration
- The decreasing energy efficiency of  $\text{H}_2\text{O}_2$  production is a result of increasing resistive losses in the water surrounding the discharge



## 4 Summary and Outlook

Pulsed streamer discharges submerged in water were studied in this thesis in order to correlate the discharge development and the chemistry induced by them. The objective was to determine, how the pulse parameters, i.e. pulse duration, pulse amplitude, and pulse steepness, affect discharge initiation, propagation, streamer morphology, and reillumination. These physical characteristics were combined with results from an experimental study of hydrogen peroxide that was produced by the discharges and characterized the induced chemistry. In particular, the effect of increased water conductivity was investigated for individual discharges. A pulsed power system was designed to ignite streamer discharges in a needle-to-plate geometry by nanosecond pulses with a pulse duration of (100-300) ns, pulse amplitude in the range of (50-64) kV, and pulse steepness characterized by three different rise and fall times between (19-35) ns and (20-43) ns, in water having conductivities ranging between (1-280)  $\mu\text{S}\cdot\text{cm}^{-1}$ . An electro-optical single discharge diagnostic, i.e. monitoring voltage, current, light intensity and imaging with a fast framing ICCD, was combined with an electrochemical method for hydrogen peroxide detection.

The discharge inception was studied statistically and it was found that the start time of discharge propagation is closely related to the pulse shape, i.e. the timing of maximum pulse amplitude, rather than the pulses rising slope. The starting of reillumination is delayed, in contrast, with longer fall time. During the propagation phase of the filaments, the propagation velocity was about  $30\text{ km}\cdot\text{s}^{-1}$  independent on pulse parameter within the range investigated in this study. The discharge morphology was similar for the different pulse steepnesses and amplitudes. With increasing pulse duration, preferential propagation in the direction of the plate electrode was observed, and the shortening of filaments propagating laterally away from the needle was associated with stopped propagation. Electrical energy was dissipated with a constant rate during propagation. The phenomenon of reillumination has been controversially discussed in the past. Hence, the post-discharge was explicitly investigated with the fast framing system and it was found that an ionization front extended at about  $200\text{ km}\cdot\text{s}^{-1}$  into preexisting discharge channels during the falling slope of the high-voltage pulse. Depending on the fall time, reillumination occurred simultaneously in all previously formed filaments for the shortest fall time and subsequently for the shallowest falling edge. Reillumination was interpreted as the process of compensation of the charge accumulated at the streamer head during propagation. Therefore, the charge transferred during reillumination could be used as a measure of the head charge of the fully developed discharge at the end of its propagation phase, which was linearly dependent on filament length. A single streamer model was developed, which combines the filaments of the highly branched discharge into a single streamer. The model explains the proportionality between head charge and streamer length, and links a smaller head charge to a reduced head potential due to a limited electrical conductivity of the streamer channel. The subsequent reillumination process for long fall times was explained

by slight differences in the head charges of the different filaments, resulting from differences in charge distribution during filament branching.

The results on the development of discharges were utilized to understand the induced chemistry of discharges in water, which was characterized by the formation of hydrogen peroxide as an indicator of the production of hydroxyl radicals. An electrochemical diagnostic was optimized to be able to detect hydrogen peroxide produced cumulatively by multiple discharges. The  $\text{H}_2\text{O}_2$  production was found to be independent of pulse steepness within the range examined in this study. The production rate increased with higher pulse amplitudes, most likely due to additional branches formed in the stronger electric field. The additional branches increased the discharge volume, which resulted in higher production rates but a constant  $\text{H}_2\text{O}_2$  production efficiency. For longer pulse durations and consequently longer propagation times, stopping some filaments that were propagating laterally to the needle axis induced branching of the other filaments due to the constant rate of energy dissipation. Increased resistive losses in the filaments with additional branches resulted in a reduced hydrogen peroxide production rate and energy efficiency. Overall, a best-case hydrogen peroxide production rate of  $0.19 \text{ mol}\cdot\text{l}^{-1}\cdot\text{s}^{-1}$  and production efficiency of  $9.2 \text{ g}\cdot\text{kWh}^{-1}$  were achieved. The electrochemical diagnostic was further optimized to observe the chemistry induced by individual discharge events. The  $\text{H}_2\text{O}_2$  production was found to depend quadratically on the propagation time. Since the streamer length and energy dissipation rate was constant, it was concluded that the radical production rate within the discharge channels was stable during propagation. The accumulated amount of hydroxyl radicals, which increased quadratically with propagation time, then reacted to hydrogen peroxide after the discharge decayed and the filaments had cooled off. An increased liquid conductivity did not influence the formation of hydrogen peroxide, even though the energy dissipation during discharge propagation increased three-fold. Considering the dielectric time constant, the increased energy dissipation for elevated conductivities was associated with resistive losses in the liquid, which did not influence the radical production inside the discharge.

The results of this study directly benefit applied sciences that utilize the induced chemistry of pulsed streamer discharges in water, e.g. for the synthesis of platform chemicals or the degradation of persistent pollutants. Within the range of pulse parameters that were investigated in this study, optimal hydrogen peroxide and, therefore, hydroxyl radical production, i.e. highest production rates and efficiencies, is obtained for steepest pulse edges, highest pulse amplitudes and pulse durations that were as long as possible to avoid stopping filaments but that were adapted to the water conductivity to avoid resistive losses. Further investigations are required to examine limits of these correlations by extending the parameter range especially towards shorter pulse durations, as the conductivity of common process water is higher than investigated in this study.

Furthermore, a 3D reconstruction of individual discharge events could make the number of filaments, branching points and the length of discharge channels accessible, which is ultimately necessary to confirm the correlation between discharge volume and hydrogen peroxide production. In addition, combining the 3D reconstruction with a study of discharge temperatures could provide more insight into the energy dissipation pathways of discharges in water with elevated conductivity. This would further elucidate the potential of the dielectric time constant as a control parameter for induced discharge chemistry.

# Literaturverzeichnis

- [1] Q. Chen, J. Li, and Y. Li. *Journal of Physics D: Applied Physics*, 48(42):424005, 2015. doi:10.1088/0022-3727/48/42/424005.
- [2] W. Bodnar, M. Schiorlin, A. Frank, T. Schulz, N. Wöhrle, C. Miron, C. Scheu, J. F. Kolb, and A. Kruth. *Applied Surface Science*, 514:145926, 2020. doi:10.1016/j.apsusc.2020.145926.
- [3] M. Ignat, P. Samoila, C. Coromelci, L. Sacarescu, I. Asaftei, V. Harabagiu, and C. Miron. *Comptes Rendus Chimie*, 21(3-4):310–317, 2018. doi:10.1016/j.crci.2017.05.006.
- [4] K. Zocher, R. Banaschik, C. Schulze, T. Schulz, J. Kredl, C. Miron, M. Schmidt, S. Mundt, W. Frey, and J. F. Kolb. *Plasma Medicine*, 6(3-4), 2016. doi:10.1615/PlasmaMed.2017019104.
- [5] K. Zocher, R. Rataj, A. Steuer, K.-D. Weltmann, and J. F. Kolb. *Journal of Physics D: Applied Physics*, 53(21):215402, 2020. doi:10.1088/1361-6463/ab768b.
- [6] B. Honnorat, V. Brüser, and J. F. Kolb. *AIP Advances*, 10(9):095025, 2020. doi:10.1063/5.0018626.
- [7] R. Zhou, R. Zhou, S. Wang, U. M. Ekanayake, Z. Fang, P. J. Cullen, K. Bazaka, and K. K. Ostrikov. *Bioresource Technology*, 318:123917, 2020. doi:10.1016/j.biortech.2020.123917.
- [8] J. Foster, B. S. Sommers, S. N. Gucker, I. M. Blankson, and G. Adamovsky. *IEEE Transactions on Plasma Science*, 40(5):1311–1323, 2012. doi:10.1109/TPS.2011.2180028.
- [9] G. R. Stratton, F. Dai, C. L. Bellona, T. M. Holsen, E. R. V. Dickenson, and S. Mededovic Thagard. *Environmental science & technology*, 51(3):1643–1648, 2017. doi:10.1021/acs.est.6b04215.
- [10] J. O. Tijani, O. O. Fatoba, G. Madzivire, and L. F. Petrik. *Water, Air, & Soil Pollution*, 225(9):1–30, 2014. doi:10.1007/s11270-014-2102-y.
- [11] J. E. Foster. *Physics of Plasmas*, 24(5):055501, 2017. doi:10.1063/1.4977921.
- [12] F. Rezaei, P. Vanraes, A. Nikiforov, R. Morent, and N. De Geyter. *Materials*, 12(17):2751, 2019. doi:10.3390/ma12172751.
- [13] M. Schneider, R. Rataj, J. F. Kolb, and L. Bláha. *Environmental Pollution*, 266:115423, 2020. doi:10.1016/j.envpol.2020.115423.
- [14] M. Schneider and L. Bláha. *Environmental Sciences Europe*, 32(1):1–24, 2020. doi:10.1186/s12302-020-00371-0.

- [15] M. Schneider, R. Rataj, L. Bláha, and J.F. Kolb. Experimental review of different plasma technologies for the degradation of cylindrospermopsin as model water pollutant. *Chemical Engineering Journal*, page 138984, 2022. doi:10.1016/j.cej.2022.138984.
- [16] R. Banaschik, F. Koch, J.F. Kolb, and K.-D. Weltmann. *IEEE Transactions on Plasma Science*, 42(10):2736–2737, 2014. doi:10.1109/TPS.2014.2325977.
- [17] R. Banaschik, P. Lukes, H. Jablonowski, M. U. Hammer, K.-D. Weltmann, and J. F. Kolb. *Water Research*, 84:127–135, 2015. doi:10.1016/j.watres.2015.07.018.
- [18] R. Banaschik, P. Lukes, C. Miron, R. Banaschik, A.V. Pipa, K. Fricke, P.J. Bednarski, and J.F. Kolb. *Electrochimica Acta*, 245:539–548, 2017. doi:10.1016/j.electacta.2017.05.121.
- [19] R. Banaschik, H. Jablonowski, P.J. Bednarski, and J.F. Kolb. *Journal of hazardous materials*, 342:651–660, 2018. doi:10.1016/j.jhazmat.2017.08.058.
- [20] P. Bruggeman and C. Leys. *Journal of Physics D: Applied Physics*, 42(5):28, 2009. doi:10.1088/0022-3727/42/5/053001.
- [21] B.R. Locke and S.M. Thagard. *Plasma Chemistry and Plasma Processing*, 32(5):875–917, 2012. doi:10.1007/s11090-012-9403-y.
- [22] R.P. Joshi and S. Mededovic Thagard. *Plasma Chemistry and Plasma Processing*, 33(1):1–15, 2013. doi:10.1007/s11090-012-9425-5.
- [23] P. Lukeš, A.T. Appleton, and B.R. Locke. *IEEE Transactions on Industry Applications*, 40(1):60–67, 2004. doi:10.1109/TIA.2003.821799.
- [24] P. Lukeš, M. Clupek, V. Babicky, and P. Sunka. *Plasma sources science and technology*, 17(2):024012, 2008. doi:10.1088/0963-0252/17/2/024012.
- [25] P. Lukeš, M. Clupek, V. Babicky, I. Sisrova, and V. Janda. *Plasma Sources Science and Technology*, 20(3):034011, 2011. doi:10.1088/0963-0252/20/3/034011.
- [26] S. Medodovic Thagard, K. Takashima, and A. Mizuno. *Plasma Chemistry and Plasma Processing*, 29(6):455, 2009. doi:10.1007/s11090-009-9195-x.
- [27] M. Sahni and B. R. Locke. *Plasma Processes and Polymers*, 3(4-5):342–354, 2006. doi:10.1002/ppap.200600006.
- [28] S. Medodovic and B. R. Locke. *Journal of Physics D: Applied Physics*, 42(4):049801, 2009. doi:10.1088/0022-3727/42/4/049801.
- [29] L. Chauvet, C. Nenbangkao, K. Grosse, and A. von Keudell. *Plasma Processes and Polymers*, 17(6):1900192, 2020. doi:10.1002/ppap.201900192.
- [30] S. Nijdam, J. Teunissen, and U. Ebert. *Plasma Sources Science and Technology*, 29(10):103001, 2020. doi:10.1088/1361-6595/abaa05.



- [31] L.B. Loeb and J.M. Meek. *Journal of applied physics*, 11(6):438–447, 1940. doi:10.1063/1.1712792.
- [32] J.M. Meek. *Physical review*, 57(8):722, 1940. doi:10.1103/PhysRev.57.722.
- [33] A. Fridman, A. Gutsol, and Y.I. Cho. *Advances in Heat Transfer*, 40:1–142, 2007. doi:10.1016/S0065-2717(07)40001-6.
- [34] P.J. Bruggeman, F. Iza, and R. Brandenburg. *Plasma Sources Science and Technology*, 26(12):123002, 2017. doi:10.1088/1361-6595/aa97af.
- [35] S. Nijdam, G. Wormeester, E.M. Van Veldhuizen, and U. Ebert. *Journal of Physics D: Applied Physics*, 44(45):455201, 2011. doi:10.1088/0022-3727/44/45/455201.
- [36] J.F. Kolb, R.P. Joshi, S. Xiao, and K.H. Schoenbach. *Journal of Physics D: Applied Physics*, 41(23):234007, 2008. doi:10.1088/0022-3727/41/23/234007.
- [37] D. Dobrynin, Y. Seepersad, M. Pekker, M. Shneider, G. Friedman, and A. Fridman. *Journal of Physics D: Applied Physics*, 46(10):105201, 2013. doi:10.1088/0022-3727/46/10/105201.
- [38] U. Ebert, C. Montijn, T.M.P. Briels, W. Hundsdorfer, B. Meulenbroek, A. Rocco, and E.M. van Veldhuizen. *Plasma Sources Science and Technology*, 15(2):S118, 2006. doi:10.1088/0963-0252/15/2/S14.
- [39] T. Huiskamp, W. Sengers, F.J.C.M. Beckers, S. Nijdam, U. Ebert, E.J.M. Van Heesch, and A.J.M. Pemen. *Plasma Sources Science and Technology*, 26(7):075009, 2017. doi:10.1088/1361-6595/aa7587.
- [40] T.M.P. Briels, J. Kos, E.M. van Veldhuizen, and U. Ebert. *Journal of Physics D: Applied Physics*, 39(24):5201, 2006. doi:10.1088/0022-3727/39/24/016.
- [41] U. Ebert, S. Nijdam, C. Li, A. Luque, T. Briels, and E. van Veldhuizen. *Journal of Geophysical Research: Space Physics*, 115(A7), 2010. doi:10.1029/2009JA014867.
- [42] B.R. Locke, M. Sato, P. Sunka, M.R. Hoffmann, and J.-S. Chang. *Industrial & engineering chemistry research*, 45(3):882–905, 2006. doi:10.1021/ie050981u.
- [43] W. An, K. Baumung, and H. Bluhm. *Journal of applied physics*, 101(5):053302, 2007. doi:10.1063/1.2437675.
- [44] I. Marinov, O. Guaitella, A. Rousseau, and S. M. Starikovskaia. *Journal of Physics D: Applied Physics*, 46(46):464013, 2013. doi:10.1088/0022-3727/46/46/464013.
- [45] I. Marinov, S. Starikovskaia, and A. Rousseau. *Journal of Physics D: Applied Physics*, 47(22):224017, 2014. doi:10.1088/0022-3727/47/22/224017.
- [46] J. N. Salazar, N. Bonifaci, A. Denat, and O. Lesaint. In *Dielectric Liquids, 2005. ICDL 2005. 2005 IEEE International Conference on*, page 91. IEEE, 2005.

- [47] P.H. Ceccato, O. Guaitella, M.R. Le Gloahec, and A. Rousseau. *Journal of Physics D: Applied Physics*, 43(17):175202, 2010. doi:10.1088/0022-3727/43/17/175202.
- [48] H. Fujita, S. Kanazawa, K. Ohtani, A. Komiya, T. Kaneko, and T. Sato. *Journal of Applied Physics*, 116(21):213301, 2014. doi:10.1063/1.4902862.
- [49] R. Rataj, H. Höft, and J.F. Kolb. *Plasma Sources Science and Technology*, 28(12):125002, 2019. doi:10.1088/1361-6595/ab54e0.
- [50] R. Rataj, M. Werneburg, H. Below, and J.F. Kolb. *Plasma Sources Science and Technology*, 31(10):105005, 2022. doi:10.1088/1361-6595/ac942a.
- [51] K. Grosse, J. Held, M. Kai, and A. von Keudell. *Plasma Sources Science and Technology*, 28(8):085003, 2019. doi:10.1088/1361-6595/ab26fc.
- [52] A. von Keudell, K. Grosse, and V. Schulz-von der Gathen. *Plasma Sources Science and Technology*, 29(8):085021, 2020. doi:10.1088/1361-6595/aba4b9.
- [53] K. Grosse, V. Schulz-von der Gathen, and A. von Keudell. *Plasma Sources Science and Technology*, 29(9):095008, 2020. doi:10.1088/1361-6595/aba487.
- [54] J. Qian, R.P. Joshi, J. Kolb, K.H. Schoenbach, J. Dickens, A. Neuber, M. Butcher, M. Cevallos, H. Krompholz, and E. Schamiloglu. *Journal of Applied Physics*, 97(11):113304, 2005. doi:10.1063/1.1921338.
- [55] F. Booth. *The Journal of Chemical Physics*, 19(4):391–394, 1951. doi:10.1063/1.1748233.
- [56] I.-C. Yeh and M. L. Berkowitz. *The Journal of chemical physics*, 110(16):7935–7942, 1999. doi:10.1063/1.478698.
- [57] Mikhail Pekker and Mikhail N Shneider. *Journal of Physics D: Applied Physics*, 48(42):424009, 2015. doi:10.1088/0022-3727/48/42/424009.
- [58] A. Sun, C. Huo, and J. Zhuang. *High Voltage*, 1(2):74–80, 2016. doi:10.1049/hve.2016.0016.
- [59] N. Y. Babaeva, D. V. Tereshonok, G. V. Naidis, and B. M. Smirnov. *Journal of Physics D: Applied Physics*, 49(2):025202, 2015. doi:10.1088/0022-3727/49/2/025202.
- [60] R.P. Joshi, J.F. Kolb, S. Xiao, and K.H. Schoenbach. *Plasma Processes and Polymers*, 6(11):763–777, 2009. doi:10.1002/ppap.200900022.
- [61] T.J. Lewis. *IEEE Transactions on Dielectrics and Electrical Insulation*, 5(3):306–315, 1998. doi:10.1109/94.689419.
- [62] D. V. Tereshonok, N. Y. Babaeva, G. V. Naidis, and B. M. Smirnov. *Journal of Physics D: Applied Physics*, 49(50):505501, 2016. doi:10.1088/0022-3727/49/50/505501.
- [63] B. Pongrác, M. Šimek, M. Člupek, V. Babický, and P. Lukeš. *Journal of Physics D: Applied Physics*, 51(12):124001, 2018. doi:10.1088/1361-6463/aaabb1.

- [64] L. Schaper, W. G. Graham, and K. R. Stalder. *Plasma Sources Science and Technology*, 20(3):034003, 2011. doi:10.1088/0963-0252/20/3/034003.
- [65] H. Fujita, S. Kanazawa, K. Ohtani, A. Komiya, and T. Sato. *Journal of Applied Physics*, 113(11):113304, 2013. doi:10.1063/1.4795765.
- [66] P. Lukeš. *Institute of Plasma Physics AS CR, Prague, Czech Republic*, 2001.
- [67] A. Starikovskiy, Y.g Yang, Y. I. Cho, and A. Fridman. *Plasma Sources Science and Technology*, 20(2):024003, 2011. doi:10.1088/0963-0252/20/2/024003.
- [68] M. N. Shneider and M. Pekker. *Journal of Applied Physics*, 114(21):214906, 2013. doi:10.1063/1.4840935.
- [69] M. N. Shneider and M. Pekker. *Physical Review E*, 87(4):043004, 2013. doi:10.1103/PhysRevE.87.043004.
- [70] M. Pekker, Y. Seepersad, M. N. Shneider, A. Fridman, and D. Dobrynin. *Journal of Physics D: Applied Physics*, 47(2):025502, 2013. doi:10.1088/0022-3727/47/2/025502.
- [71] Y. Seepersad, A. Fridman, and D. Dobrynin. *Journal of Physics D: Applied Physics*, 48(42):424012, 2015. doi:10.1088/0022-3727/48/42/424012.
- [72] M. N. Shneider and M. Pekker. *Journal of Applied Physics*, 117(22):224902, 2015. doi:10.1063/1.4922244.
- [73] M. N. Shneider and M. Pekker. *Optics letters*, 41(6):1090–1093, 2016. doi:10.1364/OL.41.001090.
- [74] M. Šimek, P. Hoffer, J. Tungli, V. Prukner, J. Schmidt, P. Bílek, and Z. Bonaventura. *Plasma Sources Science and Technology*, 29(6):064001, 2020. doi:10.1088/1361-6595/ab87b7.
- [75] M. Šimek, P. Hoffer, V. Prukner, and J. Schmidt. *Plasma Sources Science and Technology*, 29(9):095001, 2020. doi:10.1088/1361-6595/abac49.
- [76] B. Pongráč, M. Šimek, P. Ondáč, M. Člupek, V. Babický, and P. Lukeš. *Plasma Sources Science and Technology*, 28(2):02LT02, 2019. doi:10.1088/1361-6595/aae91f.
- [77] V. Prukner, J. Schmidt, P. Hoffer, and M. Šimek. *Plasma*, 4(1):183–200, 2021. doi:10.3390/plasma4010011.
- [78] S. Mededovic and B. R. Locke. *Applied Catalysis B: Environmental*, 67(3-4):149–159, 2006. doi:10.1016/j.apcatb.2006.05.001.
- [79] A.A. Joshi, B.R. Locke, P. Arce, and W. C. Finney. *Journal of hazardous materials*, 41(1):3–30, 1995. doi:10.1016/0304-3894(94)00099-3.
- [80] S. Yang, L. Zhang, F. Cui, and J. Ma. In *2009 3rd international conference on bioinformatics and biomedical engineering*, pages 1–4. IEEE, 2009. doi:10.1109/ICBBE.2009.5163248.

- [81] S. Li, S. Hu, and H. Zhang. *IEEE Transactions on Plasma Science*, 40(1):63–67, 2011. doi:10.1109/TPS.2011.2172214.
- [82] J. Wen, Y. Li, M. Zhang, and G. Zhang. In *2019 IEEE 20th International Conference on Dielectric Liquids (ICDL)*, pages 1–4. IEEE, 2019. doi:10.1109/ICDL.2019.8796626.
- [83] T.S. Nguyen, C. Rond, A. Vega, X. Duten, and S. Forget. *Plasma Chemistry and Plasma Processing*, 40:955–969, 2020. doi:10.1007/s11090-020-10084-0.
- [84] A.T. Sugiarto and T. Ohshima. In *2015 International Conference on Automation, Cognitive Science, Optics, Micro Electro-Mechanical System, and Information Technology (ICACOMIT)*, pages 176–180. IEEE, 2015. doi:10.1109/ICACOMIT.2015.7440201.
- [85] T. H. Dang, A. Denat, O. Lesaint, and G. Teissedre. *Plasma Sources Science and Technology*, 17(2):024013, 2008. doi:10.1088/0963-0252/17/2/024013.
- [86] M. Sato, T. Ohgiyama, and J.S. Clements. *IEEE Transactions on Industry applications*, 32(1):106–112, 1996. doi:10.1109/28.485820.
- [87] J. Qin and V.P. Pasko. *Journal of Physics D: Applied Physics*, 47(43):435202, 2014. doi:10.1088/0022-3727/47/43/435202.
- [88] W Deutsch. *Analen der Physik*, 5(16):588–612, 1933. doi:10.1002/andp.19334080508.
- [89] B.R. Locke and K.-Y. Shih. *Plasma Sources Science and Technology*, 20(3):034006, 2011. doi:10.1088/0963-0252/20/3/034006.

# Original Publications

The following list contains all publications forming the foundation of this PhD thesis. Detailed descriptions on the authors contribution to the articles are given below the title.

## Article 1

Rataj, R., Höft, H., and Kolb, J. F.: Reillumination of Submicrosecond Pulsed Corona-like Discharges in Water, *Plasma Sources Science and Technology*, 28.12, 2019

R. Rataj built the experimental setup, performed all measurements and analysed the data. R. Rataj also prepared the figures and wrote the article. All authors discussed the results and edited the article.

---

## Article 2

Rataj, R., Werneburg, M., Below, H., and Kolb, J. F.: Hydrogen Peroxide Production of Underwater Nanosecond-pulsed Streamer Discharges with Respect to Pulse Parameters and Associated Discharge Characteristics, *Plasma Sources Science and Technology*, 31.10, 2022

R. Rataj built the setup for the discharge experiments and optimized the setup for the hydrogenperoxide measurement, which was built by H. Below. R. Rataj performed the measurements with help of M. Werneburg and analysed the data. R. Rataj prepared the figures and wrote the article. All authors discussed the results and edited the article.

---

## Article 3

Rataj, R., Werneburg, M., Below, H., and Kolb, J. F.: Hydrogen Peroxide Production of Individual Nanosecond Pulsed Discharges Submerged in Water of Elevated Conductivity, accepted by *ChemPhysChem*, 2023

R. Rataj built the setup for the discharge experiments and optimized the setup for the hydrogenperoxide measurement, which was built by H. Below. R. Rataj performed the measurements with help of M. Werneburg and analysed the data. R. Rataj prepared the figures and wrote the article. All authors discussed the results and edited the article.

Rostock, 14. September 2023

.....  
Prof. Dr. Jürgen F. Kolb

.....  
Raphael Rataj



## Article 1

### Authors

Raphael Rataj  
Hans Höft  
Jürgen F. Kolb

### Title

Reillumination of submicrosecond pulsed corona-like discharges in water

### Journal

Plasma Sources Science and Technology, Volume 28, Number 12

Online: <https://iopscience.iop.org/article/10.1088/1361-6595/ab54e0/meta>

DOI: <https://doi.org/10.1088/1361-6595/ab54e0>

Reprinted with kind permission from:

Plasma Sources Sci. Technol. 28.12, 2019,

Copyright by IOP Publishing Limited. ©IOP Publishing. Reproduced with permission.

All rights reserved.





# Reillumination of submicrosecond pulsed corona-like discharges in water

Raphael Rataj<sup>1,2</sup> , Hans Höft<sup>1</sup>  and Juergen F Kolb<sup>1,2</sup> 

<sup>1</sup>Leibniz Institute for Plasma Science and Technology (INP), Felix-Hausdorff-Str. 2, D-17489, Greifswald, Germany

<sup>2</sup>Institute of Physics, University of Rostock, Albert-Einstein-Str. 23-24, D-18059, Rostock, Germany

E-mail: [juergen.kolb@inp-greifswald.de](mailto:juergen.kolb@inp-greifswald.de)

Received 31 July 2019, revised 18 October 2019

Accepted for publication 6 November 2019

Published 3 December 2019



CrossMark

## Abstract

Pronounced reilluminations can be observed for discharges that are generated in water by submicrosecond high-voltage pulses. This phenomenon can appear during the decrease of the applied voltage, depending on the pulse characteristics, especially fall times. The respective processes are expected to be crucial for optical investigations of discharge characteristics and also for applications. Accordingly, the development of individual corona-like discharges in water was investigated in a needle-to-plate geometry for their ignition by single rectangular high-voltage pulses with a duration of 100 ns. The pulse amplitudes of about 50 kV and adjusted pulse fall times of 20, 26, and 43 ns were used. Voltages, currents and light emissions were synchronized with subsequent images of individual discharge events. Two distinct stages, a propagation phase and a reillumination phase, were identified. The individual discharges expanded for all investigated fall times with the same velocity of  $(29 \pm 2) \text{ km s}^{-1}$ . No significant differences of streamer morphologies and electrical characteristics were observed for the propagation phase. As the voltage began to decrease, light emissions first went through a minimum before increasing again. The following maxima were strongly dependent on fall times. Corresponding images showed that discharge channels were reilluminated within 6 ns. However, not all of the previously observed filaments reignited at once for longer fall times and instead single channels reilluminated subsequently. The development of reillumination can be explained from the external electric field in the electrode gap during the streamer propagation, which determines the head charge distributions at the discharge channel ends. This space charges generate an internal electrical field in the filaments resulting in the reillumination during the falling edge of the applied high-voltage pulse.

Keywords: plasma in water, electrical discharge, prebreakdown, nanosecond discharge, pulsed power

## 1. Introduction

Corona-like discharges that are generated directly in water are currently utilized for the development of a number of applications, e.g. the synthesis of nanoparticles [1], degradation of chemical compounds in water [2], and the extraction of heat-sensitive compounds from algae [3]. These technologies benefit from specific properties of discharges in liquids and most of them increase their efficiency by applying high-voltage pulses of a few microseconds or even subnanosecond duration.

Notably, the physics of those discharges is different in comparison to gas discharges and, yet, not fully understood

[4, 5]. For example, the behavior of corona-like discharges in water is rather unique during the end of an applied positive and rectangular high-voltage pulse. In contrast to positive streamers in a gaseous medium, discharge channels in liquids can reignite during the voltage decrease [6]. This phenomenon is often described as ‘reillumination’. However, this rekindling of the entire discharge should not be confused with the reillumination of only single channels as it is observed during the propagation of microsecond pulsed corona-like discharges in liquids. The light emitted for the reillumination phase is generally comparable to the overall emission that can be collected during the propagation and development of the

preceding discharge, i.e. while high-voltage amplitudes are still sustained [6].

The reillumination of discharges in water has not been investigated in much detail or taken into account in discharge-studies although spectroscopic investigations are eminently affected. Often reported are especially time-integrated measurements and, therefore, the emissions of propagating filaments and reillumination are generally superimposed [6, 7]. Interestingly, reillumination does not occur in all experiments [7, 8] or was at least not observed for all channels [9], even for applied voltage pulses with comparable duration.

When reillumination was explained, it was from temporal- and spatial-resolved images that were, however, accumulated for several discharge events [8, 9]. Accordingly, the associated backstroke results from the space charge forming at the head of discharge channels [8–11]. When the voltage decreases rather rapidly, i.e. for short fall times, ions are not able to readily recombine or diffuse back into the discharge channel [12]. Consequently, the electric field in the preionized channel increases and electrons are accelerated towards the space charge. Conversely, electrons are then able to gain sufficient energy to ignite a channel again.

As a consequence, the main factors that are responsible for the emergence of reillumination are pulse fall times, electrode potential, formation processes of streamer head charges, as they are associated with ion generation and recombination processes, and the conductivity of the aqueous electrolyte. However, to understand details of dynamics and mechanisms, the temporal development of reillumination has to be visualized for individual discharges depending on these parameters. Information on transferred charge, dissipated energy and their relation with different voltage shapes could then be compared with the spatial development of the discharge.

Accordingly, reillumination was investigated in this study with respect to different fall times for single 100 ns positive high-voltage pulses that were applied to a needle-to-plate electrode configuration. The results suggest that the pulse duration is in fact not crucial for the reillumination phenomenon, as long as it is in a comparable, i.e. sub-microsecond, range. A pulse generator was developed that allowed to control fall times between 20 and 43 ns at constant pulse width. Discharge current, transferred charge, dissipated energy, and emitted light intensity were obtained for individual discharges and associated with consecutive images of the reillumination phase. A hypothesis is presented, how reillumination depends especially on the pulse fall times.

## 2. Experimental setup

A plasma chamber for a needle-to-plate electrode geometry was developed for detailed simultaneous optical and electrical diagnostic. The main components of the setup are shown by a block diagram in figure 1.

### 2.1. Discharge chamber and high-voltage pulse generation

A needle electrode was made from a tungsten rod of 2 mm in diameter (99.95% purity, *Metall Maier*), which was electrochemically sharpened to a tip with a curvature radius of 40  $\mu\text{m}$ . The tip was conditioned with 250 corona discharges to obtain a reproducible and stable surface structure before the actual experiments were conducted. For insulation, a PTFE (Polytetrafluoroethylene) hollow cylinder with a wall thickness of 1 mm was press-fitted on the needle, ending 5 mm from the needle tip.

A titanium plate (99.5%, *Selfan Fine + Metal GmbH*) with a diameter of 46 mm, a thickness of 5 mm and a rounded edge was the counter electrode. Both electrodes were mounted in a PMMA (Polymethylmethacrylat) chamber, containing a total volume of 100 ml. The distance between needle and plate was adjusted by a manipulator and set to  $(10 \pm 0.2)$  mm.

During the experiments, deionized water was flowing continuously with  $120 \text{ ml min}^{-1}$  through the chamber from the bottom to an outlet at the top. The resistance of the discharge chamber was matched to the impedance of the pulse generator with a high-voltage 250  $\Omega$ -resistor connected in parallel to the electrode gap.

An custom-build, stacked Blumlein-line pulse generator with two individual lines was used to apply rectangular high-voltage pulses with a duration of 100 ns (FWHM) and an amplitude of 50 kV. After the RG217-cables had been charged, a pressurized spark gap switch shortened the circuit. The amplitude of the resulting high-voltage pulses varied slightly, since the breakdown voltage of the switch was slightly varying within 7% of the set voltage. These statistical variations were taken into account and, actually, utilized in the evaluation of measurements and observations. Since impedances of discharge chamber and pulse generator were matched, only a single pulse was applied and no reflections were observed. Hence, only a single discharge was initiated with a frequency of 1 Hz. The continuous water flow guaranteed that the medium in the gap was refreshed between discharges.

The fall time of the pulses could be adjusted by connecting an additional inductance in series between the spark gap switch and pulse forming line. Thus, it was possible to increase the fall time from 20 ns up to 60 ns, as defined by the time for the applied voltage to drop from 90% to 10% of the mean pulse amplitude. Using four straight wires, coils with an inductance of 100 or 267 nH, fall times of 20, 26 and 43 ns were achieved. Pulse rise times were also changing together with fall times and were 19 ns, 24 ns and 35 ns, respectively.

The spark gap switch could not be triggered. Therefore, a delay line of 127 ns, connecting the pulse generator with the electrodes, was necessary to synchronize optical and electrical diagnostics. A trigger signal could be derived from the breakdown of the spark gap switch that was sufficiently ahead of the pulse applied to the electrodes to ready the measurement system.

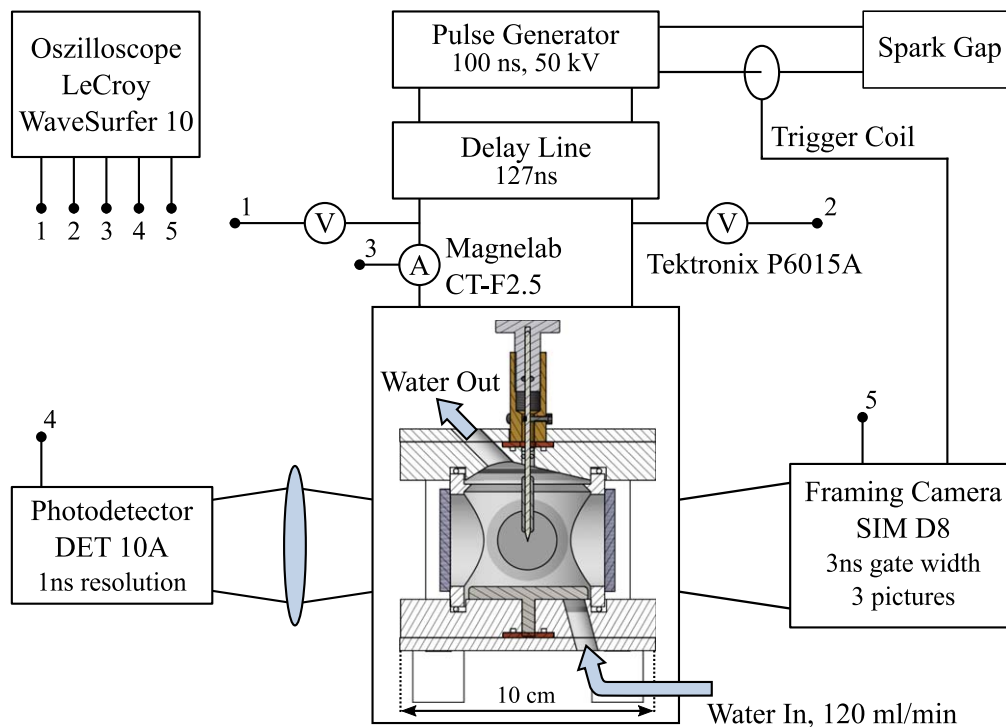


**Figure 1.** Block diagram of the setup for the investigation of discharges in water. Pulsed corona-like discharges were generated in a needle-to-plate electrode configuration with a Blumlein-line pulse generator. Measurements of electric parameters were made with two high-voltage probes and a current monitor. The light emission of single discharges was observed with a photodetector and a framing camera. The camera recorded consecutive images of the discharge development that were synchronized with the electrical measurements.

## 2.2. Electrical and optical diagnostics

According to the design of the Blumlein-line pulse generator, both needle and plate electrode were biased with a transient potential, different from ground potential, during the application of a pulse. The pulse was defined by the potential difference between both electrodes. Two similar passive high-voltage probes (P6015A, *Tektronix*) were used for a differential measurement of the voltage across the gap. The current was monitored with a Rogowski coil (CT-F2.5, *Magnelab*) around the connection to the plate electrode (reference ground). Voltage and current were recorded with an oscilloscope (WaveSurfer 10, *LeCroy*). A photodetector (DET 10A, *ThorLabs*) with a temporal resolution of 1 ns was selected to record the development of spatially integrated intensities for the light emitted from discharges and the light was focused on the sensor by two lenses. The different individual signals were all corrected for optical and cable-delays.

Images of the discharge development were taken with a framing camera (SIM D8, *Specialised Imaging Ltd.*). Beam splitters separate and guide the optical information to three independent ICCD's, which can be triggered individually. Accordingly, the progression of a single discharge could be recorded in three consecutive images depending on the delay between trigger signals. The minimum gate width of 3 ns was set for every ICCD and all recordings in each experiment. The delay between the recorded images was adjusted according to the development of voltage, current and light signals. The optical paths, the beam splitters, and the different ICCD's were not comparable, i.e. every image was recorded for different

incoming light intensities and sensor sensitivities. Hence, the intensity of structures in the images were not the same, even if the pictures were taken at the same moment. Accordingly, an intensity correction factor for each channel was determined from 25 discharges that were recorded with all ICCD's triggered simultaneously to record the same moment. The derived respective average intensity-offsets for the different channels were then consistently applied toward image analysis.

## 2.3. Analysis of light emissions and discharge currents

The spark gap switch, the pulse generator and the discharge itself were sources of considerable electromagnetic noise, which interfered with the measurements. Especially, the photodetector recorded radiated electromagnetic fields. This background signal was linearly dependent on the breakdown voltage across the spark gap switch and, therefore, depending on the amplitude of the applied voltage pulse. Measurements of this background signal with a screen blocking the optical path between needle and detector allowed for a correction. An average of 50 measurements was collected to improve the signal-to-noise-ratio and the respective averaged baseline signal was subtracted for measurements of investigated discharges.

A similar method was applied for measurements of discharge currents. In general, a displacement current is always superimposed to the actual discharge current. The displacement current was one order of magnitude larger than the discharge current. However, the displacement current is proportional to the first derivative in time of the voltage across the electrode gap and determined by the dielectric medium.

Therefore, the amplitude of this current for a specific pulse amplitude can be determined independently from a discharge event. 50 pulses with an amplitude for which no discharge were observed to obtain an average signal for the displacement current. This reference was then scaled with respect to pulse amplitudes and subtracted from the currents measured for a discharge event to derive the actual discharge current. Another error would be introduced by this correction, if the reference displacement current and the currents of investigated discharges were not precisely synchronized. Therefore, an iterative correction was performed based on the respective voltages associated with the currents. Reference displacement current and measured current were hereby shifted against each other in time, until their difference was minimized.

### 3. Results

The reillumination of discharges, which were generated in water by 100 ns high-voltage pulses, was investigated for different fall times of 20, 26 and 43 ns. Images of discharges were obtained and propagation velocities were calculated to investigate the development of the filamentary structure (section 3.1). Reillumination events were characterized by temporal resolved measurements for voltages, discharge currents and emitted light intensities (section 3.2). Derived discharge energies and the charge that was transferred during reignition were derived from the measurements (sections 3.3 and 3.4, respectively). Finally, the spatial development of reillumination was studied in detail from subsequent and consecutive images of individual events (section 3.5).

#### 3.1. Streamer channel structure and propagation for single discharge events

Typical images that were obtained for the different fall times at the end of the applied pulses are shown in figure 2. The light intensity was highest close to the needle tip from where filaments originated and spread out radially. There seemed to be only a slight preference for the propagation towards the far away ground electrode with some filaments appearing a little brighter.

Channels were branching during the propagation with an increasing number of branching points for greater distance from the tip and especially towards the very end of the propagation. However, the overall morphology of the discharges initially was independent from a particular pulse shape.

The spatial development of individual discharges was observed by taking three consecutive images and typical recordings are shown in figure 3. The images were recorded with a gate opening time of 3 ns for each picture and with a delay of 20 ns between the first and second image and a delay of 15 ns between the second and third image, respectively. Additionally, associated radial intensity profiles are presented, which were derived to measure the spherical expansion of the discharge, i.e. the intensity was averaged along a semi-circle for a given distance from the needle tip. In general, local

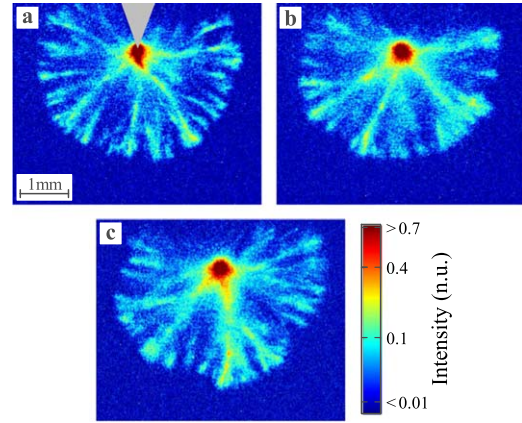


**Figure 2.** Corona-like discharges in water generated around a  $40 \mu\text{m}$  needle tip by the application of a positive 100 ns high-voltage pulse with different fall times: (a) 20 ns (image taken 98 ns after pulse onset), (b) 26 ns (image taken 105 ns after pulse onset), (c) 43 ns (image taken 107 ns after pulse onset). All images were recorded with a 3 ns gate width and intensities were normalized with respect to the maximum possible pixel value (4095).

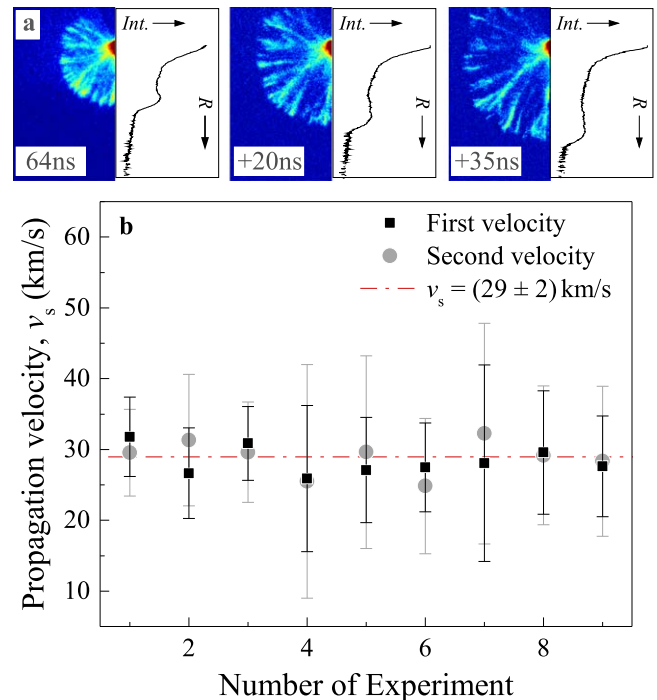


**Figure 3.** (a) Subsequent framing camera images for an individual discharge (gate opening time of 3 ns, 20 ns delay between first and second image and 15 ns delay between second and third image) together with profiles for the accumulated intensity, *Int.*, at a given distance, *R*, from the needle tip. (b) Radial streamer propagation velocity determined from these images. The velocity was calculated from the respective delay and the mean channel lengths for two subsequent images.

intensities decreased with increasing distance from the tip. At the end of the channel, i.e. at the streamer heads, the intensities intermediately peaked again and then rapidly dropped. The respective bend in the slopes of the intensity profiles



determined a mean channel length. From the lengths, which were obtained from each of the three images, a first and second propagation velocity for the streamer heads could be determined with respect to the delay between the pictures, which are shown in the lower diagram of figure 3.

Within the accuracy of the method, a constant propagation velocity was determined for the expansion. No significant differences were observed that could be related to different fall times. Accordingly, the mean propagation velocity,  $v_s$ , was approximately  $(29 \pm 2) \text{ km s}^{-1}$  for a fall time of 20 ns and  $(28 \pm 1) \text{ km s}^{-1}$  and  $(29 \pm 1) \text{ km s}^{-1}$  for fall times of 26 ns and 43 ns, respectively. These values represent a lower limit for the propagation velocity due to the projection of the three-dimensional discharge into the image plane.

### 3.2. Time-resolved electrical characteristics and associated light emission

Voltage, current and development of light intensity were recorded for every individual discharge. Examples for measurements for the different fall times of 20, 26 and 43 ns are shown in figure 4 for an applied high-voltage pulse with a mean amplitude of 47 kV. Due to the parasitic impedance of the overall electrical setup, voltage amplitudes were not entirely constant and dropped during the pulse. Therefore, an average mean voltage,  $U_{\text{mean}}$ , was calculated as reference value. The trailing edge of the pulse had an approximately linear slope, with voltages eventually decreasing to zero. The corresponding fall time,  $t_{\text{fall}}$ , was defined as the time needed for the voltage to decrease from 90% to 10% of the mean amplitude. The deliberately included inductances that were used to control fall times also affected pulse rise times. However, the corresponding rise times of 19, 24 and 35 ns did not have an appreciable effect on the discharge development as observed either by the acquired images (see section 3.1), the discharge currents or the recorded light intensities. Typical applied high-voltage pulses with a similar pulse amplitude but different rise and fall times are shown in figure 4(a) together with an illustration of definitions for timing information and other relevant parameters.

The discharge currents,  $I$ , that are associated with these voltages are presented in figure 4(b). The displacement currents, which were approximately one order of magnitude higher, were already subtracted as described in section 2. Currents started to increase during the application of high-voltages. However, afflicted by a statistical time lag, the time for the onset of a discharge,  $t_{\text{start}}$ , not necessarily corresponded to the start of a pulse or the maximum of the pulse amplitudes. At first, currents followed the voltage with the same polarity and gradually increased, which reflects the discharge propagation. As the voltage dropped, also the discharge currents declined, reversed polarity and decreased to minimum values before increasing again. The oscillations that appear in the current signals were apparently a characteristic of the overall setup and can at a closer look also be identified with the same frequency in the voltage recordings. The period of these small oscillations can be explained by an LC-circuit, which is formed by impedance of the discharge chamber and

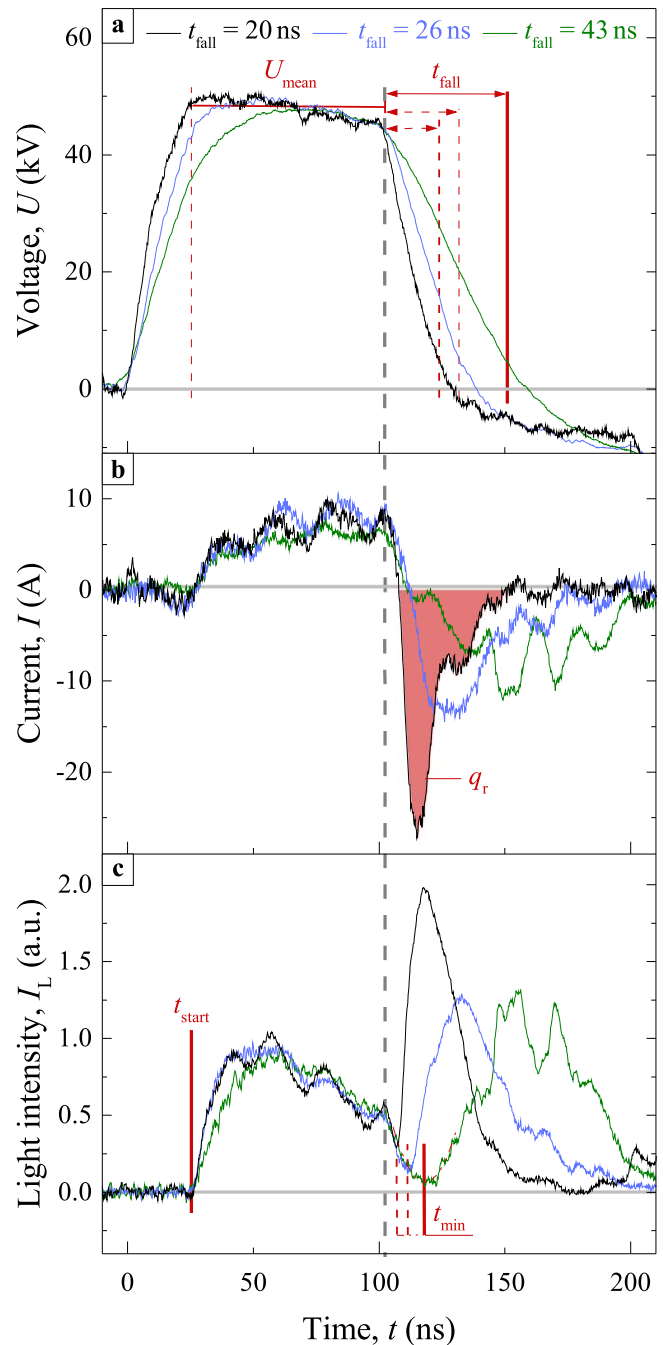


**Figure 4.** Voltages (a), discharge currents (b) and light intensities (c) for individual discharges and different pulse fall times of 20 ns (black lines), 26 ns (blue lines) and 43 ns (green lines). Characteristic times, besides fall times,  $t_{\text{fall}}$ , are time points for the initiation of a discharge event,  $t_{\text{start}}$ , and the time for the observation of a minimum in the light emission,  $t_{\text{min}}$ . The charge,  $q_r$ , flowing back into the discharge channels after it had tentatively been extinguished could be derived from the current measurements.

the electrical connections from the pulse forming lines. The oscillation period can be calculated with approximately 29 ns, which represents the experimental findings of 24 ns rather well.

Shorter fall times resulted in more pronounced and deeper current minima. Conversely, the minima were shallower,

with currents returning back to zero more gradually and over a longer time, for longer fall times.

A typical measurement for the light intensity,  $I_L$ , is shown in figure 4(c). The development of intensities is strongly associated with the development of respective voltages and currents. Light was observed as soon as currents were increasing, indicating the initiation of a discharge event at  $t_{\text{start}}$ . An increase in intensity continued for about 20 ns and proceeded only gradually slower for the longest rise time. After the voltage had reached the designated mean amplitude, light intensities at first followed the development of voltage and current, i.e. with a slow average decrease and with similar oscillations, which were both rather independent from specific rise times. Starting at  $t_{\text{fall}}$ , the light emission became weaker and intensities fell to a minimum at  $t_{\text{min}}$ . At the same time, discharge currents were transitioning through zero, i.e. there was momentarily no current flowing. Logically,  $t_{\text{min}}$  was found significantly later during the discharge development for longer fall times. Passing the intensity minimum, discharges became much brighter again with intensities twice as strong as during the preceding discharge stage for a fall time of 20 ns and still much stronger signals were also observed for fall times of 26 and 43 ns.

Intensity maxima and their relative magnitudes were directly correlated with those recorded for the currents. The strong increase in light emission is the actual phenomenon described as 'reillumination'. The respective overall highest values for emission intensities are achieved later after  $t_{\text{min}}$  for longer fall times. Associated with the higher maxima for shorter fall times was also a shorter time until the discharges were eventually completely extinguished.

### 3.3. Energy dissipated in discharge development

The energy that was dissipated during a discharge was calculated from voltage and current measurements. Contributions for propagation energies,  $E_{\text{prop}}$ , and reillumination energies,  $E_{\text{rel}}$ , were derived separately for the propagation phase and the reillumination phase, respectively. The start of the propagation phase was defined by  $t_{\text{start}}$  (see figure 4(b)) and the beginning of the reillumination phase by  $t_{\text{min}}$  (see figure 4(c)). At this time the polarity of the current reversed, indicating a backflow of charges.

There was no explicit relation between different fall times and individual propagation and reillumination energies. However, a linear dependency between the energy dissipated during the reillumination and propagation was observed, while  $E_{\text{prop}}$  was always higher than  $E_{\text{rel}}$ ; decreasing fall times caused the proportionality constant to increase as shown in figure 5.

Accordingly, reillumination energies increased linearly with higher propagation energies, with slopes of  $(0.21 \pm 0.01)$ ,  $(0.15 \pm 0.01)$  and  $(0.10 \pm 0.01)$  for fall times of 20 ns, 26 ns and 43 ns, respectively. Notably, no distinct dependency between the energies and voltage amplitudes were observed.

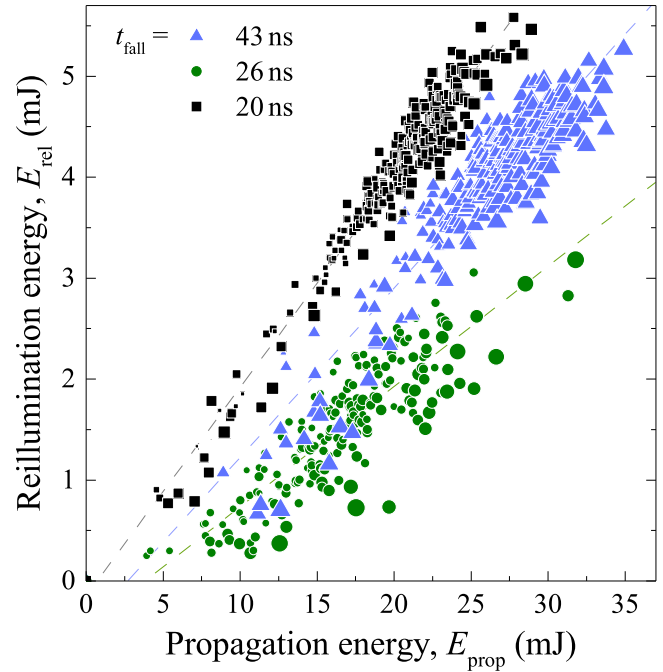


**Figure 5.** Reillumination energies,  $E_{\text{rel}}$ , with respect to propagation energies,  $E_{\text{prop}}$ , i.e. for the preceding expansion of a discharge, for different fall times of 20 ns (black symbols), 26 ns (blue symbols) and 43 ns (green symbols). The size of each symbol represents the respective mean voltage amplitude,  $U_{\text{mean}}$ , i.e. higher amplitudes correspond to larger symbols, which range between 38 and 49 kV. The ratio  $E_{\text{prop}}/E_{\text{rel}}$  increases with increasing fall time, as illustrated by linear fits (dashed lines).

### 3.4. Charge transfer

The reillumination of discharges was directly related to a transfer of charge,  $q_r$ , as already described in previous sections. The respective value can be calculated from the integration of discharge currents,  $I(t)$ , between  $t_{\text{min}}$  and  $t_{\text{end}}$ , the latter defining the time when the currents had expired, i.e.  $I(t_{\text{end}}) = 0$ , as indicated in figure 4(b).

The calculated charge,  $q_r$ , could be associated with the streamer length,  $L_s$ , i.e. the maximum radial expansion of a discharge. The relation is shown for the shortest investigated fall time of 20 ns in figure 6. The streamer length,  $L_s$ , was calculated from the propagation time,  $\Delta t = t_{\text{min}} - t_{\text{start}}$ , and the constant propagation velocity of  $29 \text{ km s}^{-1}$  (see section 3.1). Discharges starting later during the application of an high-voltage pulse had obviously less time to develop and are smaller. The starting point,  $t_{\text{start}}$ , was generally later and more erratic for lower pulse amplitudes. As a consequence, values for streamer lengths were more scattered especially for lower pulse amplitudes. Therefore, all 300 experiments, which are displayed in figure 6, were sorted with respect to the applied voltage,  $U_{\text{mean}}$ , for a more meaningful analysis. Particular groups were defined for  $U_{\text{mean}} < 44 \text{ kV}$ ,  $44 \text{ kV} < U_{\text{mean}} < 48 \text{ kV}$  and  $U_{\text{mean}} > 48 \text{ kV}$ . Especially, charges that were calculated for the last group were clearly linearly dependent on streamer length,  $L_s$ , while values of a single experiment of the first group could be up to 60% lower than the highest determined charge for the same streamer

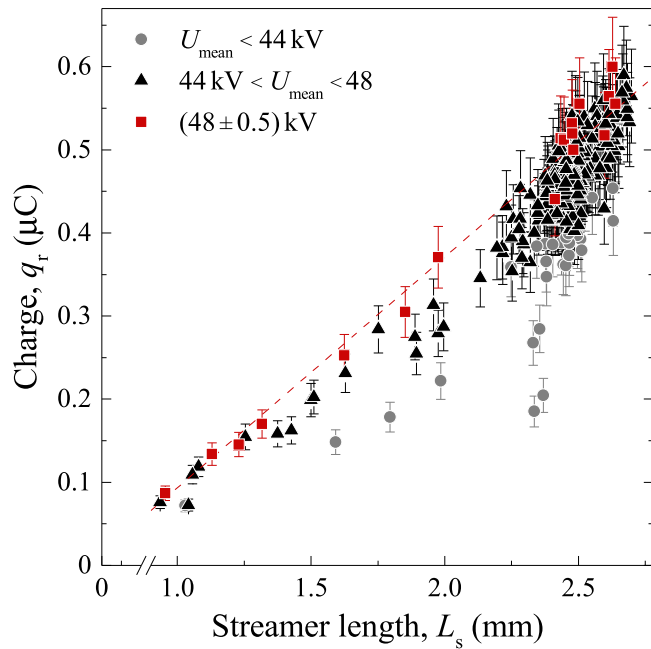


**Figure 6.** Charge backflow,  $q_r$ , into the filaments during the trailing edge of applied voltage pulses depending on the spatial expansion,  $L_s$ , of discharges with respect to pulse amplitudes, as described by  $U_{\text{mean}}$ . Each data point represents a single discharge event. A linear dependency can be assumed for the highest amplitudes (dashed red line) while for lower amplitudes a stronger variation of results and a deviation from this proportionality was observed that is likely reflecting the more erratic initiation of discharges.

length. Accordingly, the linear dependency was indicated in figure 6 only for the group representing the highest pulse amplitudes.

As shown in figure 5, more energy was dissipated during the reillumination phase for shorter fall times with corresponding more pronounced light intensities. Interestingly, the associated backflow of charge,  $q_r$ , did not depend on different fall times and was instead linearly depended on the streamer length,  $L_s$ , as shown in figure 7. Concurrent with results on dissipated energies, the findings indicate that for the given pulse duration of 100 ns, the energy dissipated in the propagation phase determined the energy in the reillumination phase (see figure 5). Conversely, the fall time defined how fast the charge backflow occurred.

### 3.5. Morphology of discharge reillumination

No significant differences were observed for the propagation phase of the discharges with respect to different rise and fall times, especially also for the electrical characteristics and streamer length as presented in sections 3.2 and 3.4, respectively. On the contrary, the measurements for voltages, currents and light intensities suggested considerable fall-time-dependent differences for the development of discharges during the reillumination phase. Three typical individual discharges are presented in figure 8 for different fall times,  $t_{\text{fall}}$ , together with the corresponding voltages and associated recorded light intensities. The pulse amplitude,  $U_{\text{mean}}$ , was in all cases 47 kV. The ICCD gate width was set to 3 ns and time

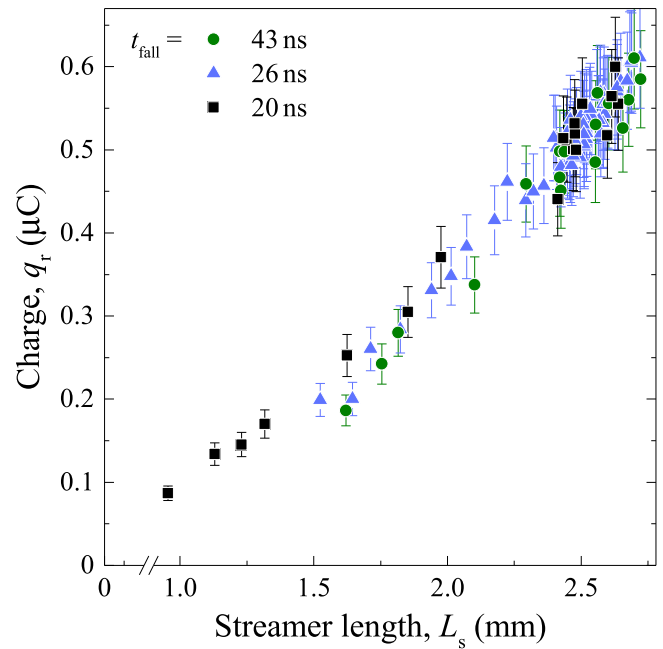


**Figure 7.** Charge transfer,  $q_r$ , during the reillumination phase for fall times of 20 ns (black symbols), 26 ns (blue symbols) and 43 ns (green symbols) depending on the spatial expansion,  $L_s$ , of discharges. The measured charges were nearly directly proportional to the streamer length but independent from fall times.

points for the images were chosen to cover the respective trailing edges and, hence, the entire development of the reillumination phase.

The first column in figure 8 shows the results for a fall time of 20 ns, the middle column for 26 ns and the last column for 43 ns. The first image was always taken when the voltage began to decline, at or close to the intensity minimum at  $t_{\text{min}}$  (row b). The emitted light intensities reached minima at 106, 110 and 120 ns, according to the strong dependence on an increasing fall time. The second image was taken with respect to the maximum in light intensity and the last image shortly before  $t_{\text{fall}}$ , i.e. before the discharge expired and the voltage ceased.

In figure 8 (row c), the images of the discharges exhibited similar branched structures and pronounced filaments towards the end of the propagation phase, i.e. when the voltage amplitude started to decrease, independent of a specific fall time. However, the filaments had faded to a different extent, which is in agreement with the spatial-integrated measurements of the emitted light.

Images, acquired during the falling edge of the voltage that were taken after the transition through the respective minima in light intensity, generally showed much higher intensities close to the needle tip (see figure 8 (row d)). Their values were similar to intensities that were found for the ignition of the plasma only in the immediate vicinity of the tip, but for this stage light was spread across a much larger volume. Notably, filaments that were alight are found at the same location as channels created during the propagation phase but were now much brighter. How many of the channels that were originating from the tip and remaining from the

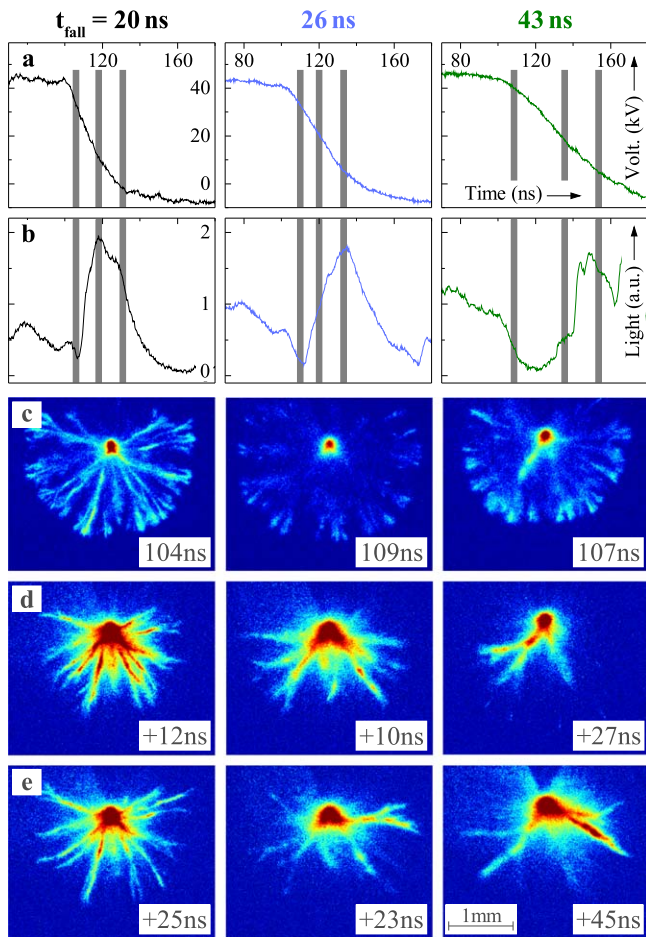


**Figure 8.** Typical framing camera images of discharges induced by voltage pulses with different fall times. Voltages (row a) and light intensities (row b) were synchronized with the images (row c–e) that were taken at three different time points (indicated by gray bars).

propagation phase were illuminated again depend on fall time. For a fall time of 20 ns all filaments were brightly reignited. Conversely, for a fall time of 43 ns only two prominent filaments could still be determined. Only the reillumination of pre-existing channels was found and no newly generated filaments were observed.

Images that were taken close to the end of  $t_{\text{fall}}$  showed that reignited channels had reached the spatial extend of the filaments that remained from the propagation phase (see figure 8 (row e)).

For a closer look, the development of the reillumination phase was recorded between  $t_{\text{min}}$ , just at the end of the propagation phase, and the time of maximal light emission of the spatially integrated intensity. For comparison, another sequence of images was acquired for the shortest and longest fall times, i.e.  $t_{\text{fall}} = 20$  and 43 ns. Recording times of the framing camera were chosen in a way, so that the next ICCD gate started, when the preceding camera had finished acquiring an image. With a gate width of 3 ns, this way the entire observation period extended over 9 ns. Timing information, relative to the voltage pulse and the development of light intensity are shown in the upper panel of figure 9 for a fall time of 20 ns and examples of associated images are

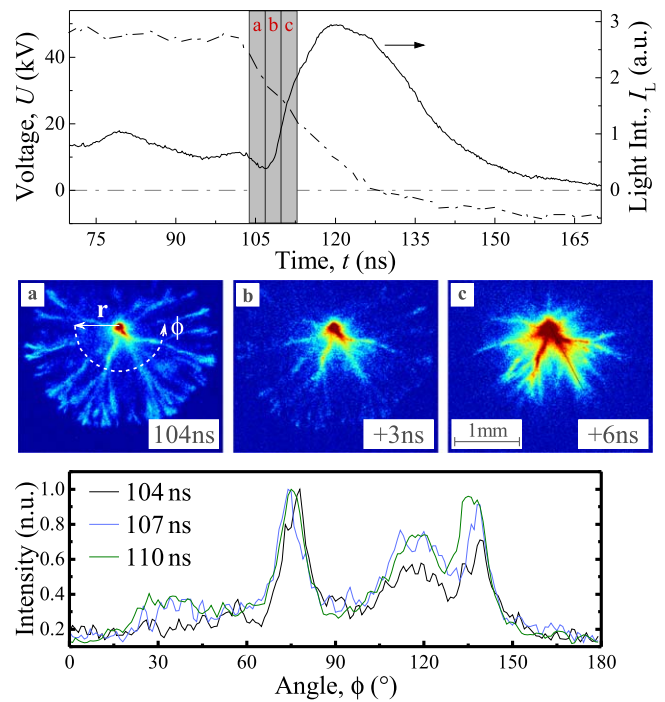


**Figure 9.** Detailed image analysis of the onset of the discharge reillumination for a fall time of 20 ns. For altogether 9 ns, three individual consecutive images were recorded. Respective measurement for voltage and light intensity are presented together with the acquired images (a)–(c), according to the timing information (gray bars) shown in the upper panel. The images describe the discharge at the end of its propagation (a), the reignition of filaments starting from the needle tip (b) and, eventually, the propagating reillumination (c). The angular intensity profiles (lower panel) were derived for a semi-circle with a radius of 0.7 mm around the needle tip and confirmed the reillumination of all pre-existing channels by the similarity of all measurements.

presented in the row in the middle of this figure. The lower panel shows the angular intensity profiles that were derived from the images along a semi-circle for a fixed radial distance from the needle tip.

The first image (a) of the sequence was taken just before  $t_{\text{min}}$  and shows the filamentary structure as well as the largest extend of the discharge that was reached during the preceding propagation phase. After passing the light intensity minimum, the next image (b) reveals an increased intensity at the center of the discharge, with light spreading out into the previous formed channels that had become almost unnoticeable beyond. This confirms that the reillumination phase started propagating from the needle tip at time  $t_{\text{min}}$ .

The last image in the sequence describes the ongoing further expansion of the reillumination. Eventually, all of the channels that were laid out during the propagation phase are reignited to their previous expansion. This was associated with the maximum that was observed for the spatially integrated light intensity. Accordingly, all channels remaining from the propagation phase were reilluminated within 6 ns after  $t_{\text{min}}$  corresponding to a mean propagation velocity of approximately  $200 \text{ km s}^{-1}$ .

The reillumination of all pre-existing channels is explicitly proven by the angular intensity profiles that were derived



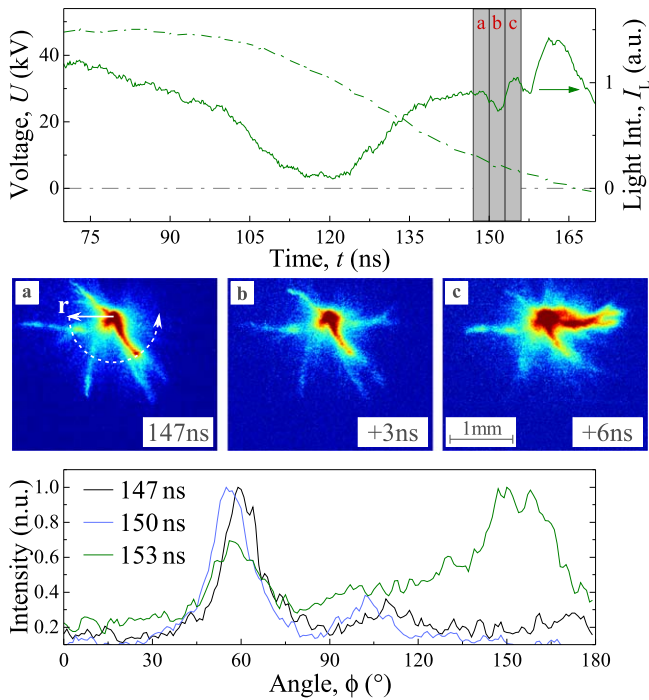


**Figure 10.** Detailed image analysis of the onset of the discharge reillumination during the trailing edge of a voltage pulse with a fall time of 43 ns. For altogether 9 ns, three individual consecutive images were recorded, each with a 3 ns gate width. Respective measurements for voltage and light intensities are presented together with the acquired images (a)–(c), according to the timing information (gray bars) shown in the upper panel. The images describe the previously reignited channels (a). Within 6 ns a channel that was not visible in the first image was reilluminated (b), (c). This is also confirmed by the angular intensity profiles, which are shown for a radius of 0.7 mm in the lower panel. The profiles are similar for the first two images whereas the profile for the last image points out the emerging channel.

for a fixed radius of  $r = 0.7$  mm from the needle tip (figure 9, lower panel). For the different time points, the normalized profiles nearly overlapped and showed light emitted from the same location along the semi-circle. In particular, three peaks that corresponded to the brightest filaments are visible.

A slightly different behavior was also observed for the longest fall time of 43 ns and is presented in figure 10. In this case an image-sequence was recorded for longer times after  $t_{\min}$ , taking into account the extended development towards the intensity maximum. Some channels were already reignited in the first image (a), since the image was acquired 30 ns after  $t_{\min}$  and the spatially integrated light intensity had already increased. However, the second image (b) shows the emergence of a new channel that became much more pronounced and much brighter than the other filaments, which almost vanished in the third image (c). This development is even more convincingly revealed by the respective normalized angular intensity profiles. At  $60^\circ$ , a prominent channel is observed for images taken at 147 and 153 ns. During the following 3 ns, the intensity of this filament decreased while simultaneously another strong channel emerged in a direction between  $140^\circ$  and  $170^\circ$ . The associated spatial integrated emission intensity peaked at about the same time at 160 ns,

indicating that at this time the discharge was in fact dominated by this particular filament and, hence, was probably carrying most of the associated discharge current. This characteristic was also observed for other discharges that were investigated for a fall time of 43 ns. Additionally, the appearance of several intensity peaks indicated again that all previously channels were reignited eventually. The collapse of the discharge consecutively into single filaments therefore seems to be a general feature for the application of high-voltage pulses with longer fall times.

## 4. Discussion

The development and propagation of filamentary discharges, i.e. streamers, in gases and in liquids at atmospheric pressure show besides some similarities distinctively different characteristics. Individual filaments propagate with velocities in the order of  $1000 \text{ km s}^{-1}$  for gaseous corona discharges. In laboratory experiments, individual channels often reach lengths of about 10 cm, diameters of  $100 \mu\text{m}$  and electron densities of  $10^{14} \text{ cm}^{-3}$  [13, 14]. Usually, several filaments originate from the high-voltage electrode, although not necessarily simultaneously, and branch out. In comparison, corona-like discharges in water grow slower (with about  $30 \text{ km s}^{-1}$ ) due to the three orders of magnitude higher density of the medium, are shorter (on the order of 1 cm) and generally thinner (about  $10 \mu\text{m}$  in diameter) for applied voltages that are comparable to the instigation-voltages of discharges in gases [11, 15, 16]. The electron density can exceed  $10^{19} \text{ cm}^{-3}$  and all channels ignite simultaneously from the same point [8, 17]. In addition, unique features, such as reillumination, have only been observed for corona-like discharges in water but not for gaseous discharges, at least not at atmospheric pressure. Regardless, the propagation mechanism is assumed to be similar for liquids and gases [15]. Therefore, respective models can be used for an explanation of reillumination and other characteristics by taking into account the particular properties of the liquid medium.

Accordingly, a simplified single streamer model of underwater discharge propagation was derived (section 4.1) and applied towards an account on the measurements of transferred charge (section 4.2) as well as the development of light emission during the reillumination phase (section 4.3).

### 4.1. Propagation of discharge filaments with respect to an external electric field

Recently, it was shown by Qin *et al* that the propagation of streamers in gases and liquids is not only depending on the localized electric field enhancement at the streamer head, but on the external electric field,  $E_{\text{ex}}$ , itself [18]. Accordingly, they derived an analytic expression for the relation between streamer head radius,  $R_s$ , and external electric field,  $E_{\text{ex}}$ , based on energy conservation and the description of a streamer as thin spherical charge layer. In conclusion, the head radius is inversely proportional to the external electric field according

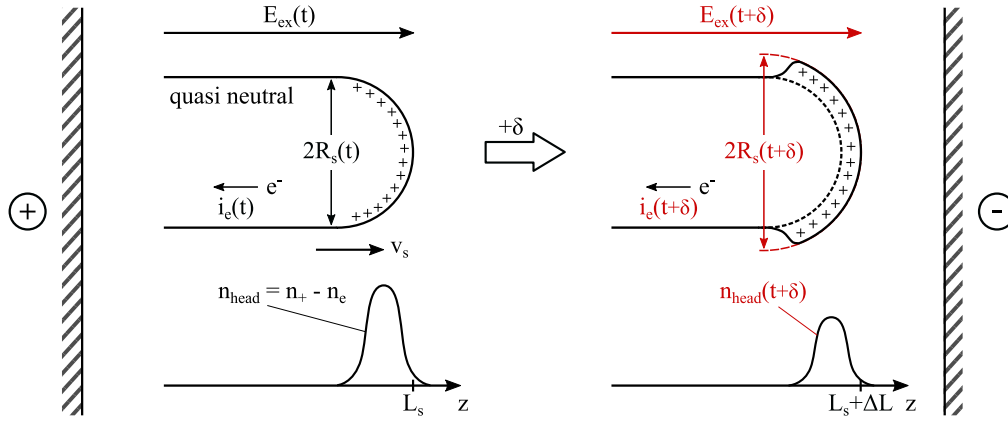


**Figure 11.** Illustration of streamer propagation. A quasi-neutral channel of radius,  $R_s$ , with a head charge corresponding to a charge density,  $n_{\text{head}}$ , extends with a velocity,  $v_s$ . The strength of the external applied electric field,  $E_{\text{ex}}$ , decreases at the streamer head during a time step,  $\delta$ . As a result, the streamer radius grows, resulting in smaller values for  $n_{\text{head}}$ .

to the following equation:

$$R_s \propto \frac{1}{E_{\text{ex}}}. \quad (1)$$

For a gaseous media, the authors demonstrated the validity of this equation by a plasma fluid model, but pointed out that the relation is also valid for dielectric liquids, such as deionized water, for discharges developing on submicrosecond time scales. With a dielectric time constant  $\varepsilon/\sigma$  (for permittivity,  $\varepsilon$ , and conductivity,  $\sigma$ , of the respective medium) of  $7 \mu\text{s}$  for deionized water, is the development of discharges for a high-voltage pulse of 100 ns well within the range of the constraints of the analysis.

No further assumptions on specific ionization processes, densities of the medium or plasma chemistries are made. The development of corona-like discharges (in gases or liquids) is illustrated together with all relevant quantities in figure 11. A streamer channel propagates with head radius,  $R_s$ , and a constant velocity,  $v_s$ , away from the electrode, i.e. the needle tip, which is biased with a positive voltage,  $U_{\text{needle}}$ . Once initiated, the external electric field,  $E_{\text{ex}}$ , sustains the propagation. The potential at the head of the streamer,  $U_{\text{head}}$ , is assumed to be equal to the voltage applied to the needle,  $U_{\text{needle}}$  due to the highly conductive discharge-channel of length  $L_s$ . The head propagates further, according to the classic description, by ionizing the medium in front. The consequence is a positive head charge density,  $n_{\text{head}}$ , since electrons are transferred much faster than ions back through the channel, constituting a current  $i_e$  [12].

An infinitesimal time step,  $\delta$ , later, the external electric field has changed. Without loss of generality,  $E_{\text{ex}}$  is assumed to decrease (in this example) while the streamer has propagated by  $\Delta L = v_s \delta$ . As a result of equation (1), the streamer radius is increasing and the head charge density is diminishing. The head charge,  $q$ , accumulating at the end of an ideally conducting filament can be expressed according to Loeb by equation (2) for the associated potential at the head,  $U_{\text{head}} = U_{\text{needle}}$ , and the streamer radius,  $R_s$  [19].

$$q = 4\pi\varepsilon_0 U_{\text{head}} R_s. \quad (2)$$

The electric field,  $E_{\text{ex}}$ , in direction of the needle can be approximated for the needle-to-plate geometry on the axis of direct connection between both electrodes by equation (3),

$$E_{\text{ex}} = \frac{2U_{\text{needle}}}{z \ln\left(\frac{4d}{r_n}\right)} \propto \frac{U_{\text{needle}}}{z}, \quad (3)$$

with the tip curvature radius,  $r_n$ , the distance,  $d$ , between the electrodes, and the potential,  $U_{\text{needle}}$ , applied to the needle.

By introducing a proportionality constant,  $a_E$ , the streamer radius  $R_s$ , can hence be derived according to equation (4):

$$R_s = \frac{a_E \ln\left(\frac{4d}{r_n}\right)}{2} \cdot \frac{z}{U_{\text{needle}}}. \quad (4)$$

This way, the streamer head charge,  $q$ , can then be related to the actual position of the streamer head,  $z$ , as described by equation (5). All parameters accounting for the electrode geometry, the ratio of applied voltage,  $U_{\text{needle}}$ , to head potential,  $U_{\text{head}}$ , and other quantities can be summarized in a proportionality factor,  $b$ , to explicitly express the correlation with the streamer head position.

$$q = 2\pi\varepsilon_0 \cdot a_E \ln\left(\frac{4d}{r_n}\right) \cdot \frac{U_{\text{head}}}{U_{\text{needle}}} \cdot z = b \cdot z, \quad (5)$$

Corollary, the charge accumulated in the streamer heads at the end of a streamer propagation is linear dependent on the total streamer length,  $L_s$  and independent on the applied needle potential, as long as the streamer channel is ideally conductive.

The analytical model, in particular equation (5), does not describe the branching of filaments. A simple and general assessment of the overall branching characteristics and discharge structure can be obtained assuming the total charge of a branching streamer to be conserved during the branching process [13]. In agreement with the observation, it is further assumed that the discharge originates from a single point [8, 17, 20]. Based on these reasonable assumptions, the filamentary structure of corona-like discharges can be described by a network of impedances,  $Z_i$ , representing individual channels, and capacities,  $C_i$ , for each streamer head. Since,

the channels are assumed to be ideal conductors, the channel impedances equal zero for every branch. Hence, the electric network defaults to a circuit of parallel capacitors with an equivalent total capacitance,  $C$ , described by

$$C = \sum_i C_i. \quad (6)$$

The capacitance,  $C_i$ , of a single streamer head can be calculated, again according to Loeb, from the particular head radius,  $R_{s,i}$ , from equation (7) [19]

$$C_i = 4\pi\epsilon_0 R_{s,i}. \quad (7)$$

Accordingly, the total capacitance,  $C$ , can be expressed by

$$C = 4\pi\epsilon_0 \sum_i R_{s,i} = 4\pi\epsilon_0 R_s. \quad (8)$$

As a result, the entire discharge structure can in fact be interpreted as only a single filament with radius  $R_s = \sum R_{s,i}$  and head charge  $Q = \sum q_i$ . The respective values offer an upper limit for the total charge along the discharge perimeter depending on the extent of the discharge, i.e. the streamer length  $L_s$  (see equation (5)).

#### 4.2. Relation between streamer length and transferred charge

The charge that is transferred into the channels after the voltage decreases and, in a first approximation, the positive space charges that had formed at the streamer heads until the end of the propagation phase are essentially the same. The total head charge,  $Q$ , according to the model presented in the preceding section, is therefore directly correlated with the charge,  $q_r$ , that was determined from current measurements (as described in section 3.4). According to equation (5),  $q_r$  should in particular be proportional to the streamer length,  $L_s$ , which determines the distance that filaments had on average extended. The respective measurements, shown in figure 6, indeed confirm the linear dependency between  $L_s$  and  $q_r$ , as predicted by the model. Conversely, the proportionality factor,  $b$ , which describes the relation according to equation (5), can be determined as  $(0.278 \pm 0.007) \mu\text{C mm}^{-1}$ .

Implicitly included in  $b$  is the ratio of voltage at the channel head to the voltage at the needle,  $U_{\text{head}}/U_{\text{needle}}$ , which defaults to unity for ideally conductive discharge channels. Accordingly, measured charges,  $q_r$ , should be independent from these parameters and, hence, especially the applied voltage,  $U_{\text{mean}}$  (as long as this one is sufficient to instigate a discharge at all). That this assumption is valid for the investigated discharges is demonstrated by the strict linearity of most data points in figure 6.

The straight line, approximating the transferred charge, does, however, not include the origin as predicted by equation (5), i.e. does not describe the absence of charges while no streamer has yet emerged correctly. The reason for the slight discrepancy is most likely due to the ions that constitute the head space charge, which could already have partially recombined before and during the reillumination. This would correspond to lower values for the transferred charge. Furthermore, the uncertainty inherent to the measurement of transferred charges and streamer lengths could

increase the discrepancy. Both parameters depend on time points,  $t_{\text{start}}$  and  $t_{\text{min}}$ , which can only be determined within certain limits of 3–5 ns from the light intensities, especially for small values.

However, measured charges are also slightly lower than predicted by the linear relationship described by equation (5) for lower applied voltages. Charges are especially 60% smaller than expected for the lowest applied voltage. This might indicate that filaments had actually not become highly conductive for these conditions. Fully developed and highly conductive channels develop more likely when initiated early during the application of a voltage pulse with higher amplitude. This is exactly what the respective measurements seem to describe. Conversely, the analysis offers a possibility to study channel conductivities by backtracking the derivation of equation (5).

#### 4.3. Mechanism of channel reillumination for different fall times

Qin and Pasko suggested that a streamer propagates as long as the external electric field is high enough to support ionization processes at the streamer head [18]. As the external field strength declines, the head radius starts to increase and, eventually, the streamer stops propagating. This corresponds to a minimum in the light intensity at the time  $t_{\text{min}}$ . However, the actual expiration of the discharge happens not as abrupt as it might be suggested by such a parameter and develops more gradually as demonstrated by the measurements shown in figure 4. When the voltage starts to fall, the discharge current decreases together with the light intensity. At  $t_{\text{min}}$  there is no longer any discharge current. This process takes longer and is associated with later times,  $t_{\text{min}}$ , for longer fall times,  $t_{\text{fall}}$ , since even the diminishing external electric field is able to still sustain some ionization processes.

After passing through the minimum at  $t_{\text{min}}$ , the space charge remaining at the end of each channel is then able to accelerate electrons along the channel towards the streamer head. Hence, the current reverses polarity (see figure 4). As illustrated by the images that are shown in figures 8–10, the electrons gain enough energy to reignite the channels laid out during the propagation phase.

Reillumination starts accordingly from the needle tip and electron impact ionization processes enhance the electron density again. As a result, a reillumination front propagates with the electron avalanche towards the end of the filaments with a velocity that is actually higher than that observed for the propagation phase (see section 4.1). Of crucial importance for this process is apparently the particle density in the residual filaments and the residual head charge density. When it takes longer for reignition to start, as defined by  $t_{\text{min}}$  and  $t_{\text{fall}}$ , the latter is most likely diminished, resulting in a lower electric field in the channel and, therefore, in a weaker electron avalanche. This could explain the lower energy dissipation during the reillumination phase as it is presented in figure 5.

With the drop of the applied voltage to zero, recorded spatially integrated light intensities reach peak values with maximum values that are depending on fall time. Eventually,

the electric field that has built up in the channels decreases due to the charge influx at the streamer heads. Hence, the light intensities faint together with the current. The respective development is shown in figure 4.

The charge transferred during the reillumination is not depending on the fall times. This suggests that initial space charges at the streamer heads are similar after the propagation phase for all investigated fall times,  $t_{\text{fall}}$ . The respective discharge characteristics are up to this time only determined by pulse length and applied voltage, which were in all cases similar. This is demonstrated in particular by the images presented in figure 2 and expressed especially by comparable streamer lengths,  $L_s$ . As it was found from the measurements of the charge transferred to discharge filaments during the reillumination phase (see figure 7) and confirmed by the presented model (see equation (5)), a similar amount of charge has to be transferred into the channels to neutralize the head space charges independent on the fall time; although on different time scales.

The description does, so far, not take into account the branching of streamers and is instead based on the propagation of a single filament from start to end, which is motivated in particular by the model and equation (6) ff. However, the description of the propagation by only a single streamer seems at a close look only applicable for the reilluminated structures that are observed for the shortest fall time, i.e. with every channel reignited (see figure 8). There is no consistent theory of branching processes for discharges in water. A possibility suggested by Joshi *et al* is the splitting of filaments when they hit on density fluctuations in the medium, e.g. on bubbles of dissolved gas that could have a size of only a few nanometers [21]. Regardless of actual branching criteria or mechanisms, a reasonable assumption for the discharge development is still the conservation of the total charge during the channel branching. The assessment is based on similar characteristics that were established for corona discharges in gases, even for a non-uniform distribution of charges into each channel head [13, 14]. Therefore, during branching the overall conserved charge,  $Q$ , can also for discharges in water be assumed to be distributed into smaller and different individual charges,  $q_i$ , which form the new channel heads.

Conversely, highly localized conditions at the streamer head seem to determine if and when a particular channel is reignited, depending on different fall times,  $t_{\text{fall}}$ , and respective head charges,  $q_i$ . The head charges are proportional to individual channel radii,  $R_{s,i}$ , and the applied potential,  $U_{\text{needle}}$ , during the propagation phase (see section 4.1). An increase of  $q_i$  results in an amplification of the local electric field at the streamer head. For the reillumination phase, the fall time determines the time when the electric field in a channel becomes strong enough to reignite a filament. Therefore, reaching this threshold for the electric field determines the sequence of channel reillumination and  $t_{\text{fall}}$  specifies how fast the sequence reignites. It is most likely that the distribution of head charges is independent from fall times, since discharge morphologies in general appear unaffected by them (see figure 2). The distribution of head charges is also not affecting the reillumination pathways at all for the

shortest investigated fall time and all channels reignite approximately at the same time. Longer fall times result in measurable time differences for the reillumination of single channels. Eventually, this leads to the reillumination of only a single main channel at a time as it is observed for the longest investigated fall time of 43 ns (see figure 10).

## 5. Conclusions

The electrical characterization of individual discharges in water, together with consecutive images of the discharge development, revealed characteristics for the reignition of discharge channels that are strongly dependent on the fall time of the applied voltage pulse.

All filaments that had formed during the application of the voltage pulse were reilluminated at the same time for short fall times, while channels reignited rather sequentially with increasing fall times. Only a single filament at a time frequently dominated the reillumination eventually for the longest fall time. Associated with an increase in fall time was an extended emission of light and longer lasting currents. However, the charge, transferred during this reillumination, which was derived from the current, was found to be independent from fall times. Hence, this charge seems to be determined by the propagation phase, which ended with similar distributions of filaments and especially also the same semi-spherical expansion.

Reignition mechanisms can be explained with respect to the decline of the external electric field, which vice versa determines channel radius and associated charge distributions at the head. This derivation is independent from the number of individual filaments and their distribution, i.e. the specific distribution of the charge accumulated by the end of the propagation phase. Therefore, a model for single, unbranched, ideally conductive streamer can also describe reignition.

Filaments did not suffer much decay and maintained adequate conditions for reignition for a shorter fall time. Differences of head charge densities could apparently resulted in a noticeable delay in reignition of individual discharge channels for longer fall times.

The similar structure and propagation of corona-like discharges in water and in gases and the possibility to describe both by similar approaches suggests that there are actual no significant differences for their development in both media once the discharge is established. Therefore, both can be described regardless of the medium as actual corona discharges. However, liquid specific properties, such as a high particle density and conductivity, are likely to affect the discharge behavior. For instance, the particle density in the channels is dependent on the energy dissipated during the propagation, which is associated with the liquid conductivity. Hence, the dependency of channel reignition on water conductivity combined with an investigation of the particle densities inside the channels would be an interesting topic of further study.

The reillumination of individual channels was more sequential for long fall times, so current measurements could




reveal the distribution of charges between different channels and clarify conditions for branching depending on the properties of individual filaments. Changing in addition to fall times also pulse durations and applied voltages would hereby allow to introduce different final charges. Ideally these studies can be complemented by 3D-imaging methods and spectroscopic investigations, providing a better picture of channel and charge distributions as well as temporal and spatial resolved electron densities.

In conclusion, the possibility to study discharge phenomena with respect to fall times offers a new way to investigate discharge structures and channel distributions.

## ORCID iDs

Raphael Rataj  <https://orcid.org/0000-0002-7777-0367>

Hans Höft  <https://orcid.org/0000-0002-9224-4103>

Juergen F Kolb  <https://orcid.org/0000-0002-0434-5001>

## References

- [1] Ignat M, Samoila P, Coromelci C, Sacarescu L, Asaftei I, Harabagiu V and Miron C 2017 *C. R. Chim.* **21** 310
- [2] Banaschik R, Lukes P, Jablonowski H, Hammer M U, Weltmann K-D and Kolb J F 2015 *Water Res.* **84** 127
- [3] Zocher K, Banaschik R, Schulze C, Schulz T, Kredl J, Miron C, Schmidt M, Mundt S, Frey W and Kolb J F 2016 *Plasma Med.* **6** 273
- [4] Joshi R P and Thagard S M 2013 *Plasma Chem. Plasma Process.* **33** 1
- [5] Höft H and Huiskamp T 2018 *Eur. Phys. J. D* **72** 217
- [6] Marinov I, Starikovskaia S and Rousseau A 2014 *J. Phys. D: Appl. Phys.* **47** 224017
- [7] Pongrác B, Šimek M, Člupek M, Babický V and Lukeš P 2018 *J. Phys. D: Appl. Phys.* **51** 124001
- [8] Seepersad Y, Pekker M, Shneider M N, Fridman A and Dobrynin D 2013 *J. Phys. D: Appl. Phys.* **46** 355201
- [9] Marinov I, Guaitella O, Rousseau A and Starikovskaia S M 2013 *J. Phys. D: Appl. Phys.* **46** 464013
- [10] Salazar J N et al 2005 *IEEE Int. Conf. Dielectric Liquids, ICDL 2005*. 2005 p 91
- [11] An W, Baumung K and Bluhm H 2007 *J. Appl. Phys.* **101** 053302
- [12] Lukeš P 2001 *Dissertation* Institute of Plasma Physics AS CR, Prague, Czech Republic
- [13] Briels T M P, Kos J, van Veldhuizen E M and Ebert U 2006 *J. Phys. D: Appl. Phys.* **39** 5201
- [14] Ebert U, Montijn C, Briels T M P, Hundsdorfer W, Meulenbroek B, Rocco A and van Veldhuizen E M 2006 *Plasma Sources Sci. Technol.* **15** S118
- [15] Bruggeman P and Leys C 2009 *J. Phys. D: Appl. Phys.* **42** 28
- [16] Kolb J F, Joshi R P, Xiao S and Schoenbach K H 2008 *J. Phys. D: Appl. Phys.* **41** 234007
- [17] Fujita H, Kanazawa S, Ohtani K, Komiya A, Kaneko T and Sato T 2014 *J. Appl. Phys.* **116** 213301
- [18] Qin J and Pasko V P 2014 *J. Phys. D: Appl. Phys.* **47** 435202
- [19] Loeb L B 1965 *Science* **148** 17
- [20] Dobrynin D, Seepersad Y, Pekker M, Shneider M, Friedman G and Fridman A 2013 *J. Phys. D: Appl. Phys.* **46** 105201
- [21] Qian J, Joshi R P, Schoenbach K H, Woodworth J R and Sarkisov G S 2006 *IEEE Trans. Plasma Sci.* **34** 1680



## Article 2

### Authors

Raphael Rataj  
Matthias Werneburg  
Harald Below  
Jürgen F. Kolb

### Title

Hydrogen peroxide production of underwater nanosecond-pulsed streamer discharges with respect to pulse parameters and associated discharge characteristics

### Journal

Plasma Sources Science and Technology, Volume 31, Number 10

Online: <https://iopscience.iop.org/article/10.1088/1361-6595/ac942a/meta>

DOI: <https://doi.org/10.1088/1361-6595/ac942a>

Reprinted with kind permission from:

Plasma Sources Sci. Technol. 28.12, 2019,

Copyright by IOP Publishing Limited. ©IOP Publishing. Reproduced with permission.

All rights reserved.





# Hydrogen peroxide production of underwater nanosecond-pulsed streamer discharges with respect to pulse parameters and associated discharge characteristics

Raphael Rataj<sup>1,2</sup> , Matthias Werneburg<sup>1,3</sup>, Harald Below<sup>4</sup> and Juergen F Kolb<sup>1,2,\*</sup> 

<sup>1</sup> Leibniz Institute for Plasma Science and Technology (INP), Felix-Hausdorff-Str. 2, 17489 Greifswald, Germany

<sup>2</sup> University of Rostock, Institute of Physics, Albert-Einstein-Str. 23-24, 18059 Rostock, Germany

<sup>3</sup> University of Greifswald, Institute of Physics, Felix-Hausdorff-Str. 6, 17489 Greifswald, Germany

<sup>4</sup> Department of Restorative Dentistry, Periodontology, Endodontology, Preventive and Pediatric Dentistry, Dental School of University Medicine Greifswald, Walter-Rathenau-Straße 42, 17489, Greifswald, Germany

E-mail: [raphael.rataj@inp-greifswald.de](mailto:raphael.rataj@inp-greifswald.de) and [juergen.kolb@inp-greifswald.de](mailto:juergen.kolb@inp-greifswald.de)

Received 1 June 2022, revised 15 August 2022

Accepted for publication 22 September 2022

Published 14 October 2022



CrossMark

## Abstract

Pulsed streamer discharges submerged in water have demonstrated potential in a number of applications. Especially the generation of discharges by short high-voltage pulses in the nanosecond range has been found to offer advantages with respect to efficacies and efficiencies. The exploited plasma chemistry generally relies on the initial production of short-lived species, e.g. hydroxyl radicals. Since the diagnostic of these transient species is not readily possible, a quantification of hydrogen peroxide provides an adequate assessment of underlying reactions. These conceivably depend on the characteristics of the high-voltage pulses, such as pulse duration, pulse amplitude, as well as pulse steepness.

A novel electrochemical flow-injection system was used to relate these parameters to hydrogen peroxide concentrations. Accordingly, the accumulated hydrogen peroxide production for streamer discharges ignited in deionized water was investigated for pulse durations of 100 ns and 300 ns, pulse amplitudes between 54 kV and 64 kV, and pulse rise times from 16 ns to 31 ns. An independent control of the individual pulse parameters was enabled by providing the high-voltage pulses with a Blumlein line. Applied voltage, discharge current, optical light emission and time-integrated images were recorded for each individual discharge to determine dissipated energy, inception statistic, discharge expansion and the lifetime of a discharge. Pulse steepness did not affect the hydrogen peroxide production rate, but an increase in amplitude of 10 kV for 100 ns pulses nearly doubled the rate to  $(0.19 \pm 0.01) \text{ mol l}^{-1} \text{ s}^{-1}$ , which was overall the highest determined rate. The energy efficiency did not change with pulse

\* Author to whom any correspondence should be addressed.



Original content from this work may be used under the terms of the [Creative Commons Attribution 4.0 licence](https://creativecommons.org/licenses/by/4.0/). Any further distribution of this work must maintain attribution to the author(s) and the title of the work, journal citation and DOI.

amplitude, but was sensitive to pulse duration. Notably, production rate and efficiency doubled when the pulse duration decreased from 300 ns to 100 ns, resulting in the best peroxide production efficiency of  $(9.2 \pm 0.9) \text{ g kWh}^{-1}$ . The detailed analysis revealed that the hydrogen peroxide production rate could be described by the energy dissipation in a representative single streamer. The production efficiency was affected by the corresponding discharge volume, which was comprised by the collective volume of all filaments. Hence, dissipating more energy in a filament resulted in an increased production rate, while increasing the relative volume of the discharge compared to its propagation time increased the energy efficiency.

Keywords: hydrogen peroxide, nanosecond-pulsed streamer, pulsed power, plasma in liquids, plasma chemistry

 Supplementary material for this article is available [online](#)

(Some figures may appear in colour only in the online journal)

## 1. Introduction

Sub-microsecond pulsed streamer discharges in liquid water, which are generated from the application of high-voltage pulses, have been found an environmentally friendly technology to degrade hazardous pollutants [1–4]. In general, this water purification method exploits the generation of UV-radiation and oxidative chemical species, e.g.  $\cdot\text{O}$ ,  $\cdot\text{OH}$  or  $\cdot\text{OOH}$ . Especially, hydroxyl radicals are known for their high reactivity and, hence, their essential role in the plasma-assisted degradation of recalcitrant organic compounds. However, hydroxyl radicals are short-lived with a lifetime in the order of milliseconds at most [5]. Unless they react with other compounds, i.e. pollutants, the radicals eventually recombine to hydrogen peroxide. Therefore, in particular in pure water, the more stable hydrogen peroxide concentration is an appropriate measure for initially created hydroxyl radicals [6, 7].

Recent publications reported hydrogen peroxide production efficiencies for sub-microsecond pulsed streamer discharges in liquid water of  $(1\text{--}2) \text{ g kWh}^{-1}$ , which is low when accounting for the limitations on treatment costs in common sewage water treatment plants [6–9]. An optimization of electrical operating parameters is an obvious way to improve the efficiency of pulsed power systems. However, this requires a detailed understanding of the influence of pertinent electrical characteristics [8, 10].

Sub-microsecond pulsed streamer discharges in liquid water are typically instigated by rectangular high-voltage pulses, which can be described by direct and derived parameters. Direct parameters, such as amplitude, pulse steepness and pulse duration, define the shape of an individual pulse, while derived parameters, like energy and repetition rate, characterize the pulses in relation to the specific experimental conditions, e.g. implicitly consider pulse reflections due to impedance mismatching or inherently include discharge or residual post-discharge characteristics. Derived parameters, especially energy, have generally been investigated with respect to specifically pursued applications [6–9, 11]. Only

few fundamental studies have considered the effect of selected direct parameters on hydrogen peroxide production [9–23].

For example, increasing pulse amplitudes have been observed to accelerate the production. The finding is commonly explained with an increased power density in a streamer, resulting in higher channel temperatures [9, 11–16]. Concurrent simulations showed that the thermal dissociation of  $\text{H}_2\text{O}$  in the discharge filaments was the dominant pathway for creating hydroxyl radicals [9, 17]. Accordingly, higher temperatures should correspond to higher amounts of hydrogen peroxide. However, a higher pulse amplitude also resulted in an earlier discharge-onset [18–21]. Accordingly, streamer lengths were increasing with an earlier ignition, yielding higher amounts of chemical species even if the channel temperature was not rising [10, 22]. Therefore, species concentrations cannot be understood solely from the direct parameters. In addition, the discharge characteristics (with respect to the properties of the propagation medium, like conductivity), e.g. streamer length, morphology, temperature, time lags, etc. have to be taken into account.

A pertinent example is the effect of pulse duration, which dominantly affects the streamer length and statistical time lag for a given electrode configuration [10, 22]. Associated is an enlarged active discharge volume, which encouraged the production of higher amounts of hydrogen peroxide [10, 11, 16].

Pulse rise times have also been reported crucial for the discharge initiation [23], while fall times have been found to affect post-discharge behavior, i.e. the reillumination of discharge channels [20, 24]. Related effects can consequently be expected on radical reaction chemistry and hydrogen peroxide production.

Although the impact of direct pulse parameters cannot be doubted, comprehensive studies on their individual contribution to the promoted plasma chemistry are so far insufficient. Previous reports have either focused on a specific characteristic, mostly neglecting the relation to other aspects, in particular

of the treated medium, e.g. conductivity, or have fallen short to consider the impact of a specific parameter also on other possibly affected discharge characteristics, e.g. time lags, or lacked the necessary single discharge diagnostic, i.e. electrical and optical methods, to resolve individual effects [9–21].

Necessary experiments are admittedly challenging and often not possible with the pulsed power systems that were utilized. Exemplary, an increase in amplitude is also associated with longer pulse durations and fall times for high-voltage pulses that are obtained from the discharge of a bulk capacitor [25]. Another example is a mismatch of the load, which results in pulse reflections especially for the application of rectangular high-voltage pulses, which can considerably affect radical chemistry [9].

These challenges were resolved for the presented study by a Blumlein line pulse generator. If correctly matched to the load, the system can provide single, rectangular high-voltage pulses, i.e. without reflections (within limits). A careful consideration of the entire electrical circuit further provided the possibility to include elements, e.g. impedance elements, which allowed for an independent adjustment of pulse duration, pulse amplitudes as well as rise and fall times [24]. The applied and investigated high-voltage pulses were characterized by rise and fall times in a range from (16–31) ns and (21–37) ns, respectively. Pulse amplitudes were adjusted from (54–64) kV and pulse durations set to 100 ns or 300 ns.

Accordingly, individual effects of each direct pulse parameter on the hydrogen peroxide production could be disentangled and related to the underlying development of discharges. Individual discharge events were electrically and optically analyzed to determine dissipated energy, propagation time and streamer length. Hydrogen peroxide concentrations were measured with an electrochemical flow injection analysis (FIA), from which the production efficiencies were summarily calculated.

## 2. Experimental setup

A schematic of the experimental setup is shown in figure 1, indicating discharge chamber, pulse generator, electrical and optical diagnostics, and typical signals for voltage figure 1(A), current figure 1(B), and light intensity figure 1(C).

### 2.1. Discharge generation

As previously reported in detail [24], discharges were ignited at a tip with a curvature radius of 35  $\mu\text{m}$  of an otherwise insulated tungsten needle electrode (*Metall Maier*, 99.95% purity) of 2 mm in diameter. The counter electrode was a titanium plate (*Selvan Fine + Metal GmbH*, 99.5%) with a diameter of 46 mm, which was set at a distance,  $d$ , of either 8 mm or 14 mm beneath the needle tip. Both electrodes were placed in the middle of a cylindrical chamber with a diameter of 20 mm made from polymethylmethacrylate. The volume was filled with deionized water, which was moved at a flow rate of 120 ml  $\text{min}^{-1}$  from bottom to top. A total volume of 75 ml of water was circulated.

Rectangular high-voltage pulses were applied with pulse durations,  $t_{\text{pulse}}$ , of 100 ns and 300 ns by two different, custom-built Blumlein line generators with pressurized spark gaps as closing switches. For the application of 100 ns pulses, pulse amplitudes,  $U_{\text{mean}}$ , could be adjusted between 54 kV and 64 kV (calculated as the average of voltages, which exceeded 90% of the highest applied voltage during a pulse). The edge steepness of the applied pulse could be modified by means of an adjustable inductance in parallel to the spark gap switch yielding rise times,  $t_{\text{rise}}$ , of 16 ns, 22 ns and 31 ns and concurrent fall times,  $t_{\text{fall}}$ , of 21 ns, 29 ns and 37 ns (both defined as the time that amplitudes changed from 10% to 90% of the highest applied voltage). For the application of 300 ns pulses, the amplitude was set at 61 kV and rise time and fall time to 10 ns and 23 ns, respectively. The voltage that was provided by both pulse generators was applied so that the needle was on a positive and the plate electrode on a negative potential with respect to the ground reference. A matching resistor of 250  $\Omega$ , connected in parallel to the electrodes, was chosen to prevent pulse reflections and deliver only single, well-defined pulses with a repetition rate of 1 Hz.

### 2.2. Electrical and optical diagnostics

The electrical and most of the optical diagnostics were similar to the setup described before [24]. High-voltage pulses were recorded according to the potential difference that was derived from the measurements of two passive high-voltage probes (*Tektronix*, P6015A) at either electrode. Typical recorded voltage signals for single pulses with a pulse duration of 100 ns and fall times of 21 ns, 29 ns or 37 ns are presented in figure 1(A) where also definitions for pulse amplitude, rise time, fall time and duration are indicated.

Corresponding current signals are shown in figure 1(B), which were measured with a Rogowski coil (*Magnelab*, CT-E2.5). The currents were corrected for displacement currents and Ohmic losses, which were derived from applied pulses that did not result in a visible discharge, as confirmed by the simultaneously recorded light emission. Accordingly, signals presented in figure 1(B) only show values for the actual discharge currents. Discharge current and corresponding voltage signal were multiplied and time-integrated to calculate the momentary electrical power and dissipated energy, respectively.

Emitted visual light intensity,  $I_L$ , was observed with a photodetector (*ThorLabs*, DET 10A). Typical results are shown in figure 1(C) for different fall times. In addition, characteristic times for discharge ignition,  $t_{\text{start}}$ , for discharge propagation,  $\Delta t$ , and the onset of discharge channel reillumination,  $t_{\text{min}}$ , are indicated. The reillumination is a typical observed phenomenon, which marked the end of the propagation of discharge filaments and corresponded to a change in polarity of the discharge current. A more detailed discussion of the electrical and optical signals was provided previously [24].

Together with the photodetector signals, temporal integrated images of the discharge development and especially the expansion were recorded with an ICCD camera (*Stanford Computer Optics*, 4Picos). Gate times of 200 ns and

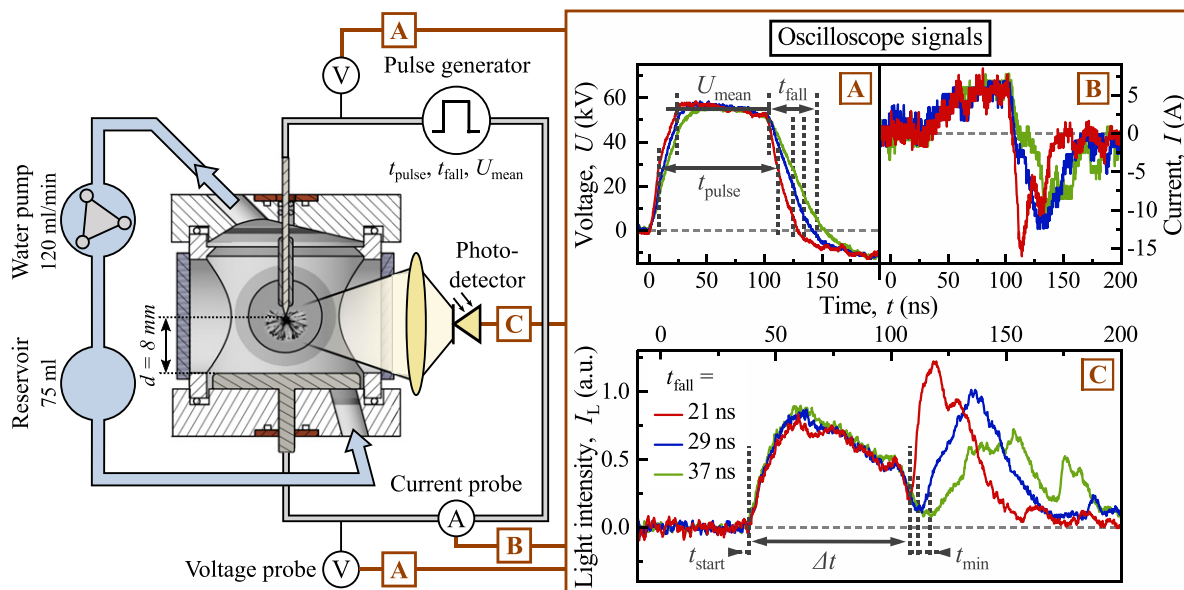


**Figure 1.** Schematic of the experimental setup, consisting of discharge chamber, pulse generator and diagnostics. Discharges were ignited in a needle-to-plate electrode configuration (submerged in water) with an interelectrode distance,  $d$ , and instigated by high-voltage pulses provided by a Blumlein line generator. Deionized water was circulated through the system by a peristaltic pump. Pulse amplitude,  $U_{\text{mean}}$ , pulse duration,  $t_{\text{pulse}}$ , pulse rise time,  $t_{\text{rise}}$ , and fall time,  $t_{\text{fall}}$ , were recorded in a differential measurement with two high-voltage probes (A), a Rogowski coil (B), and a photodetector (C). Typical signals for voltage (panel (A)), discharge current (panel (B)) and emitted light intensity (panel (C)) are shown for pulse steepnesses characterized by fall times of 21 ns, 29 ns and 37 ns. Images of every discharge event were recorded with an ICCD camera.

600 ns were chosen for pulses of 100 ns and 300 ns duration, respectively. Consequently, image acquisition times covered the entire propagation and reillumination phase for a discharge. Because discharges had stopped expanding when the reillumination began, the images show in particular the largest extend of the discharge. The previously used image analysis algorithm was improved and now detected end points and the length,  $L_{s,i}$ , of each discharge filament by tracing the brightest path connecting the needle electrode with individual end points (cf figure S1) [24].

### 2.3. Electrochemical determination of hydrogen peroxide

Concentrations of hydrogen peroxide that were generated by the discharges were quantified electrochemically with a FIA method, which was combined with a chronoamperometric detection [26, 27]. Experiments were performed with screen-printed three-electrode-systems (Metrohm, DRP-710) consisting of a working electrode functionalized with Prussian blue, a carbon counter electrode, and a silver reference electrode. A working potential of  $-0.1$  V was applied to the system and reaction currents were measured with a sampling rate of  $20$  s $^{-1}$  by a potentiostat (Metrohm, PGSTAT101).

Water was pumped through the discharge chamber for each experiment for 5 min without the instigation of any discharges before a reference sample of 4.5 ml was taken. After the discharges were applied, another sample was collected and both aliquots were separately mixed with 0.5 ml concentrated buffer solution ( $134.04$  g l $^{-1}$  KH $_2$ PO $_4$  +  $2.67$  g l $^{-1}$  Na $_2$ HPO $_4$  +  $74.52$  g l $^{-1}$  KCl dissolved in deionized water) containing

phosphate to stabilize the H $_2$ O $_2$ -concentration. Both samples were then stored in a refrigerator until the electrochemical measurements were conducted at the end of each day for all sample-pairs that were collected for different operating parameters. The earliest obtained samples were stored for 6 h at most. A control experiment showed no effects, i.e. increase or decrease in hydrogen peroxide concentrations, for continuous pumping for 1 h without discharge or storage of the solution for 10 h.

After all samples for an experimental series were gathered, a chip electrode was installed in the FIA-setup, moistened with running buffer and activated with several consecutive cyclic-voltammetric measurements until a stable voltammogram was obtained. A dilution of the concentrated buffer of 10% was used as running buffer. A calibration curve was then obtained by injecting hydrogen peroxide standard solutions of increasing concentration, i.e. (1, 2, 4, 6, 8, 10 and 15)  $\mu\text{mol l}^{-1}$  H $_2$ O $_2$  in running buffer, with three repetitions for each concentration. If a linear fit with a Pearson coefficient,  $R$ , of at least 0.999 was achieved, 500  $\mu\text{l}$  of reference and treated samples were injected into the FIA-system with five repetitions for each sample. This was followed by two injections of a higher concentrated standard solution (either (8, 10 or 15)  $\mu\text{mol l}^{-1}$ ) to perform a single peak calibration after the analysis of each sample to ensure electrode stability.

A detection limit of  $0.2$   $\mu\text{mol l}^{-1}$  and a recovery rate of 98.4% was achieved for a H $_2$ O $_2$  concentration of  $1$   $\mu\text{mol l}^{-1}$ . However, no sample with a concentration of less than  $2$   $\mu\text{mol l}^{-1}$  was obtained in the experiments.



Hydrogen peroxide production rate and efficiency was derived for each experiment separately using  $\text{H}_2\text{O}_2$  concentration and electrical as well as optical data. Discharge energy and propagation time of the individual discharge events were accumulated and related to the concentrations.

### 3. Results

Hydrogen peroxide production rate,  $k$ , and production efficiency,  $G$ , were characterized with respect to pertinent parameters of the high-voltage pulses that were applied to generate sub-microsecond pulsed streamer discharges in liquid water. An obvious influence was expected especially for pulse duration,  $t_{\text{pulse}}$ , and pulse amplitude,  $U_{\text{mean}}$ . Both determine to a large extent the discharge development, i.e. propagation time,  $\Delta t$ , and streamer length,  $L_s$ . The extend and duration of discharges are assumed to be predominantly responsible for the production of reactive species that are preceding the formation of hydrogen peroxide. However, both direct parameters together also affect time lags before discharge initiation, which is described by the inception time,  $t_{\text{start}}$ . Resulting characteristics of discharge propagation and associated inception probabilities consequently need to be taken into account for a comprehensive description. Concurrently, pulse steepness, expressed by rise and fall time,  $t_{\text{rise}}$  and  $t_{\text{fall}}$ , are parameters, which determine in particular reillumination processes and their contribution to the generation of species. The influence of the different factors on hydrogen peroxide production in relation to the responsible discharge characteristics are described in the subsequent sections.

#### 3.1. Hydrogen peroxide production efficiency increases with shorter pulse duration

Two pulse generators with different pulse durations of 100 ns and 300 ns were utilized to observe differences in discharge inception, discharge propagation, as well as the reillumination of discharge filaments after pulse application. The respective processes were related to the accumulated hydrogen peroxide production.

Due to the extended pulse duration, discharge filaments that were developing for 300 ns pulses were expected to be three times longer than for 100 ns pulses. To prevent arcing, the distance between needle and counter electrode was increased to 14 mm for the experiments with both pulse generators. Accordingly, pulse amplitudes were increased to 61 kV so that the electric field at the tip of the needle, which determines the onset of ionization mechanisms, was for the larger electrode gap the same as for the previously investigated shorter gap [24].

Reillumination is a characteristic phenomenon of sub-microsecond pulsed streamer discharges in liquid water, which is predominantly determined by fall times (cf figure 1). However, the reilluminated channels were already established during the application of the high-voltage pulses, depending on their respective parameters, i.e. pulse duration and amplitude. Therefore, the contribution of reillumination to hydrogen peroxide production was, in general, inherently included in the

comparison of pulse durations. However, for 100 ns pulses it was further investigated in more detail (and described in subsection 3.3). The results for the comparison of pulse durations are summarized in figure 2.

Typical images of single discharge events are presented in figure 2(A) for the application of pulses of both durations. All discharges showed filamentary structures, regardless of pulse duration, contained several channels and propagated into the medium away from the needle. Filaments ignited during a 300 ns pulse were, as expected, noticeably longer with more pronounced elongation toward the counter electrode when compared with the application of 100 ns pulses. Filaments propagating toward the counter electrode appeared more intense and branched more often with increasing distance to the needle electrode.

The individual streamer length,  $L_s$ , that was derived from the images of single discharge events (altogether 200 images for a duration of 100 ns and 400 images for a duration of 300 ns), depending on individual propagation times,  $\Delta t$ , are presented in figure 2(B). An algorithm analyzed all images and determined the distance,  $L_{s,i}$ , between the end of each filament and the needle tip (cf figure S1). For the application of 100 ns high-voltage pulses, streamer lengths fluctuated strongly between different discharge events. This was also a consequence of two-dimensional mapping of the discharge, which resulted in a loss of spatial information. A seemingly short filament could either actually be shorter or have propagated out of the imaging plane. Commonly, streamer lengths were determined as the maximal distance of the needle electrode to the end of a single filament [28, 29] or, on average, to the end of every filament end [24, 30]. Both methods neglect the structure of filaments, e.g. changing propagation directions due to branching. For a more precise measurement, the algorithm traced the luminous filaments from end to needle tip and determined the maximum streamer length,  $L_s$ , to sufficiently describe the discharge expansion. The streamer length, generally, grew linearly with propagation time for both pulse durations with similar growth rate, which could be described by the fitted averaged, constant propagation velocity,  $v_s$ , of  $(31.2 \pm 0.6) \text{ km s}^{-1}$ .

The probability distribution for the inception of discharges, i.e. start time,  $t_{\text{start}}$ , during the application of a pulse, is shown in figure 2(C). A representative pulse for each pulse duration is indicated in arbitrary units. Whereas the amplitude stayed close to the same value for a pulse duration of 300 ns (plateau), was the amplitude for the 100 ns pulse gradually decreasing by 9%. More than 30% of the discharges were ignited at the beginning of the 100 ns pulse, i.e. 32 ns into the pulse, where the pulse voltages reached the highest values. The probability for a discharge inception decreased for later times. Notably, the inception of discharges started later into the pulse for a duration of 300 ns with a maximum probability of 11% at 71 ns. This was observed despite the faster rise time of 10 ns in comparison to 16 ns for the 100 ns pulse. The distribution for the longer pulse was also broader and a second, local probability maximum can be observed around 250 ns into the pulse. The observed statistics suggest that, besides rise times,

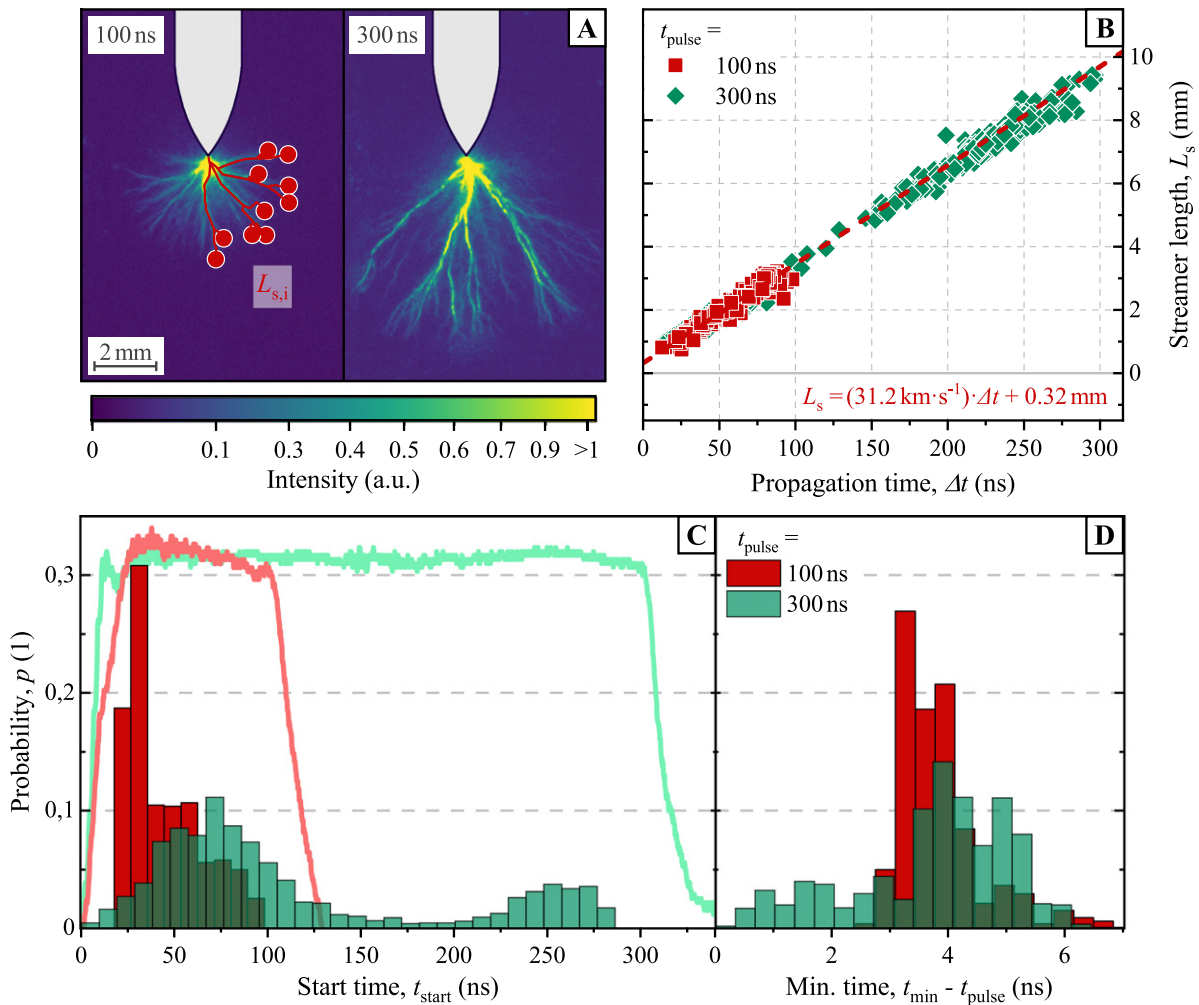


**Figure 2.** Images of discharge developments (panel (A), for the presentation, only half of the detected streamers are shown), from the images derived maximum streamer length,  $L_s$ , depending on propagation time,  $\Delta t$ , (panel (B)), inception time statistic, and reillumination time probability,  $p$ , (panel (C) and (D), respectively) for pulse durations of 100 ns (red symbols, lines and bars) and 300 ns (green symbols, lines and bars). The analysis included 200 discharges for the shorter and 400 discharges for the longer pulse duration. Streamer lengths increased linearly with propagation time and a fit yielded a mean propagation velocity,  $v_s$ , of  $(31.2 \pm 0.6) \text{ km s}^{-1}$ . The probability distribution of inception times corresponded to the pulse shapes, while the distribution for the onset of reillumination was not correlated with the pulse durations.

even small variations of pulse amplitudes could affect inception probability. A longer sustained and invariable amplitude seemed to encourage a broader distribution. With even slightly increasing voltages, there was also an increasing possibility to initiate discharges even late into the pulse.

The pulses had similar fall times of 21 ns and 23 ns for durations of 100 ns and 300 ns, respectively. Since reillumination is primarily determined by fall times, the statistic for the start of the reillumination of discharge filaments after pulse application, as expressed by the difference between  $t_{\text{min}}$  and  $t_{\text{pulse}}$  (cf figure 1), was similar for both pulse durations. The probability distribution peaked between 3 ns and 4 ns.

As shown in figure 2(A), filaments were approximately spherically distributed for 100 ns pulses. Spatial distributions were similar for the application of 300 ns pulses for equivalent propagation times. The continuing propagation showed a strong directionality toward the counter electrode for

longer propagation times. Only streamers propagating within a  $\pm 20^\circ$ -angle relative to the needle axis reached a length of 7.5 mm (assuming a constant propagation velocity, cf figure 2(B)). For larger angles, especially  $> |\pm 70^\circ|$ , streamer lengths of 2.5 mm were on the same order as for the propagation for 100 ns pulses. Accordingly, these streamers stopped their propagation early during the pulse. Details on the directionality and related spatial distributions of filaments are described in the supplemental information (cf figure S2).

The expanse of the discharge and the number of filaments that were generated conceivably determined the possible abundance of chemical reactions and the associated absolute production of reactive species. The parameters for spatial extend and distribution of discharge channels can be summarized by the discharge volume,  $V_D$ , which is described in figure 3 with respect to propagation time,  $\Delta t$ , for both pulse durations. For a comparison, the area of light emission in a particular image

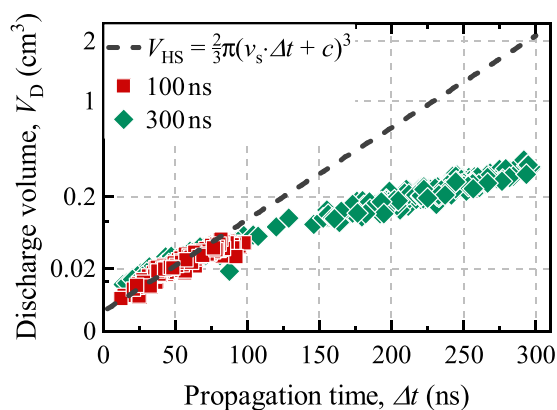


**Figure 3.** Discharge volume,  $V_D$ , associated with propagation time,  $\Delta t$ , for pulse durations of 100 ns and 300 ns. The derivation of the idealized equivalent half-sphere volume,  $V_{HS}$ , with radius  $L_s$  assumed a continuous expansion with a velocity  $v_s$ . The correlation of  $L_s$  with  $\Delta t$  was extracted from the measurements summarized in figure 2(B). Accordingly, discharge volumes grew proportional to  $L_s^3$ , i.e. cubical, but the growth rate declined after the first 100 ns of propagation.

(cf figure 2(A)) was determined by defining an arbitrary intensity limit (independent of absolute intensity values).

Discharges were generally expanding into a half-sphere away from the needle tip within an ideal volume,  $V_{HS}$ . The increasing volume could be calculated from the correlation of streamer lengths,  $L_s$ , to the propagation time of discharges,  $\Delta t$  (defined in figure 2(B)). Accordingly, discharge volumes were increasing with distance in a similar cubic fashion for 100 ns and 300 ns pulses for propagation times up to 100 ns. The subsequent later development for the longer pulses approximately retained the spherical propagation but with a slower growth rate (reflecting the described directionality). The resulting discharge volume was, therefore, much smaller than expected from the early propagation. Comparing the discharge volume,  $V_D$  with  $V_{HS}$ , discharges propagating for 300 ns filled a 80% smaller volume than expected from an expansion of a half sphere with constant velocity.

The rate of energy dissipation into discharge processes differed for both pulse durations regardless of comparable pulse amplitudes. Energy dissipation rates of  $0.16 \text{ mJ ns}^{-1}$  and  $0.12 \text{ mJ ns}^{-1}$  were measured for pulses of 100 ns and 300 ns, respectively. Notably, energy dissipation rates were smaller for longer pulses and altogether smaller than those described for an electrode distance of 8 mm.

Discharge volume and energy dissipation affected the observed hydrogen peroxide production and especially explain production rates and efficiencies that are shown in figure 4. Production rates and efficiencies were calculated with respect to the accumulated propagation time and energy dissipation of the discharges that were resulting in the determined hydrogen peroxide concentrations (for the application of either 200 or 400 pulses of the same operating parameters for pulse durations of 100 ns and 300 ns, respectively). The production rate, presented in figure 4(A), was approximately two times higher at  $(0.14 \pm 0.02) \text{ mol l}^{-1} \text{ s}^{-1}$  for the three times shorter pulse. The energy efficiency, shown in figure 4(B), was less

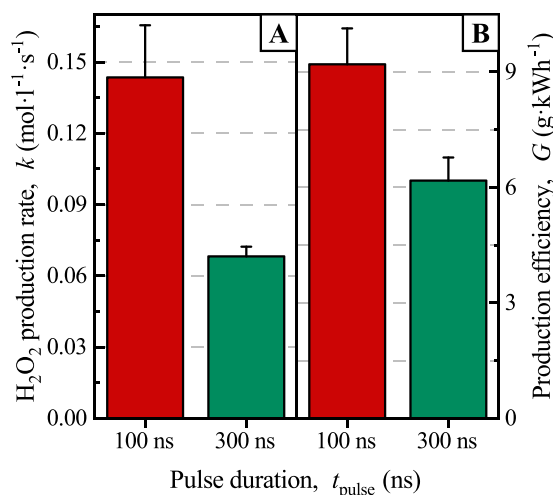


**Figure 4.** Rate (panel (A)) and efficiency (panel (B)) of hydrogen peroxide production for pulse durations of 100 ns and 300 ns. Both, rate and energy efficiency, increased for a shorter pulse duration.

affected. The production efficiency of hydrogen peroxide was  $(9.2 \pm 0.9) \text{ g kWh}^{-1}$  and  $(6.2 \pm 0.6) \text{ g kWh}^{-1}$  for a duration of 100 ns and 300 ns, respectively. Hence, even the reduced energy dissipation for longer propagation times did not counterbalance the reduced hydrogen peroxide production.

### 3.2. Hydrogen peroxide production rates increase linearly with pulse amplitude

The energy, provided to a discharge during a pulse is, for a given pulse duration, foremost determined by the pulse amplitude. Corollary, higher amplitudes promote earlier discharge inceptions and a higher probability for the generation of a discharge in general. However, in many respective investigations was the actual applied amplitude of a pulse strongly affected by the load, i.e. in the case of sub-microsecond pulsed streamer discharges in liquid water especially by water conductivity. Accordingly, pulse amplitudes are not necessarily corresponding to the output-settings of many pulse generators, which are usually designed for specific loads. Therefore, instead of a single pulse, reflections often disturb an unambiguous analysis of the influence of pulse amplitudes. A comprehensive understanding on how amplitudes affect hydrogen peroxide production is, hence, difficult. Consequently, a dedicated setup was established, which does not suffer from these limitations by controlling the impedance match between pulse generator and load together with differential measurements of the applied voltage.

Figure 5 shows the dependency of dissipated energy,  $E$ , mean start time,  $t_{start}$ , and  $\text{H}_2\text{O}_2$  production rate,  $k$ , on pulse amplitude,  $U_{mean}$ , in a range from 54 kV to 64 kV for single, well-defined pulses with a duration of 100 ns. Respective results were determined for 500 discharges for each value of the amplitude. For an unambiguous comparison, pulses with the steepest possible rise and fall time of 16 ns and 21 ns, respectively, were applied for an electrode distance of 8 mm. Accordingly, discharge inception was only affected by the variation of pulse amplitudes. Dissipated energies for

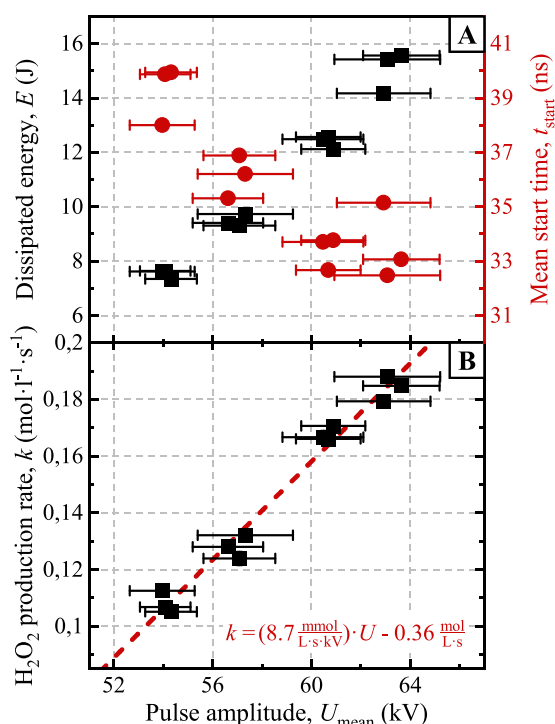


**Figure 5.** Total energy,  $E$ , dissipated for 500 accumulated discharges that were generated with 100 ns high-voltage pulses and their average starting time,  $t_{\text{start}}$ , (panel (A)) are shown together with hydrogen peroxide production rate,  $k$ , (panel (B)) for pulse amplitudes,  $U_{\text{mean}}$ , between 54 kV and 64 kV. Accumulated discharge energy and production rate increased linearly with pulse amplitude, while the mean starting time decreased.

each individual discharge were accumulated throughout the experiment and correlated with production rates, which were calculated from the sum of discharge propagation times of each set of the 500 investigated discharges and the amounts of  $\text{H}_2\text{O}_2$  that were formed accordingly.

The accumulated dissipated energy during discharge propagation increased linearly in a range from 8–16 J within the observed range of pulse amplitudes, as displayed in figure 5(A). The rate of energy dissipation, which is also linearly dependent on the pulse propagation time [24], increased by 100% from  $(0.21 \pm 0.04) \text{ mJ ns}^{-1}$  to  $(0.39 \pm 0.08) \text{ mJ ns}^{-1}$ . Simultaneously, the averaged starting time shortened from 39 ns to 32 ns, which corresponds to an average propagation time extended by 10%.

Hence, the difference in discharge inception could not be exclusively responsible for the observed increase in energy dissipation. Concurrently, the ignition probability of a discharge during a high-voltage pulse also increased with voltage. Starting at 47% for 54 kV, discharges occurred in 87% of all applied pulses with amplitudes of 64 kV. The significance of pulse amplitudes was already implicitly addressed by the statistics that were observed for different pulse durations as presented in figure 2(C). Concurrently, the lowest voltages that were applied with a 100 ns pulse were just sufficient to initiate a discharge. Associated with the low voltages were broadened inception time probability distributions.

As expected, hydrogen production rates were increasing with voltage and the associated higher energy dissipation, as shown in figure 5(B). Notably, the rates nearly doubled from  $100 \text{ mmol l}^{-1} \text{ s}^{-1}$  to  $190 \text{ mmol l}^{-1} \text{ s}^{-1}$  although the increase in pulse amplitude by about 19% was rather moderate. Applied amplitudes were prone to variations of approximately 4%, but a linear dependency was clearly identified and a fit yielded a growth rate of  $(8.7 \pm 0.4) \text{ mmol l}^{-1} \text{ s}^{-1} \text{ kV}^{-1}$ . The dependency of voltage with energy dissipation explains a stable, i.e. constant, production efficiency of  $\text{H}_2\text{O}_2$ . This suggests that the pulse amplitude was directly correlated to peroxide formation without affecting the formation pathway, i.e. by increasing the discharge temperature.

### 3.3. Hydrogen peroxide production is independent from pulse steepness

Pulse steepness was also expected to affect the production of hydrogen peroxide. Fast rise times presumably result in an earlier initiation of discharges during pulse application and eventually larger discharge volumes while fast fall times are conducive for a more pronounced reillumination [24]. Accordingly, inception and reillumination statistics were investigated with respect to hydrogen peroxide production for rise times,  $t_{\text{rise}}$ , of 16 ns, 22 ns and 31 ns, and corresponding fall times,  $t_{\text{fall}}$ , of 21 ns, 29 ns and 37 ns. The pulse amplitude was set at 56 kV for an electrode distance,  $d$ , of 8 mm. Histograms for both statistics are presented in figure 6.

Each histogram includes measurements for 2700 discharge events. Probabilities,  $p$ , were expressed for the time of inception for different rise times with respect to the discharge beginning,  $t_{\text{start}}$ , or for the onset of reillumination,  $t_{\text{min}}$ , according to different fall times. Discharge inception for the shortest rise time, i.e. the steepest pulses, peaked (highest probability) at 25 ns, while the probability for a discharge inception later than 35 ns did not exceed 5%.

An increasing rise time resulted in a prolonged inception time from 30 ns and 32 ns, which was associated with a broadening of the probability distribution. Comparing the probability distributions for each rise time, it was reasonable to assume that the different maximum probabilities of 27% at 25 ns, 14% at 30 ns or 10% at 32 ns were a result of the different pulse shapes. In this respect, it should be mentioned again that the gradual decrease of voltage amplitudes during 100 ns pulses was more pronounced for shorter rise times, which was already described for figure 2(C). Correspondingly, probability distributions for inception shifted to later times and broadened.

Fall times mainly influenced the reillumination start. A narrow probability distribution for  $t_{\text{min}}$  with a width of 1 ns and a maximum of 45% at 4 ns was observed for the shortest rise and fall time. Similar to the inception probabilities, the maxima of the probability distributions were delayed from 5 ns and 7 ns and broadened for the longest rise and fall times.

Although pulse steepness did affect details of the discharge development, interestingly the overall propagation times, from discharge inception until onset of reillumination, were rather similar, i.e. between 69 ns and 71 ns, for all investigated conditions. The comparison of the comprehensive discharge



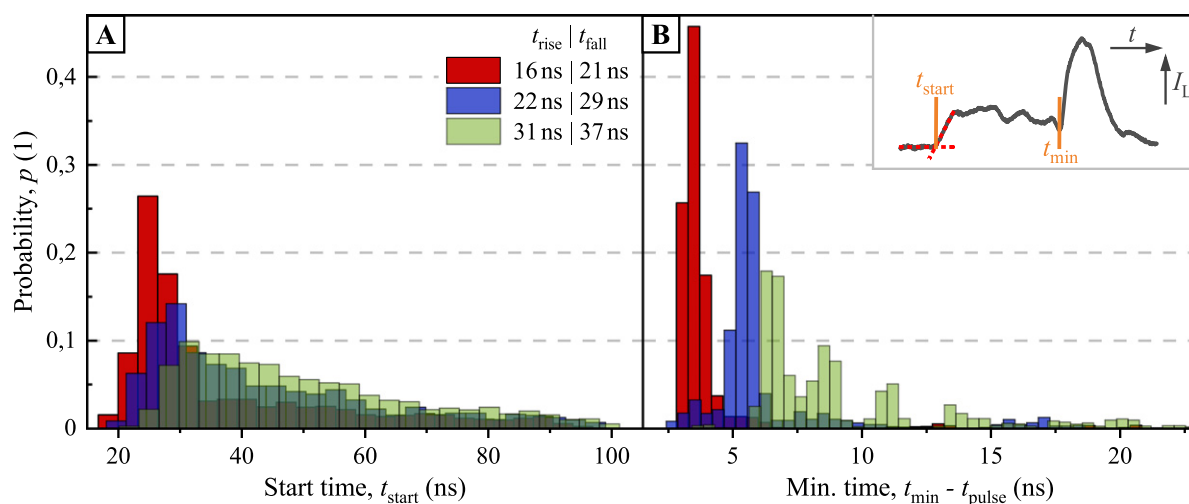


**Figure 6.** Probability distributions for inception times (panel (A)) and reillumination times (panel (B)) for an electrode distance,  $d$ , of 8 mm, a pulse amplitude,  $U_{\text{mean}}$ , of 56 kV and fall times,  $t_{\text{fall}}$ , of 21 ns (red bars), 29 ns (blue bars) as well as 37 ns (green bars). Altogether 2700 discharges were included in the analysis for each rise and fall time. Discharge inception was described by the time of first observable light emission,  $t_{\text{start}}$ , while the beginning of reillumination was associated with the time,  $t_{\text{min}}$ , when the discharge current changed polarity. For the shortest rise time, 27% of the discharges were incepted 25 ns into the applied high-voltage pulse and 45% of the discharges were reilluminating at 108 ns. Both probability distributions were broadened and delayed for increasing rise- and fall times.

development of 900 discharge events, i.e. summing up their individual propagation times, yielded also only marginally different total discharge propagation times between 62  $\mu\text{s}$  and 64  $\mu\text{s}$ . Accordingly, the corresponding times for radical production and discharge volumes were similar. This explains why no significant difference between the hydrogen peroxide production rates,  $k$ , of  $(147 \pm 5) \text{ mmol l}^{-1} \text{ s}^{-1}$ ,  $(143 \pm 3) \text{ mmol l}^{-1} \text{ s}^{-1}$ , and  $(145 \pm 7) \text{ mmol l}^{-1} \text{ s}^{-1}$  were observed for decreasing pulse steepness (figure S3). Mean discharge energies were likewise constant, consolidating previous results [24]. Summarily, an overall constant discharge propagation time resulted in a comparable hydrogen peroxide chemistry regardless of pulse steepness. Accordingly, a constant  $\text{H}_2\text{O}_2$  production efficiency of  $(5.8 \pm 0.1) \text{ g kWh}^{-1}$  was typical for the application of 100 ns pulses with an amplitude of 56 kV.

Notably, this assessment only includes the application of high-voltage pulses, which resulted in a discharge event. Considering the probability of ignition by comparing the total number of applied pulses with the number of actual discharge events (2700 per pulse steepness) yielded a decreasing ignition probability of 58%, 33%, and 29% with increasing rise time (and associated increasing fall time). Taking the applied pulses with ‘failed’ ignition into account, hydrogen peroxide production rates would falsely be assumed to decrease to  $85 \text{ mmol l}^{-1} \text{ s}^{-1}$ ,  $47 \text{ mmol l}^{-1} \text{ s}^{-1}$ , and  $42 \text{ mmol l}^{-1} \text{ s}^{-1}$  when calculated with the number of pulses instead of discharge events. Overall, the ignition probability clearly needs to be considered and reported for the description of respective experiments to prevent wrongful conclusions on the production of reactive species for repetitively applied high-voltage pulses.

#### 4. Discussion

Reaction chemistry for sub-microsecond pulsed streamer discharges in liquid water was investigated by quantifying the indicative hydrogen peroxide production depending on direct pulse parameters, i.e. pulse duration, pulse amplitude and pulse steepness. The highest peroxide production rate found was  $9.2 \text{ g kWh}^{-1}$ , which is higher than previously reported by comparable studies, e.g. ca.  $2 \text{ g kWh}^{-1}$  [9],  $4.6 \text{ g kWh}^{-1}$  [11],  $0.8 \text{ g kWh}^{-1}$  [1] or  $(0.46\text{--}3.64) \text{ g kWh}^{-1}$  [6]. The difference to our results could conceivably be explained by the fact, that previous studies did not necessarily exclude applied high voltage pulses, which did not result in a discharge event and only contributed Ohmic losses. In addition, the comparison confirms the significance of a dedicated control of pulse parameters to improve the performance of the method. The best peroxide production rate found was  $9.2 \text{ g kWh}^{-1}$ , which is on the same order of magnitude but higher as in comparable studies [1, 6, 9, 11].

Dominant influence on  $\text{H}_2\text{O}_2$  production could be attributed to pulse duration and pulse amplitude. An extended pulse duration eventually led to the stopping of discharge filaments, which was accompanied by decreased hydrogen peroxide production rates and efficiencies. A rather small increase in pulse amplitude of approximately 20% nearly doubled the energy dissipation and the production rate. Although pulse steepness did affect discharge developments, i.e. statistics of inception times and the contribution of the reillumination processes, and probably influenced the discharge inception, i.e. direct or indirect breakdown, as proposed in the literature, the respective effect on  $\text{H}_2\text{O}_2$  production was marginal or negligible in com-

parison to pulse duration and amplitude [31, 32]. Altogether, production rates and achieved concentrations of species were primarily determined by differences in dissipated energies in relation to pulse parameters. However, the energy could not be arbitrarily increased for a given discharge structure but instead was eventually distributed in longer or more discharge channels. Accordingly, the overall discharge volume was crucial for an effective generation of species. This could explain the observed higher rates and efficiencies for hydrogen peroxide production for the application of higher pulse amplitudes and shorter pulse durations.

#### 4.1. Discharge development depends on pulse parameters

For needle-to-plate geometries, plasma parameters, such as electron density and temperature have already been investigated. Although these studies rather investigated specific conditions but not a dedicated variation of pulse parameters, such as pulse durations, pulse amplitude or pulse steepness, selected settings were investigated for a range of several orders of magnitude, e.g. rise times of (0.1–100) ns, pulse amplitudes from (10–100) kV and pulse durations from 6 ns–10  $\mu$ s. Nonetheless, electron densities were reported to be relatively stable between ( $10^{18}$ – $10^{19}$ )  $\text{cm}^{-3}$  (with some outliers of ( $10^{17}$  and  $10^{20}$ )  $\text{cm}^{-3}$ ). Rotational temperatures of (2000–4000) K, black body radiation for temperatures of (7000–15000) K, and electron energies of (1–3) eV were also reported [6, 30, 33–40]. These results present a good overview of pertinent plasma characteristics for sub-microsecond pulsed streamer discharges in liquid water and this study adds a detailed investigation on the dependency of electrical and optical plasma properties on pulse parameters.

Propagation time and streamer length of individual discharge channels were increasing with extended pulse duration (figure 2(B)). However, the start of a discharge was, on average, delayed by about 40 ns for longer pulses (figure 2(C)). Conversely, the onset of the reillumination occurred for rather similar delays for both pulse durations (figure 2(D)). Consequently, the propagation time was 2.8 times longer for the application of 300 ns pulses in comparison to 100 ns pulses.

According to literature, sub-microsecond pulsed streamer discharges in liquid water that were instigated with pulses with durations in the order of 100 ns propagate with a constant velocity of about 30  $\text{km s}^{-1}$  [20, 22, 24]. This could be confirmed (figure 2(B)).

The typical propagation time of 62 ns for the application of 100 ns pulses corresponded to streamer lengths of 1.9 mm, while the filaments extend up to a typical length of 5.6 mm for a pulse duration of 300 ns (figure 2(B)). Individual channels could be much longer (but also shorter) since a typical inception time for the application of 300 ns pulses is prone to larger deviations from the mean (figure 2(C)).

Propagation times and resulting streamer length were to a lesser extend also depending on pulse amplitudes (figure 5(B)). Discharges were starting earlier during the application of a 100 ns pulse by 7 ns when pulse amplitudes were increased

from 54 kV to 64 kV, which resulted in an increase in streamer length by 10%.

Pulse steepness, i.e. rise and fall times, had actually no significant effect on propagation times and streamer length. This finding was especially surprising, as previous studies showed a significant impact of the pulse rise time on discharge inception and an effect of pulse fall time on discharge reillumination [24, 31, 32]. A decreasing edge steepness impacted the discharge by a broadening of inception and reillumination time statistics. On average, discharge inception and the beginning of the reillumination phase were both delayed in a similar fashion (figure 6). Consequently, averaged propagation times turned out independent from rise or fall time.

Since the discharge channels are the origin for the generation of reactive species, the correlation of discharge expanse with  $\text{H}_2\text{O}_2$  production is eminent. However, the actual discharge volume is also determined by the number of discharge channels and their distribution in addition to average (or maximal) streamer length. Unfortunately, these characteristics escape a statistical evaluation from 2D images. The respective assessment should be the dedicated topic of future studies, i.e. how streamer distribution and their individual properties depend on pulse parameters. However, some conclusions and conjectures were already possible without detailed information on the three dimensional discharge behavior. For pulses of about 100 ns duration, not only the extend of filaments that were originating along a thin wire at the center of a coaxial electrode system but also their number decreased when pulse amplitudes were lowered [10]. For the here investigated needle-to-plate geometry, this observation conceivably corresponded to the decrease in ignition probability for lower voltages. Concurrently, the number of filaments was possibly reduced and, accordingly, the overall discharge volume.

Images of the discharge development further show that discharge volumes and streamer lengths were not directly related for different pulse parameters (figure 2(A)). Discharge propagation and associated distribution of filaments were not generally isotropic or homogeneous. Instead, discharges exhibited a directionality toward the counter electrode for longer propagation times, which was, hence, more prominent for longer pulse durations of 300 ns. This resulted in an eventually decreasing growth rate of discharge volumes (figure 3).

For an isotropic propagation throughout the discharge development, a minimal electric field strength would have to be maintained in all directions to sustain ionization at all channel heads [24]. However, the electric field between a needle and plate is inherently inhomogeneous, decreasing away from the needle and more strongly for directions away from the needle axis [41]. Therefore, streamers heading directly toward the counter electrode were able to expand longer than streamers propagating in an askew direction, resulting in a decreased growth rate of the discharge volume. If the electric field fell below the critical field strength, continuous propagation stopped and instead a stepwise expansion ensued, provided that energy input into the channels is sustained [22].

#### 4.2. Energy dissipation depends on discharge development

Discharges developed from the tip of the high-voltage electrode—originating from a distinct root point—as a single streamer, which could branch several times during its propagation with a constant velocity. The result was a complex morphology with distinct filaments, i.e. plasma channels connecting electrode and one of the streamer heads that either reached their full expansion (determined by propagation velocity and pulse duration) or already stopped earlier instead.

The production of reactive species and, therefore, the indicative amount of hydrogen peroxide was primarily depending on overall achieved discharge volumes. This volume was determined by the energy that could be provided into the discharge regardless of the underlying structure. The energy that was dissipated in a sub-microsecond pulsed streamer discharges in liquid water was found to depend linearly on the propagation time for a fixed set of operating parameters [24, 42]. Accordingly, the continuing extension of a filament by ionization, radiation, recombination processes, etc, needed a constant amount of energy for the same incremental growth. This assumption is supported by investigations on plasma parameters, e.g. electron density, temperatures and energies, which are relatively stable for different experimental settings [6, 30, 33–40]. The intrinsic discharge morphology can be described by an instructive ‘single streamer’ model, which summarizes the filamentous structure, including filament radii and number of heads, i.e. head-charges, by an unbranched ‘single streamer’ with a distinct discharge volume [24]. The constant rate of energy dissipation in a single streamer and the associated discharge volume,  $V_D$ , implies a limited number of filaments that can be included in this streamer because the expansion of each additional filament would have to dissipate additional energy that is not necessarily available. Conversely, an energy dissipation, which was increasing with pulse amplitude (figure 5(A)), combined with an insignificant change of streamer length, hence, had to be associated with an increasing number of filaments. Since energy dissipation rate and pulse amplitude were proportional, the correlation between the number of filaments and energy dissipation also had to be linear. Previous observations on the number of streamers in a coaxial discharge configuration that were increasing with applied pulse amplitudes support assumption and approach [10].

Consequently, hydrogen peroxide production should also depend in a similar fashion, i.e. linearly, on pulse durations, since propagation velocity and energy dissipation rate were constant (figure 4(B)). However, the  $H_2O_2$ -production rates and -efficiencies that were observed, were much lower than expected from the indeed lower energy that was dissipated for the longer pulses. The pronounced directionality of the streamers for 300 ns pulses toward the plate electrode offers an explanation in agreement with the ‘single streamer’ model.

The increasing inhomogeneity of the electric field across larger distances from the needle tip resulted in early stopping of filaments that went askew. This corresponded to a lower energy dissipation rate of about 25% for the 300 ns high-voltage pulses. This reduction is not sufficient to explain the

actually much stronger decreasing hydrogen peroxide production rate by 50% or the production efficiency, which was smaller by 33% (figure 4). Instead, the results implicate a significantly reduced growth rate of discharge volume for discharges that were generated with 300 ns high-voltage pulses, in addition to the lower energy dissipation rate, in comparison with 100 ns high-voltage pulses. (Although overall discharge volumes were still larger for longer pulses.) On the one hand, filaments that stopped their propagation during the longer pulses could continue dissipating their share on the provided energy due to a step-wise propagation [22]. On the other hand, the filaments that continued propagation could branch whenever another filament stopped and, therefore, dissipated the still available energy, as this was required for a continued constant propagation according to the ‘single streamer’ model, but at the cost of a higher rate of energy dissipation for this ‘forced’ branching.

Filaments propagating sideways appeared rather dark, which seems contradictory to the hypothesized step-wise propagation. Filaments on a more direct trajectory to the counter electrode, which expanded for longer than 100 ns, showed instead additional branching as demanded by the ‘single streamer’ model. Accordingly, at a distance of 3–4 mm away from the needle tip, most of the filaments that came that far branched and branching became more likely for even larger distances. These filaments appeared brighter due to their extended propagation, i.e. light was emitted for longer times, and due to an increased current flowing through the existing channels to sustain ionization for the additional channel heads.

This was associated with a limited but higher conductivity of each remaining filament [7, 24]. Corresponding were a higher resistance and related greater resistive losses. The associated Joule heating scaled with filament length and quadratically with the current density within a discharge channel. Hence, if a filament of the streamer that propagated sideways stopped due to an insufficient electric field and simultaneously a filament directed toward the counter electrode branched, the energy for the continuing propagation of the latter became smaller. Accordingly, the energy available for expansion of the streamer decreased with every filament that stopped. Consequently, some filaments that were stopping did not induce further branching, i.e. fewer new filaments could be formed, corresponding to a reduced volume growth rate.

#### 4.3. Hydrogen peroxide production depends on energy dissipation and discharge volume

The investigations revealed that the formation of reactive species and consequently hydrogen peroxide production depended on the discharge volumes,  $V_D$ , which could be established during the application of high-voltage pulses. A higher energy dissipation, which could be provided by either longer pulse durations or higher pulse amplitudes, was expended in an expanse of discharge volumes. This included, on the one hand, a larger extension away from the origin of streamers, i.e. the needle tip, and, on the other hand, encouraged branching of filaments.

The growth of individual discharge filaments was associated with a constant dissipation of energy per increase in

length. This resulted, for a fixed set of parameters, in a stable energy density within filaments and a corresponding steady radical production (per unit length). For increasing pulse amplitudes, the energy density still had to be stable but the energy dissipation rate grew. Accordingly, the number of filaments increased resulting in higher hydrogen peroxide production rates for 100 ns pulses (figure 5(B)).

A rigorous assessment of the filamentary discharge structures, depending on pulse duration and pulse amplitude, that were filling and determining the actual discharge volume, is currently difficult. However, maximum streamer lengths,  $L_s$ , and associated propagation times,  $\Delta t$ , provided a reasonable comparison (figure 3). Notably, the rate of increase in discharge volume slowed down for propagation times of more than 100 ns. This emphasizes the electric field at the streamer head as driving force of the streamer propagation. In the inhomogeneous needle-to-plate geometry, it became increasingly difficult to sustain ionization processes, especially away from the extended needle axis. In fact, filaments that were initially propagating at larger angles away from the needle tip eventually stopped (cf figure S2). Concurrently, the volume growth rate of the still propagating channels was reduced due to energy losses in the discharge. Notably, the increased channel temperature due to Joule heating, which is supposed to induce increased radical formation [6, 7, 9, 17], did not counteract the smaller volume growth rate and, consequently, hydrogen peroxide production rates decreased (figure 4).

As a consequence, the growth of discharge volume could be related to the amounts of hydrogen peroxide with typical production rates of  $(0.14 \pm 0.02) \text{ mol l}^{-1} \text{ s}^{-1}$  for 100 ns pulses and  $(0.068 \pm 0.004) \text{ mol l}^{-1} \text{ s}^{-1}$  for pulse durations of 300 ns (figure 4(A)). The two times lower rate for the longer pulse was explained by the reduced discharge volume growth rate due to an increasing directionality and associated fewer filaments. For an extended propagation period, the ratio between volume growth and energy dissipation rate of a discharge decreased. Therefore, not only the rate of hydrogen peroxide production was reduced but also the energy efficiency of the production. However, since the generation of sub-microsecond pulsed streamer discharges in liquid water depends on inhomogeneous electrode configurations, this instructs shorter pulse durations as more efficient (figure 4(B)).

## 5. Conclusions

The individual influence of three direct pulse parameter, i.e. pulse steepness, amplitude and duration, on the production of hydrogen peroxide in a sub-microsecond pulsed streamer discharges in liquid water could be investigated. The implementation of an optical and electrical diagnostic that could resolve the temporal development of individual discharges, e.g. automated determination of discharge currents and streamer length, facilitated an association between pulse parameter and hydrogen peroxide production. The energy dissipation rate in relation to the discharge volume were identified to primarily affect peroxide production rate and energy efficiency.

Increasing the energy dissipation rate, i.e. increasing the pulse amplitude, led to an increased hydrogen peroxide production rate with a constant production efficiency, as increasing numbers of filaments were formed. The stopping of channels due to an inhomogeneous electric field reduced the ratio between volume expansion and energy dissipation rate, which yielded lower hydrogen peroxide production rate and efficiency.

The relation between discharge volume and hydrogen peroxide was based on the statistical analysis of two-dimensional images, which revealed valuable structural characteristics of the discharge. However, a full 3D-reconstruction of the filamentary structure may enable an exact analysis of streamer quantity as well as quantification of occupied volume and may support the presented correlation. Our image analysis algorithm, which traces the discharge filaments, may provide the basis of such a reconstruction.

As the energy dissipation directly corresponds to increasing hydrogen peroxide production rates for increasing pulse amplitudes, the question arises for any application if there is a limit for this correlation and how much energy could be dissipated in a single discharge. Additionally, the method of increasing energy dissipation, e.g. via pulse amplitude, repetition frequency or water conductivity, may benefit the coupling between discharge energy and chemistry and should be investigated in more detail.

With respect to frequency, hydrogen peroxide was produced in the scope of this study by several hundred consecutive discharges. Hence the interaction between discharges and already existing hydrogen peroxide in solution could have reduced production rates. Therefore, an analysis of hydrogen peroxide production in single discharge events may be considered in the future.

## Acknowledgments

The authors appreciate the research structure and the supportive background of the Leibniz Institute for Plasma Science and Technology (INP). Special thanks are given to Hans Höft for constructive discussions on experiments and data analysis.

## Data availability statement

The data that support the findings of this study are available upon reasonable request from the authors.

## ORCID iDs

Raphael Rataj  <https://orcid.org/0000-0002-7777-0367>  
Juergen F Kolb  <https://orcid.org/0000-0002-0434-5001>

## References

- [1] Banaschik R, Lukes P, Miron C, Banaschik R, Pipa A V, Fricke K, Bednarski P J and Kolb J F 2017 *Electrochim. Acta* **245** 539–48



- [2] Dang T H, Denat A, Lesaint O and Teissedre G 2008 *Plasma Sources Sci. Technol.* **17** 024013
- [3] Schneider M, Rataj R, Kolb J F and Bláha L 2020 *Environ. Pollut.* **266** 115423
- [4] Banaschik R, Jablonowski H, Bednarski P J and Kolb J F 2018 *J. Hazard. Mater.* **342** 651–60
- [5] Kaufman F and Del Greco F P 1961 *J. Chem. Phys.* **35** 1895
- [6] Locke B R and Shih K-Y 2011 *Plasma Sources Sci. Technol.* **20** 034006
- [7] Locke B R and Thagard S M 2012 *Plasma Chem. Plasma Process.* **32** 875–917
- [8] Banaschik R, Lukes P, Jablonowski H, Hammer M U, Weltmann K-D and Kolb J F 2015 *Water Res.* **84** 127
- [9] Chauvet L, Nenbangkao C, Grosse K and Keudell A 2020 *Plasma Process. Polym.* **17** 1900192
- [10] Banaschik R, Koch F, Kolb J F and Weltmann K-D 2014 *IEEE Trans. Plasma Sci.* **42** 2736–7
- [11] Nguyen T S, Rond C, Vega A, Duten X and Forget S 2020 *Plasma Chem. Plasma Process.* **40** 955–69
- [12] Joshi A A, Locke B R, Arce P and Finney W C 1995 *J. Hazard. Mater.* **41** 3–30
- [13] Lukes P, Appleton A T and Locke B R 2004 *IEEE Trans. Ind. Appl.* **40** 60–7
- [14] Yang S, Zhang L, Cui F and Ma J 2009 *2009 3rd Int. Conf. Bioinformatics and Biomedical Engineering* (Piscataway, NJ: IEEE) pp 1–4
- [15] Li S, Hu S and Zhang H 2011 *IEEE Trans. Plasma Sci.* **40** 63–7
- [16] Wen J, Li Y, Zhang M and Zhang G 2019 *2019 IEEE 20th Int. Conf. Dielectric Liquids (ICDL)* (Piscataway, NJ: IEEE) pp 1–4
- [17] Medodovic S and Locke B R 2009 *J. Phys. D: Appl. Phys.* **42** 049801
- [18] Palmer A W and House H 1972 *J. Phys. D: Appl. Phys.* **5** 1106
- [19] Gzowski O A, Wlodarski R, Hesketh T R and Lewis T J 1966 *Br. J. Appl. Phys.* **17** 1483
- [20] Marinov I, Guaitella O, Rousseau A and Starikovskaia S M 2013 *J. Phys. D: Appl. Phys.* **46** 464013
- [21] Fujita H, Kanazawa S, Ohtani K, Komiya A, Kaneko T and Sato T 2014 *J. Appl. Phys.* **116** 213301
- [22] Ceccato P H, Guaitella O, Le Gloahec M R and Rousseau A 2010 *J. Phys. D: Appl. Phys.* **43** 175202
- [23] Seepersad Y, Fridman A and Dobrynin D 2015 *J. Phys. D: Appl. Phys.* **48** 424012
- [24] Rataj R, Höft H and Kolb J F 2019 *Plasma Sources Sci. Technol.* **28** 125002
- [25] Huiskamp T 2020 *Plasma Sources Sci. Technol.* **29** 023002
- [26] Trojanowicz M 2009 *Anal. Chim. Acta* **653** 36–58
- [27] Ricci F and Palleschi G 2005 *Biosens. Bioelectron.* **21** 389–407
- [28] Šimek M, Hoffer P, Prukner V and Schmidt J 2020 *Plasma Sources Sci. Technol.* **29** 095001
- [29] Pongráč B, Šimek M, Ondáč P, Člupek M, Babický V and Lukeš P 2019 *Plasma Sources Sci. Technol.* **28** 02LT02
- [30] Grosse K, Schulz-von der Gathen V and von Keudell A 2020 *Plasma Sources Sci. Technol.* **29** 095008
- [31] Pekker M, Seepersad Y, Shneider M N, Fridman A and Dobrynin D 2013 *J. Phys. D: Appl. Phys.* **47** 025502
- [32] Tereshonok D V, Babaeva N Y, Naidis G V and Smirnov B M 2016 *J. Phys. D: Appl. Phys.* **49** 505501
- [33] An W, Baumung K and Bluhm H 2007 *J. Appl. Phys.* **101** 053302
- [34] Salazar J N, Bonifaci N, Denat A and Lesaint O 2005 *2005 IEEE Int. Conf. Dielectric Liquids (ICDL)* (Piscataway, NJ: IEEE) p 91
- [35] Namihira T, Sakai S, Yamaguchi T, Yamamoto K, Yamada C, Kiyama T, Sakugawa T, Katsuki S and Akiyama H 2007 *IEEE Trans. Plasma Sci.* **35** 614–8
- [36] Šunka P 2001 *Phys. Plasmas* **8** 2587–94
- [37] Dobrynin D, Seepersad Y, Pekker M, Shneider M, Friedman G and Fridman A 2013 *J. Phys. D: Appl. Phys.* **46** 105201
- [38] Marinov I, Starikovskaia S and Rousseau A 2014 *J. Phys. D: Appl. Phys.* **47** 224017
- [39] Pongráč B, Šimek M, Člupek M, Babický V and Lukeš P 2018 *J. Phys. D: Appl. Phys.* **51** 124001
- [40] Bruggeman P J et al 2016 *Plasma Sources Sci. Technol.* **25** 053002
- [41] Deutsch W 1933 *Ann. Phys.* **408** 588–612
- [42] Qin J and Pasko V P 2014 *J. Phys. D: Appl. Phys.* **47** 435202



## Article 3

### Authors

Raphael Rataj  
Matthias Werneburg  
Harald Below  
Jürgen F. Kolb

### Title

Hydrogen Peroxide Production of Individual Nanosecond Pulsed Discharges Submerged in Water of Elevated Conductivity

### Journal

ChemPhysChem (accepted)

Online: <https://chemistry-europe.onlinelibrary.wiley.com/doi/full/10.1002/cphc.202300143>

DOI: <https://doi.org/10.1002/cphc.202300143>

Reprinted with kind permission from:

ChemPhysChem

Reproduced under terms of the CC BY-NC-ND 4.0 license. Copyright 2023 by the authors and published by Wiley-VCH GmbH.





# Hydrogen Peroxide Production of Individual Nanosecond Pulsed Discharges Submerged in Water of Elevated Conductivity

Raphael Rataj,<sup>\*[a, b]</sup> Matthias Werneburg,<sup>[c]</sup> Harald Below,<sup>[d]</sup> and Juergen F. Kolb<sup>\*[a, b]</sup>

The production of hydrogen peroxide (H<sub>2</sub>O<sub>2</sub>) is a key parameter for the performance of pulsed discharges submerged in water utilized as advanced oxidation process. So far, any related assessment of the underlying mechanism was conducted for the application of several hundred discharges, which did not allow for a correlation with physical processes. Moreover, the production was rarely investigated depending on water conductivity as one of the most important parameters for the development of submerged discharges. Accordingly, hydrogen peroxide generation was investigated here for individual single discharge events instigated with 100 ns high-voltage pulses in water with three different conductivities and was associated with the discharge development, i.e. spatial expansion and

dissipated electrical energy. The approach necessitated the improvement of an electrochemical flow injection analysis based on the reaction of Prussian blue with H<sub>2</sub>O<sub>2</sub>. Hydrogen peroxide concentrations were quadratically increasing with propagation time and stable for different water conductivities. H<sub>2</sub>O<sub>2</sub> production per unit volume of a discharge was constant over time with an estimated rate constant of 3.2 mol·m<sup>-1</sup>·s<sup>-1</sup>, averaged over the cross-sectional area of all discharge filaments. However, the individually dissipated energy increased with conductivity, hence, the production efficiency decreased from 6.1 g·kWh<sup>-1</sup> to 1.4 g·kWh<sup>-1</sup>, which was explained by increased resistive losses within the bulk liquid.

## Introduction

Pulsed streamer discharges, instigated directly in an aqueous solution, were shown to effectively degrade various toxic pollutants.<sup>[1–7]</sup> As a treatment method, streamer discharges do not rely on any additional chemicals or catalysts, while residual reactive species eventually recombine to water, oxygen and hydrogen. Hence, the treatment is considered to provide a sustainable water purification process, which will be essential for drinking water and waste water treatment to overcome global environmental challenges induced by anthropogenic

pollutants like per- and polyfluoroalkyl substances (PFAS), pharmaceuticals and agricultural plant protection products in the future.

Applications of pulsed streamer discharges are contextualized as advanced oxidation process as they exploit the production of oxidative radicals, e.g. ·O, ·OH, ·HO<sub>2</sub>. While all of the radicals possibly contribute to degradation, hydroxyl radicals are considered especially important for the oxidation of stable bonds, including ring cleavage of organic compounds.<sup>[5]</sup>

However, hydroxyl radicals are short-lived with a life time of less than 3 μs<sup>[8]</sup> and, without other reaction partners, readily recombine to more stable hydrogen peroxide (H<sub>2</sub>O<sub>2</sub>). Respective concentrations are, therefore, an accepted measure for the reliable characterization of hydroxyl production rates.<sup>[5,9,10]</sup>

Accordingly, investigations to improve operating parameters for submerged discharges, in particular for water decontamination, have relied on the assessment of hydrogen peroxide production rates. Increasing pulse amplitude,<sup>[11–17]</sup> duration,<sup>[15,17,18]</sup> and repetition frequency<sup>[16,17]</sup> resulted in a higher concentration. Water pH-value and electrode material did not have any effect, despite catalytic H<sub>2</sub>O<sub>2</sub>-cleavage due to metal impurities as a result of electrode erosion.<sup>[4,19,20]</sup> Water conductivities are obviously an important parameter for operation and applications. For surface waters they span a range from (0.3–60) mS·cm<sup>-1</sup>, i.e. three orders of magnitude, which cannot be easily accommodated by electrical systems. Concurrently, the effect on hydrogen peroxide production was so far not conclusive. Both decreasing and increasing concentrations of H<sub>2</sub>O<sub>2</sub>, as well as no changes, have been reported for increasing conductivities.<sup>[9,18,20–24]</sup> A possible explanation is the change of applied high-voltage pulses, i.e. amplitude and pulse

[a] R. Rataj, Prof. Dr. J. F. Kolb  
 Leibniz Institute for Plasma Science and Technology (INP),  
 Felix-Hausdorff-Str. 2, 17489 Greifswald, Germany  
 E-mail: raphael.rataj@inp-greifswald.de  
 juergen.kolb@inpgreifswald.de  
 Homepage: <https://www.inp-greifswald.de/>

[b] R. Rataj, Prof. Dr. J. F. Kolb  
 University of Rostock, Institute of Physics,  
 Albert-Einstein-Str. 23–24, 18059 Rostock, Germany

[c] M. Werneburg  
 University of Greifswald, Institute of Physics,  
 Felix-Hausdorff-Str. 6, 17489 Greifswald, Germany

[d] Dr. H. Below  
 Department of Restorative Dentistry, Periodontology, Endodontology,  
 Preventive and Pediatric Dentistry, Dental School of University,  
 Medicine Greifswald,  
 Walter-Rathenau-Str. 42, 17489, Greifswald, Germany

© 2023 The Authors. ChemPhysChem published by Wiley-VCH GmbH. This is an open access article under the terms of the Creative Commons Attribution Non-Commercial NoDerivs License, which permits use and distribution in any medium, provided the original work is properly cited, the use is non-commercial and no modifications or adaptations are made.

duration, with increasing water conductivity, especially for often studied Marx-type pulse generators.<sup>[18]</sup> In this case are pulse amplitudes and durations decreasing (for the same charging voltage), which corresponds to shorter discharge filaments and reduced times for the production of reactive species. Unfortunately, reports on the influence of liquid conductivity on the plasma chemistry separately from the pulsed power system are, so far, missing.

Moreover, previous studies suffer from a common methodology to apply several discharges to form rather high amounts of hydrogen peroxide.<sup>[16,17,25]</sup> Multiple discharges aid the averaged quantification but also introduce possible interactions between discharge events. For example, hydrogen peroxide that is formed in a discharge, is susceptible to cleavage by UV-light from the next discharge, which eventually leads to saturation.<sup>[21]</sup> Also, each discharge generates micro-bubbles in the vicinity of the needle electrode, which alter the streamer development during subsequent pulses.<sup>[26]</sup> Therefore, only a diagnostic sensitive enough to measure hydrogen peroxide concentrations from a single discharge event may reveal representative quantities.

In addition, chemical simulations of streamer discharges in water showed a decreasing H<sub>2</sub>O<sub>2</sub>-production with reduced discharge temperature and expansion (corresponding to a lower voltage and shorter pulse duration),<sup>[16,27]</sup> hence, supporting that the observed decreasing amount of peroxide amount is affected by pulse characteristics. Accordingly, a consequent correlation of the spatial expansion as well as the dissipated energy of a discharge with the hydrogen peroxide production is necessary for different water conductivities to unambiguously describe the generation of reactive species. In this work, the specific production of hydrogen peroxide of individual single discharges was determined for conductivities of 1 μS·cm<sup>-1</sup>, 140 μS·cm<sup>-1</sup> and 280 μS·cm<sup>-1</sup>. The experiments were specifically conducted for pulses with a duration of 100 ns, as previous investigations have shown for this case an optimal relation between H<sub>2</sub>O<sub>2</sub> concentration, discharge expansion and sample volume. Discharges instigated by longer pulses had reduced production rates and needed an increased sample volume to account for longer discharge filaments, which reduced the hydrogen peroxide concentration below an analyzable limit.<sup>[10]</sup> For a thorough determination of hydrogen peroxide production, electrical as well as optical characteristics of individual discharges were observed to derive pertinent discharge properties, e.g. streamer length and dissipated energy. Any influence of the conductivity or the pulse shape on the expanse of the discharge was considered separately. Additionally, the production efficiency was calculated. The comprehensive characterization also enabled a differentiation of propagation and reillumination energy, which gave an insight into energy transfer processes. Thus, a comparison with simulations was possible and the findings could be related to electrical models of the discharge development.

## Experimental Section

### Discharge generation and characterization

The setup for this study was already described in detail previously.<sup>[28]</sup> In short, a tungsten needle (99.95% purity, *Metall Maier*), sharpened to a tip radius of (35 ± 1) μm, was placed at a distance of (5.0 ± 0.2) mm above a titanium plate with a diameter of 46 mm (99.5% purity, *Selfan Fine + Metal GmbH*), which was integrated in the bottom of a polymethylmethacrylat chamber. The chamber had a volume of 1 mm<sup>3</sup> and was filled with 800 μl of conductive water. For this, KCl (96%, Carl Roth) was dissolved into deionized water to adjust the conductivity,  $\sigma$ , from 1 μS·cm<sup>-1</sup> to either 140 μS·cm<sup>-1</sup> or 280 μS·cm<sup>-1</sup>. The conductivities were selected with respect to a comparison of the dielectric time constant with time characteristics pertinent to the applied high-voltage pulses, i.e. pulse duration and fall time (see Discussion for details).

High-voltage pulses of positive polarity and a duration of (100 ± 2) ns (FWHM), a rise time of (19 ± 2) ns (defined by the change of voltage from 10% to 90% of the amplitude) and an amplitude of (55 ± 2) kV were generated with a custom build, stacked Blumlein line generator. A matching resistance of 250 Ω reduced pulse reflections and the influence of water conductivity on the applied pulses, i.e. amplitude and duration.

Voltage and current signals were monitored with two passive high-voltage probes (P6015A, *Tektronix*) and a Rogowski coil (CT-E2.5, *Magnelab*). Additionally, a photodetector (DET 10 A, *ThorLabs*) recorded the spatially-integrated emitted light intensity. All signals were recorded with an oscilloscope (WaveSurfer 10, *LeCroy*). An ICCD camera (4Picos, *Stanford Computer Optics*) took time-integrated images of the discharge development with a gate width of 200 ns.

### Hydrogen peroxide quantification

Hydrogen peroxide was quantified electrochemically. After an individual single discharge event, 720 μl of the treated solution were withdrawn, mixed with 80 μl concentrated buffer solution (134.04 g·l<sup>-1</sup> of KH<sub>2</sub>PO<sub>4</sub>, 2.67 g·l<sup>-1</sup> of Na<sub>2</sub>HPO<sub>4</sub> and 74.52 g·l<sup>-1</sup> of KCl dissolved in deionized water, *Carl Roth*) and stored in a refrigerator to suppress any reaction degrading H<sub>2</sub>O<sub>2</sub>. Afterwards, the hydrogen peroxide content of each sample was quantified with a potentiostat for flow injection analysis (FIA) (PGSTAT101, *Metrohm*) and a screen-printed electrode (DRP-710, *Metrohm*). The measurement potential was set to -0.1 V and the sampling rate to 0.05 s. Each electrode was calibrated with a serial dilution of a standard H<sub>2</sub>O<sub>2</sub> solution with concentrations of (0.25, 0.5, 0.75, 1, 2 and 4) μmol·l<sup>-1</sup>. To decrease the hydrogen peroxide detection limit, reference samples of untreated liquid, which were injected into the plasma chamber and removed after two minutes without applying a pulse, were analyzed in combination with the actual samples. Prior to and after the measurement of a sample, a 1 μmol·l<sup>-1</sup> hydrogen peroxide standard was recorded to ensure electrode stability. Accordingly, a detection limit of 0.05 μmol·l<sup>-1</sup> (three-times the noise amplitude) and a recovery rate of 98.4% (for a concentration of 1 μmol·l<sup>-1</sup>) were achieved.

## Results

### Discharge development depending on water conductivity

Typical temporal resolved measurements of voltage, current and light intensity are shown in Figure 1 for single discharges for all three investigated conductivities.

Voltage characteristics, as shown in Figure 1(A), did not change with water conductivities. This was enforced with a matching resistor and by adjusting the charging voltage of the Blumlein line. The peak pulse amplitude was achieved in 36 ns and dropped off at about 100 ns into the pulse. The times for

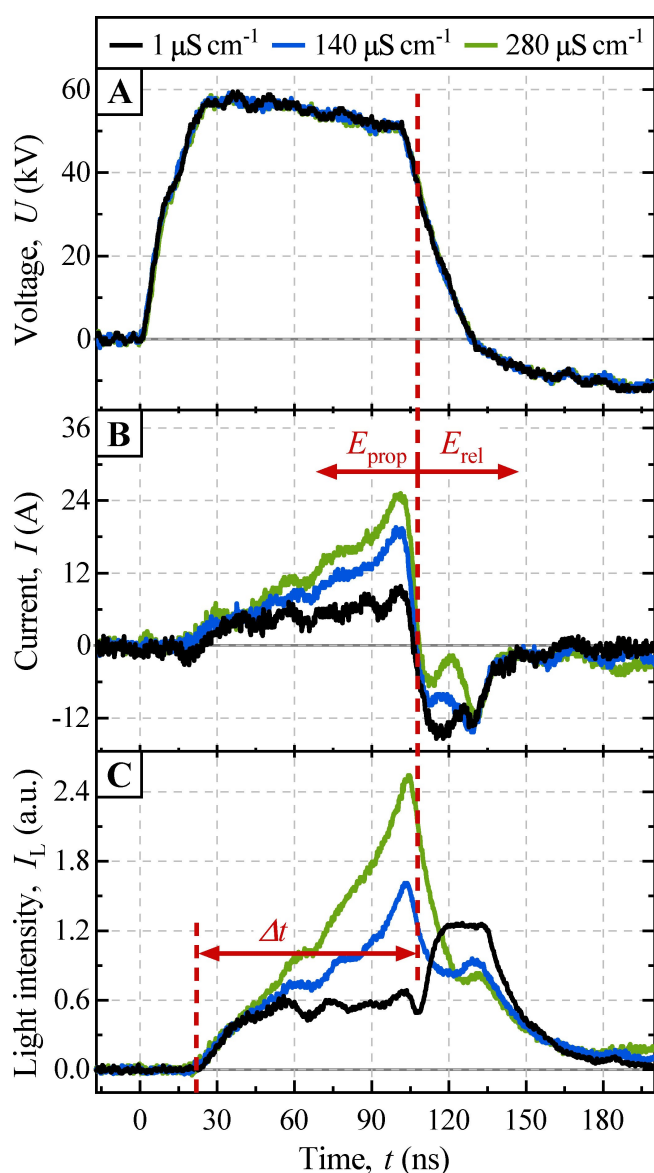


**Figure 1.** Voltages (A), discharge currents (B) and light intensities (C) for individual discharges ignited in water with different conductivities of  $1 \mu\text{S}\cdot\text{cm}^{-1}$  (black lines),  $140 \mu\text{S}\cdot\text{cm}^{-1}$  (blue lines) and  $280 \mu\text{S}\cdot\text{cm}^{-1}$  (green lines). Discharge propagation time,  $\Delta t$ , was defined as the time between first detectable light emission and current zero-crossing during the falling edge of the voltage pulse. Total electric energy dissipated in the discharge was divided into propagation energy,  $E_{\text{prop}}$ , and reillumination energy,  $E_{\text{rel}}$ .

voltage increase and decrease from 10% to 90% of the peak voltage were 19 ns and 20 ns, respectively.

Currents were strongly dependent on water conductivity, as illustrated in Figure 1(B). All current signals were corrected for events that did not result in a discharge for an applied pulse by subtracting respective reference measurements. Accordingly, no displacement or resistive current due to reactor capacitance or resistance is shown. After a statistical time lag, varying between 15 ns and 85 ns, currents began to rise linearly, perturbed by small fluctuations that were also present in the voltages. For the lowest conductivity of  $1 \mu\text{S}\cdot\text{cm}^{-1}$ , the increase in current was almost imperceptible, reaching about 6 A before the voltage dropped off. For higher conductivities, highest currents of 19 A and 24 A were observed, respectively. Currents reversed polarities, while decreasing voltages were still positive, and passed through a minimum before rising to zero again. This current minimum was associated with the reillumination of discharge filaments, which was described in detail previously.<sup>[28]</sup> Accordingly, propagation energy,  $E_{\text{prop}}$ , and reillumination energy,  $E_{\text{rel}}$ , were defined as the energy dissipated before and after the current signal changed polarity, respectively.

Light emissions closely followed the development of currents, as shown in Figure 1(C). Again, a background signal (without a discharge and an non-transparent screen blocking the photodetector) was subtracted from signals obtained for actual discharges. Light intensity increased slightly until the end of the voltage pulse. While the voltage decayed, a distinct maximum in light intensity – the reillumination – was correlated with the minimum in current before both signals ceased. Higher peak values for light emissions towards the end of discharge propagation were observed for higher conductivities, corresponding to higher currents, before the voltage dropped. The distinct reillumination peak that was observed for the lowest conductivity flattened out and shifted to times shortly after the reversal of voltage polarity. Additionally, as the time of current polarity inversion was unaffected by conductivity, the light intensity minimum seemed no longer to correspond to a ceasing propagation of discharge filaments. As unique feature of the development of individual discharges, the propagation time,  $\Delta t$ , of a discharge was, therefore, defined as the time between first light emission and the change in current polarity.

The spatial expansion and structure of a discharge were obtained from images exemplarily shown in Figure 2. The needle is located at the top while the counter electrode is set below, outside of the imaged area. Discharges appeared brightest near the tip of the high-voltage needle electrode. From there, filaments spread outwards in a half sphere beneath the needle with a tendency of longer filaments in the direction towards the counter electrode. With an increasing distance from the needle tip, channels branched into multiple paths. Despite an increasing emission intensity, no differences were observed in spatial structure for different conductivities.

End points for each filament were identified automatically by an image processing algorithm.<sup>[10]</sup> Based on those ends, the path of strongest light emission was traced back to the needle electrode and their individual length,  $L_{s,j}$ , was calculated, from

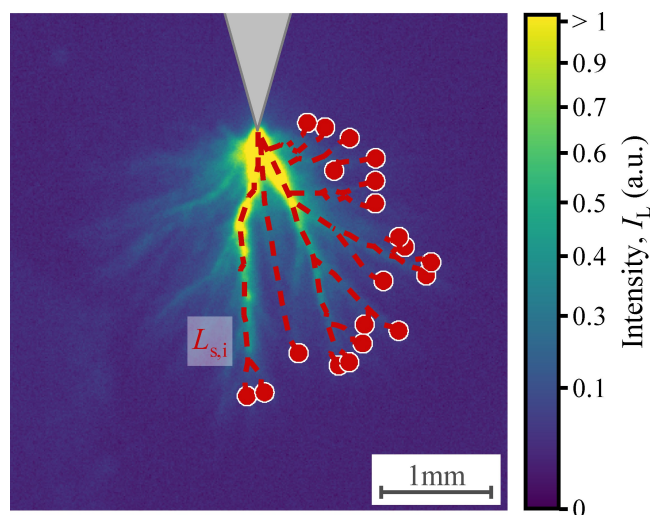


**Figure 2.** Time integrated image of a streamer discharge in deionized water ( $1 \mu\text{S}\cdot\text{cm}^{-1}$ ), which was recorded with a 200 ns-gate width. Intensities were normalized to the maximum possible pixel value (14 bit). An algorithm identified all discharge path endings in the right half of the image (red dots) and traced the filaments, originating at the needle electrode, to measure the individual filament length,  $L_{s,i}$ .

which a mean streamer length,  $L_s$ , for each discharge was derived.

#### Hydrogen peroxide production depending on water conductivity

Parameters for a comprehensive characterization of hydrogen peroxide production in single discharges are shown in Figure 3. Streamer length,  $L_s$ , propagation energy,  $E_{\text{prop}}$ , and reillumination energy,  $E_{\text{rel}}$ , are, therefore, displayed conjointly with the amount of produced  $\text{H}_2\text{O}_2$ ,  $n_{\text{H}_2\text{O}_2}$ , in relation to the individual propagation time,  $\Delta t$ , for all investigated water conductivities. Different propagation times were a result of the statistical time lag before discharge inception, while each discharge ended at a similar time (see Figure 1). Panel A of Figure 3 shows the amount of  $\text{H}_2\text{O}_2$ ,  $n_{\text{H}_2\text{O}_2}$ , produced in individual discharges. For deionized water with a conductivity of  $1 \mu\text{S}\cdot\text{cm}^{-1}$ , production of  $\text{H}_2\text{O}_2$  increased nonlinearly with longer propagation times. The eventually achieved highest amount of  $\text{H}_2\text{O}_2$  was  $(1.0 \pm 0.1) \text{ nmol}$  corresponding to a concentration of  $(43 \pm 4) \mu\text{g}\cdot\text{l}^{-1}$ . Overall, a higher conductivity did not have a significant influence on the amount of  $\text{H}_2\text{O}_2$  that was produced. Only slightly lower hydrogen peroxide contents of  $(0.8 \pm 0.1) \text{ nmol}$  and  $(0.6 \pm 0.1) \text{ nmol}$  were observed for water conductivities of  $140 \mu\text{S}\cdot\text{cm}^{-1}$  and  $280 \mu\text{S}\cdot\text{cm}^{-1}$ , respectively. If the mean amount of  $\text{H}_2\text{O}_2$  was calculated only for discharges that propagated more than 75 ns, quantities of  $(0.7 \pm 0.1) \text{ nmol}$ ,  $(0.7 \pm 0.1) \text{ nmol}$ , and  $(0.5 \pm 0.1) \text{ nmol}$  were obtained. Hence, the influence of different water conductivities seemed even less pronounced. Due to these rather small differences, all measured values of  $n_{\text{H}_2\text{O}_2}$  were used to  $\Delta t$  an empirical function, describing the  $\text{H}_2\text{O}_2$ -production with respect to propagation time. A linear,

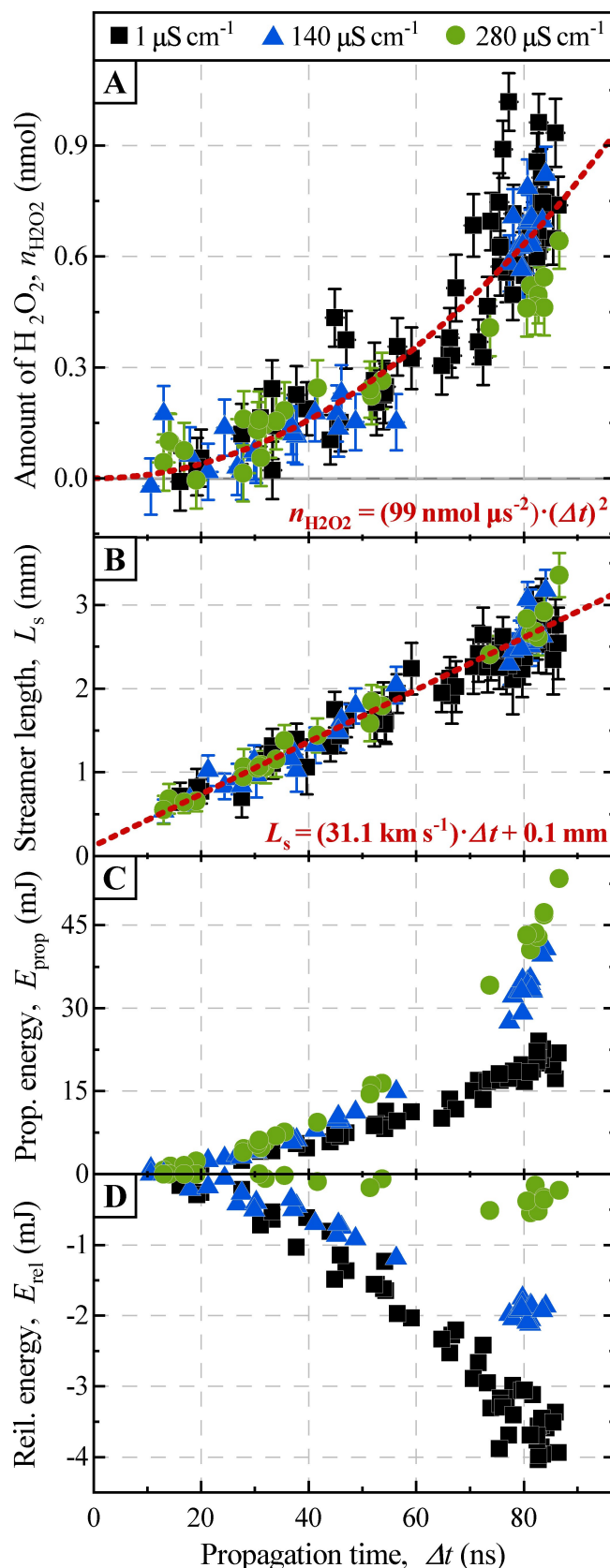


**Figure 3.** Amount of  $\text{H}_2\text{O}_2$  (A), streamer lengths (B), propagation energies (C) and reillumination energies (D) for different water conductivities of  $1 \mu\text{S}\cdot\text{cm}^{-1}$  (black squares),  $140 \mu\text{S}\cdot\text{cm}^{-1}$  (blue triangles) and  $280 \mu\text{S}\cdot\text{cm}^{-1}$  (green circles). The amount of hydrogen peroxide increased with propagation time, which can be described by a quadratic function (dashed line), while streamer lengths increased linearly.



a quadratic and an exponential model were fitted. The quadratic model yielded the best approximation with an R-value of 0.85 (A motivation of this model is given in the Discussion). The corresponding function for the molar amount of generated hydrogen peroxide was:

$$n_{\text{H}_2\text{O}_2} = (99 \text{ nmol} \cdot \mu\text{s}^{-2}) \cdot (\Delta t)^2. \quad (1)$$

Panel B of Figure 3 shows the dependency between mean streamer length,  $L_{sr}$ , and propagation time,  $\Delta t$ . Regardless of different conductivities, streamer lengths increased with longer propagation time, reaching lengths up to 3.4 mm. This was best described with a linear function. Accordingly, streamers propagated with a constant average velocity,  $v_s$ , of  $31.1 \text{ km} \cdot \text{s}^{-1}$ .

Dissipated energies were split into propagation energy,  $E_{\text{prop}}$ , and reillumination energy,  $E_{\text{rel}}$ , as presented in panels C and D of Figure 3, respectively. This separation was encouraged, since  $E_{\text{prop}}$  was dissipated during the expansion of the discharge, which draws power from the generator. Conversely,  $E_{\text{rel}}$  was associated with a self-driven ionization wave propagating through the already established discharge filaments to electrically neutralize their heads. Thus, energy that was stored at the heads of the filaments during the propagation process was utilized for reillumination which is why negative values have been assigned to  $E_{\text{rel}}$ .<sup>[28]</sup>

In general, propagation energies increased with propagation time. For the lowest conductivity, a maximum energy of 24 mJ was derived, which rose with conductivity to 43 mJ or 53 mJ. The reillumination energy also increased in absolute values with increasing propagation times with a maximum of 4 mJ for a water conductivity of  $1 \mu\text{S} \cdot \text{cm}^{-1}$ . However, the regained energy decreased to at most 2.1 mJ and 0.5 mJ for higher conductivities. The total dissipated energy was calculated from the sum of  $E_{\text{prop}}$  and  $E_{\text{rel}}$ . As the reillumination energy was recuperated once the discharge seized to expand any further, the entire, in the discharge dissipated energy was in fact smaller than indicated by  $E_{\text{prop}}$  alone. (Hence, the negative values associated with  $E_{\text{rel}}$ .) The actually dissipated energy during the development of a discharge increased with propagation time, as implicitly also did  $E_{\text{prop}}$  and  $E_{\text{rel}}$  in absolute values. For a given propagation time, the overall dissipated energy was smallest for the lowest liquid conductivity, as  $E_{\text{prop}}$  was minimal and the energy regained from reillumination was highest. With increasing liquid conductivity, propagation energies increased while reillumination energies were reduced, thus more electrical energy was dissipated in total.

Relating total energy dissipation, i.e. the sum of  $E_{\text{prop}}$  and  $E_{\text{rel}}$ , with the highest amount of produced hydrogen peroxide, production efficiencies of  $6.1 \text{ g} \cdot \text{kWh}^{-1}$ ,  $2.4 \text{ g} \cdot \text{kWh}^{-1}$  and  $1.4 \text{ g} \cdot \text{kWh}^{-1}$  were determined for conductivities of  $1 \mu\text{S} \cdot \text{cm}^{-1}$ ,  $140 \mu\text{S} \cdot \text{cm}^{-1}$  and  $280 \mu\text{S} \cdot \text{cm}^{-1}$ . Accordingly, production efficiencies dropped with rising conductivity due to a higher energy demand during propagation and a less pronounced reillumination, while the general production rate was the same.

## Discussion

The results revealed that water conductivity does not have a substantial effect on the production of hydrogen peroxide for discharges submerged in water (Figure 3). This has been validated for the application of 100 ns high-voltage pulses but conceivably also applies for other pulse durations. This important finding indicates that any improvement in  $\text{H}_2\text{O}_2$ -production, and on plasma-chemical reactions in general, requires an optimization of underlying discharge processes itself. This refers directly to respective operating parameters and discharge mechanisms. However, the generation of submerged discharges by high-voltage pulses has to take into account the electrical characteristics of the load, including in particular water conductivity. Therefore, considerable effort was put in the presented study on the compensation of the effect of water conductivities on the applied high-voltage pulses, i.e. possible changes in pulse durations and amplitudes. We assume that these might explain previous reports for a decreasing hydrogen peroxide production for an increase of conductivity.<sup>[18,20–22]</sup> Therefore, in the subsequent sections, first the necessary control of electrical operating parameters for discharges in liquids are described in more detail. On this basis, an unambiguous evaluation of hydrogen peroxide production for defined pulse parameters and corresponding discharge development is discussed, which could guide future studies on the actual effect of different plasma parameters.

### Control of electrical operating parameters with respect to liquid conductivity

Many systems for the instigation of discharges in liquid are based on the discharge of a capacitance, including Marx-type generators and pulse forming networks. In these (and other) cases is the applied pulse crucially dependent on the matching of the output impedance of the generator to the load. An increase in water conductivity reduces the load resistance, resulting in shorter pulse durations with lower amplitudes (for the same charging parameters of the system). While changes in amplitudes could be addressed by higher output settings (or charging voltages) are shorter pulse lengths an inherent feature of the experimental setup, which cannot be easily corrected at the pulse generator. In addition, a load-mismatch will give rise to reflections with various effects on instigated discharges, e.g. the possible reignition of discharges.<sup>[29,30]</sup> Lower pulse amplitudes could lead to lower temperatures inside a discharge filament or reduce the total number of channels resulting in a lower production rate of hydroxyl radicals.<sup>[10,16,27,31]</sup> Accordingly, the pulse duration indirectly influences the plasma chemistry, as the mean spatial expansion of a discharge and the associated period for plasma-chemical reactions to proceed. Thus, it defines the chemical active volume of a discharge as long as the discharge stopping length is not reached.<sup>[32]</sup> Consequently, the study of pulsed discharges in liquid has to consider pulse generation and discharge configuration together to define comparable conditions for the investigation of specific param-

ters. For the system investigated in this study, this allowed an unambiguous correlation of reaction chemistry with discharge characteristics, for instance to determine the actual influence of water conductivity.

### Advantage of a single discharge diagnostic for assessing hydrogen peroxide production

Commonly, experiments to determine  $\text{H}_2\text{O}_2$ -concentrations for discharges in water with respect to different water conductivities relied on an application of several thousand discharges.<sup>[4,9,16,20,21,25,31]</sup> This method has, however, the obvious disadvantage that the water conductivity has several indirect effects on the observed and averaged bulk  $\text{H}_2\text{O}_2$ -concentrations even if a dependency on operating pulse parameters was not the objective of these studies. For instance, higher conductivity leads to stronger emission of UV-radiation and increases the electrode erosion, resulting in higher concentrations of metal ions dissolved in the liquid. If multiple discharges are generated in a sample, both, ions and radiation, are able to dissociate  $\text{H}_2\text{O}_2$  that was previously formed.<sup>[4,9,19–21]</sup> On the contrary, a single discharge releases a negligible amount of metal ions, which could be quenched by adding a buffer solution to the sample after treatment.<sup>[20]</sup> Furthermore, the UV-emission of a single discharge cannot degrade any hydrogen peroxide, as simulations suggest that the peroxide is formed in the discharge mainly after the temperature of the plasma has sufficiently dropped. Therefore, the simultaneously strongly reduced UV-emission will have at most a marginal effect.<sup>[27]</sup> However, the main motivation for applying single discharges was the separation of effects of inherent liquid conductivity on the production of  $\text{H}_2\text{O}_2$ , i.e. plasma chemistry, from those resulting from the discharges itself and their development depending on parameters for applied high-voltage pulses, i.e. discharge physics. For example, the relation between streamer length and propagation time was not affected by conductivity (cf. Figure 3(B)). This corresponded to a hydrogen peroxide production of individual discharges, which was also independent from conductivity (cf. Figure 3(A)). This suggests that as long as the discharge volume was the same for similar propagation times, hydrogen peroxide concentrations were the same and liquid conductivity had no influence on the production. On average however, the streamer length is decreasing due to generally shorter propagation times, which is primarily an effect of an increasing statistical time lag as a consequence of higher conductivity. This effect of averaging seems to explain previous reported results on reduced  $\text{H}_2\text{O}_2$ -production for increasing conductivity.<sup>[21,27]</sup>

### Hydrogen peroxide production in a single discharge

Simulations and experimental studies of discharges in water indicate that  $\text{H}_2\text{O}_2$ -concentration is closely dependent on the generation of hydroxyl radicals ( $\cdot\text{OH}$ ) according to the following reactions by the aid of an additional reaction partner (M).<sup>[9,27,31]</sup>



Rate constants for reaction 2 and 3 are  $k_1 = 5.8 \cdot 10^{-9} \cdot \exp(-440 \text{ kJ}/RT)$  and  $k_2 = 1.51 \cdot 10^{-11} \cdot (T/298 \text{ K})^{-0.37}$ , respectively (both in units of  $\text{cm}^3 \cdot \text{molecule}^{-1} \cdot \text{s}^{-1}$ ). The generation of  $\cdot\text{OH}$  is only dependent on temperature and overall volume of the plasma channel. As described, these parameters are determined by the spatial expansion of a discharge, i.e. streamer length,  $L_s$ , and the energy dissipated during the propagation,  $E_{\text{prop}}$  which is conceivably depending on water conductivity.<sup>[27]</sup> Hydrogen peroxide is then produced from  $\cdot\text{OH}$  after discharge channels have cooled down.<sup>[16,27]</sup>

In simulations,  $\cdot\text{OH}$  production in streamer discharges is commonly calculated in one dimension along the filament radius assuming a homogeneous production in the direction of filament propagation.<sup>[16,27]</sup> For simplification, a single substitute streamer can summarily describe the entire discharge.<sup>[10,28]</sup> The production of hydroxyl radicals can then be calculated by the integration of local  $\cdot\text{OH}$  concentrations over the streamer volume. It can be assumed that the overall  $\cdot\text{OH}$ -production rate,  $k_1$ , in a streamer is constant as long as the temperature along the filaments of a streamer remains the same. Thus, the amount of hydroxyl radicals,  $n_{\text{OH}}$ , that is produced equals:

$$\begin{aligned} n_{\text{OH}} &= \int_0^{\Delta t} \int_0^{L_s} \int_0^{A_s} k_1 dAdLdt \\ &= k_1 A_s v_s \int_0^{\Delta t} dt \\ &= k_1 A_s v_s (\Delta t)^2, \end{aligned} \quad (4)$$

where  $L_s$  indicates the streamer length,  $A_s$  the streamer cross-sectional area,  $v_s$  the propagation velocity and  $\Delta t$  the propagation time. Streamer length was directly proportional to the propagation time (cf. Figure 3(B)). Hence, the propagation time could be substituted by the constant propagation velocity as shown in Figure 3(B). In addition, changes in streamer cross section,  $A_s$ , were assumed to be insignificant.<sup>[27]</sup> Defining an empirical proportionality factor  $c_{\text{OH} \rightarrow \text{H}_2\text{O}_2}$ , which describes the conversion of  $\cdot\text{OH}$  to  $\text{H}_2\text{O}_2$ , Eq. (5) then relates to the produced amount of hydrogen peroxide:

$$\begin{aligned} n_{\text{H}_2\text{O}_2} &= c_{\text{OH} \rightarrow \text{H}_2\text{O}_2} \cdot k_1 \cdot A_s \cdot v_s \cdot (\Delta t)^2 \\ &= k_{\text{H}_2\text{O}_2} \cdot A_s \cdot v_s \cdot (\Delta t)^2 \end{aligned} \quad (5)$$

Eq. (5) was fitted to the obtained  $\text{H}_2\text{O}_2$  data with good agreement (cf. Figure 3(A)). Accordingly, an average production rate,  $k_{\text{H}_2\text{O}_2}$ , of  $(3.2 \cdot A_s^{-1}) \text{ mol} \cdot \text{m}^{-1} \cdot \text{s}^{-1}$  could be derived for a propagation velocity,  $v_s$ , of  $31.1 \text{ km} \cdot \text{s}^{-1}$  as well as the fitting parameter of  $99 \text{ nmol} \cdot \mu\text{s}^{-2}$  (Eq. (1)). The rather basic model for the relevant discharge chemistry with respect to spatial and temporal expansion of a discharge seems sufficient to explain the results.

## Hydrogen peroxide production for an increasing energy dissipation due to water conductivity

According to literature, a higher water conductivity results in a higher power density in a discharge channel.<sup>[20,25,31,33]</sup> This should elevate the channel temperature and, hence, effect the hydroxyl and hydrogen peroxide production rates,  $k_1$  and  $k_2$ .<sup>[31,33]</sup> Therefore, a higher energy dissipation in a discharge for a higher conductivity was expected to correspond to a higher  $\text{H}_2\text{O}_2$ -production. An actual increasing propagation energy,  $E_{\text{prop}}$  was indeed observed at elevated conductivities (Figure 3(B)) while streamer lengths did not change (Figure 3(C)). If this energy would be completely transformed into heat, the channel temperature would be by a factor of 2.2 higher for a water conductivity of  $280\ \mu\text{S}\cdot\text{cm}^{-1}$  in comparison to deionized water. Obviously, the entire electrical energy is not exclusively transformed into heat in a discharge.<sup>[31]</sup> A substantial share was stored in the streamer head, as described by the reillumination energy,  $E_{\text{rel}}$ . Some of the electrical energy was dissipated in the electrode gap outside the plasma channel as well, e.g. due to Joule heating of the liquid. In fact, investigations on nano-second pulsed discharges in gas bubbles submerged in water have shown that the increasing energy dissipation was related only to an increased current flowing in the bulk liquid.<sup>[34]</sup> Plasma properties, i.e. electron density, gas temperature and plasma volume, were not significantly changed. Therefore, energy dissipation has to be discussed in terms of water conductivity and hydrogen peroxide production separately for the discharge itself and the surrounding liquid.

An expedient parameter to describe the electrical response of a liquid for the application of a high-voltage pulse is the dielectric time constant  $\tau = \epsilon\epsilon_0 \cdot \sigma^{-1}$ , which is primarily determined by changes of the conductivity,  $\sigma$ , while the permittivity of water,  $\epsilon\epsilon_0$ , can practically not change. The response of the medium to an electrical event is dominantly resistive if the duration of the event is much longer than  $\tau$  and, conversely, better described by capacitive, i.e. charging, phenomena, when much shorter than the dielectric time constant. Hence, the constant is a parameter describing, if a lossy dielectric, i.e. a water load, acts as a resistance or a capacitance for the duration of an applied high-voltage pulse. Both have significantly different implications for the development of a discharge channel.

For a conductivity of  $1\ \mu\text{S}\cdot\text{cm}^{-1}$ ,  $\tau$  equals 7080 ns, which means that the electrical response of water was determined by its capacitive characteristic. In this case, resistive losses were negligible for the application of high-voltage pulses that were much shorter than  $\tau$ , e.g. a pulse duration of 100 ns. With increasing conductivities, i.e.  $140\ \mu\text{S}\cdot\text{cm}^{-1}$  and  $280\ \mu\text{S}\cdot\text{cm}^{-1}$ ,  $\tau$  decreased significantly to 50 ns and 25 ns, respectively. Accordingly, the water resembled a resistor for the short duration of the discharge events. Less of the provided energy could be stored in the streamer for the propagation in the conductive medium and a higher share was transferred through the channel envelope into the surrounding water.

The reillumination energy,  $E_{\text{rel}}$ , is a measure for the electrical energy that is stored in the streamer and corresponds to the charge accumulated at the streamer head.<sup>[28,35]</sup> In deionized

water, up to 4 mJ were stored this way, i.e. about 17% of  $E_{\text{prop}}$  (cf. Figure 3(C) and (D)). On the contrary, for water acting predominantly as resistive medium, i.e. for the highest conductivity and the smallest dielectric time constant, only about 1% (0.5 mJ) of the energy was retrieved during reillumination.

Corresponding to greater losses in the liquid surrounding, the discharge had a higher propagation energy,  $E_{\text{prop}}$ , for higher conductivities (Figure 3(C)). The losses themselves were not only dependent on liquid conductivity but on the surface of the boundary between streamer and water and on the distance between streamer and the counter electrode. Both determined the actual conductive pathway and both were related to streamer length,  $L_s$ . No significant effect of conductivity on  $E_{\text{prop}}$  was observed for short propagation times. In this case were streamer lengths small ( $< 1\ \text{mm}$ ) and the ground electrode was far away. Accordingly, losses were small. For an extended propagation, some filaments crossed up to 70% of the interelectrode gap and strong branching increased the boundary between plasma and liquid. Consequently, losses became more substantial.

The higher propagation energy that was observed for higher water conductivities (cf. Figure 3(C)) was apparently primarily dissipated by corresponding losses in the surrounding medium. Reillumination energies, as a measure for energy stored in the streamer heads, decreased with higher conductivity, which also indicated higher losses in the liquid surrounding of the discharge (cf. Figure 3(D)). Neither discharge structures (cf. Figure 2), nor discharge development and in particular streamer lengths (cf. Figure 3(B)) were depending on conductivity, i.e. changing for higher propagation energies. In addition, hydrogen peroxide concentrations (cf. Figure 3(A)) were not affected by different conductivities. Accordingly, also temperatures in the streamer could not sufficiently have increased to result in a higher rate constant,  $k_1$  for the production of hydroxyl radicals and hydrogen peroxide (cf. Eqs. (2) and (3)). As a result,  $\text{H}_2\text{O}_2$ -production only depended on the spatial expansion of the discharge and was not affected by an increasing conductivity although production efficiencies decreased.

## Conclusions

The production of hydrogen peroxide was investigated for single discharges that were instigated directly in water of different conductivities with high-voltage pulses of 100 ns and 55 kV in amplitude. The amount of hydrogen peroxide was quadratically dependent on the discharge propagation time but independent from liquid conductivity. As a result, an independent rate of  $(3.2 \cdot A_s^{-1})\ \text{mol}\cdot\text{m}^{-1}\cdot\text{s}^{-1}$  was found for the hydrogen peroxide production. The result can be explained by an increasingly resistive behavior of the water surrounding the discharges for higher liquid conductivities, which could be described by the dielectric time constant. This quantitative description for the hydrogen peroxide and hydroxyl production was presented based on readily observable parameters of the discharge development. With respect to the likely underlying

mechanisms, the findings contribute to a better understanding of discharges chemistry for submerged discharges, e.g. the production of other species like  $\cdot\text{O}$ ,  $\cdot\text{HO}_2$ , and respectively developed simulations may be compared with the presented data.

With respect to application of discharges in water as an advanced oxidation process and an optimization of the production of chemical species, and in particular hydrogen peroxide, the results suggest that the energy efficiency should be improved for conductive liquids primarily by discharges that are operated on shorter time scales than determined by the dielectric time constant. This approach might benefit the competitiveness of the method against other advanced oxidation processes.

## Funding

This research did not receive any specific grant from funding agencies in the public, commercial, or not-for-profit sectors.

## Acknowledgements

The authors appreciate the research structure and the supportive background of the Leibniz Institute for Plasma Science and Technology (INP). Special thanks are given to Hans Höft for constructive discussions on experiments and data analysis. Open Access funding enabled and organized by Projekt DEAL.

## Conflict of Interests

The authors declare that they have no known competing financial interests or personal relationships that could have appeared to influence the work reported in this paper.

## Data Availability Statement

The data that support the findings of this study are available from the corresponding author upon reasonable request.

**Keywords:** advanced oxidation process · plasma chemistry · plasma in liquids · pulsed power · water chemistry

- [1] B. Locke, M. Sato, P. Sunka, M. Hoffmann, J.-S. Chang, *Ind. Eng. Chem. Res.* **2006**, *45*, 882.  
 [2] J. Kolb, R. Joshi, S. Xiao, K. Schoenbach, *J. Phys. D* **2008**, *41*, 234007.  
 [3] J. Foster, *Phys. Plasmas* **2017**, *24*, 055501.

- [4] R. Banaschik, P. Lukes, C. Miron, R. Banaschik, A. Pipa, K. Fricke, P. Bednarski, J. Kolb, *Electrochim. Acta* **2017**, *245*, 539.  
 [5] R. Banaschik, H. Jablonowski, P. Bednarski, J. Kolb, *J. Hazard. Mater.* **2018**, *342*, 651.  
 [6] M. Schneider, R. Rataj, J. Kolb, L. Bláha, *Environ. Pollut.* **2020**, *266*, 115423.  
 [7] M. Schneider, R. Rataj, L. Bláha, J. Kolb, *Chem. Eng. J.* **2022**, *451*, 138984.  
 [8] P. Attri, Y. Kim, D. Park, Y. Park, Y. Hong, H. Uhm, K.-N. Kim, A. Fridman, E. Choi, *Sci. Rep.* **2015**, *5*, 1.  
 [9] S. Thagard, K. Takashima, A. Mizuno, *Plasma Chem. Plasma Process.* **2009**, *29*, 455.  
 [10] R. Rataj, M. Werneburg, H. Below, J. Kolb, *Plasma Sources Sci. Technol.* **2022**, *31*, 105005.  
 [11] A. Joshi, B. Locke, P. Arce, W. C. Finney, *J. Hazard. Mater.* **1995**, *41*, 3.  
 [12] P. Lukeš, A. Appleton, B. Locke, *IEEE Trans. Ind. Appl.* **2004**, *40*, 60.  
 [13] S. Yang, L. Zhang, F. Cui, J. Ma, *Production of Hydrogen Peroxide by Pulsed High Voltage Discharge in Water*, in 2009 3rd international conference on bioinformatics and biomedical engineering, IEEE 2009 pages 1–4.  
 [14] S. Li, S. Hu, H. Zhang, *IEEE Trans. Plasma Sci.* **2011**, *40*, 63.  
 [15] J. Wen, Y. Li, M. Zhang, G. Zhang, *Effects of Discharge Patterns and Pulse Width on Hydrogen Peroxide Formation by Pulsed Electrical Discharge in Water*, in 2019 IEEE 20th International Conference on Dielectric Liquids (ICDL), IEEE 2019 pages 1–4.  
 [16] L. Chauvet, C. Nenbangkaeo, K. Grosse, A. von Keudell, *Plasma Processes Polym.* **2020**, *17*, 1900192.  
 [17] T. Nguyen, C. Rond, A. Vega, X. Duten, S. Forget, *Plasma Chem. Plasma Process.* **2020**.  
 [18] R. Banaschik, F. Koch, J. Kolb, K.-D. Weltmann, *IEEE Trans. Plasma Sci.* **2014**, *42*, 2736.  
 [19] S. Mededovic, B. Locke, *Appl. Catal. B* **2006**, *67*, 149.  
 [20] P. Lukeš, M. Clupek, V. Babicky, I. Sisrova, V. Janda, *Plasma Sources Sci. Technol.* **2011**, *20*, 034011.  
 [21] P. Lukeš, M. Clupek, V. Babicky, P. Sunka, *Plasma Sources Sci. Technol.* **2008**, *17*, 024012.  
 [22] A. Sugiarto, T. Ohshima, *Active species formation of pulsed plasma in water with ring-to-cylinder reactor type electrode*, in 2015 International Conference on Automation, Cognitive Science, Optics, Micro Electro-Mechanical System, and Information Technology (ICA-COMIT), IEEE 2015 pages 176–180.  
 [23] T. Dang, A. Denat, O. Lesaint, G. Teissedre, *Plasma Sources Sci. Technol.* **2008**, *17*, 024013.  
 [24] M. Sato, T. Ohgijama, J. Clements, *IEEE Trans. Ind. Appl.* **1996**, *32*, 106.  
 [25] B. Locke, K.-Y. Shih, *Plasma Sources Sci. Technol.* **2011**, *20*, 034006.  
 [26] P. Hoffer, P. Bilek, V. Prukner, Z. Bonaventura, M. Šimek, *Plasma Sources Sci. Technol.* **2022**, *31*, 015005.  
 [27] S. Medodovic, B. Locke, *J. Phys. D* **2009**, *42*, 049801.  
 [28] R. Rataj, H. Höft, J. Kolb, *Plasma Sources Sci. Technol.* **2019**, *28*, 125002.  
 [29] I. Marinov, S. Starikovskaia, A. Rousseau, *J. Phys. D* **2014**, *47*, 224017.  
 [30] K. Grosse, J. Held, M. Kai, A. von Keudell, *Plasma Sources Sci. Technol.* **2019**, *28*, 085003.  
 [31] B. Locke, S. Thagard, *Plasma Chem. Plasma Process.* **2012**, *32*, 875.  
 [32] P. Ceccato, O. Guaitella, M. Le Gloahec, A. Rousseau, *J. Phys. D* **2010**, *43*, 175202.  
 [33] R. Joshi, S. Thagard, *Plasma Chem. Plasma Process.* **2013**, *33*, 17.  
 [34] H. Wang, R. Wandell, K. Tachibana, J. Voráč, B. Locke, *J. Phys. D* **2019**, *52*, 075201.  
 [35] K. Grosse, V. Schulz von der Gathen, A. von Keudell, *Plasma Sources Sci. Technol.* **2020**, *29*, 095008.

Manuscript received: February 23, 2023

Revised manuscript received: July 4, 2023

Accepted manuscript online: July 10, 2023

Version of record online: ■■, ■■



# Publications and Conference Contributions

## Publications in Peer Reviewed Journals

---

Rataj, R., Höft, H., and Kolb, J. F.: Reillumination of submicrosecond pulsed corona-like discharges in water, *Plasma Sources Science and Technology*, 28.12, 2019

Schneider, M., Rataj, R., Kolb, J. F., and Bláha, L.: Cylindrospermopsin is Effectively Degraded in Water by Pulsed Corona-like and Dielectric Barrier Discharges, *Environmental Pollution*, 266, 2020

Zocher, K., Rataj, R., Steuer, A., Weltmann, K. D., and Kolb, J. F.: Mechanism of Microalgae Disintegration by Spark Discharge Treatment for Compound Extraction, *Journal of Physics D: Applied Physics*, 53.2, 2020

Sommer, M.-C., Balazinski, M., Rataj, R., Wenske, S., Kolb, J. F., and Zocher, K.: Assessment of Phycocyanin Extraction from *Cyanidium Caldarium* by Spark Discharges, Compared to Freeze-thaw Cycles, Sonication, and Pulsed Electric Fields, *Microorganisms*, 9.7, 2021

Schneider, M., Rataj, R., Bláha, L., and Kolb, J. F.: Experimental Review of Different Plasma Technologies for the Degradation of Cylindrospermopsin as Model Water Pollutant, *Chemical Engineering Journal*, 451.4, 2022

Rataj, R., Werneburg, M., Below, H., and Kolb, J. F.: Hydrogen Peroxide Production of Underwater Nanosecond-pulsed Streamer Discharges with Respect to Pulse Parameters and Associated Discharge Characteristics, *Plasma Sources Science and Technology*, 31.10, 2022

Rataj, R., Werneburg, M., Below, H., and Kolb, J. F.: Hydrogen Peroxide Production of Individual Nanosecond Pulsed Discharges Submerged in Water of Elevated Conductivity, accepted by *ChemPhysChem*, 2023. <https://doi.org/10.1002/cphc.202300143>

## Contributions to Conferences

---

Rataj, R.\* , Schulz, T., and Kolb, J. F.: Inception and Propagation of Pulsed Corona-like Discharges in Water, oral presentation, *82. Jahrestagung der DPG und DPG-Frühjahrstagung* in Erlangen, Germany, 2018

Zocher, K.\* , Rataj, R., Lackmann, J.-W. and Kolb, J. F.: Cell Wall Rupture of Microalgae for the Extraction of Metabolites by Applying Spark Discharges - Effects and Mechanism, oral presentation, *15th International Bioelectrics Symposium (BIOELECTRICS 2018)* in Prague, Czech Republic, 2018

Kolb, J. F.\* , Kredl, J., Schulz, T., Rataj, R., Hahn, V., Schmidt, M. and Weltmann, K.-D.: Pulsed Discharges in and close to Water for Degradation of Microbiological and Chemical Contaminants, oral presentation, *45th IEEE International Conference on Plasma Science (ICOPS 2018)* in Denver, USA, 2018

Rataj, R.\* , Höft, H., and Kolb, J. F.: Channel Reillumination in Pulsed Corona-like Discharges in Water, oral presentation, *83. Jahrestagung der DPG und DPG-Frühjahrstagung* in München, Germany, 2019

Rataj, R.\* , Höft, H., and Kolb, J. F.: Inception Voltage for Corona-like Discharges Generated with 100-ns High Voltage Pulses in Water Depending on Pulse Shape and Water Conductivity, oral presentation, *2019 IEEE Pulsed Power and Plasma Science Conference* in Orlando, USA, 2019

Rataj, R.\* , Höft, H., and Kolb, J. F.: Reillumination of Expiring Corona-like Pulsed Discharges in Water, poster presentation, *2019 IEEE Pulsed Power and Plasma Science Conference* in Orlando, USA, 2019

Schneider, M.\* , Rataj, R., Kolb, J. F. and Bláha, L.: Degradation of Cyndrospermopsin using Advanced Non-Thermal Plasma Technologies, oral presentation, *16th International Conference on Environmental Science and Technology* in Rhodes, Greece, 2019

Schneider, M.\* , Rataj, R., Kolb, J. F. and Bláha, L.: Degradation of Cyndrospermopsin using Advanced Non-Thermal Plasma Technologies, oral presentation, *11th International Conference on Toxic Cyanobacteria* in Kraków, Poland, 2019

Zocher, K.\* , Rataj, R., Steuer, A. and Kolb, J. F.: Spark Discharges as Tool for the Extraction of Microalgal Compounds, oral presentation, *83. Jahrestagung der DPG und DPG-Frühjahrstagung* in München, Germany, 2019

Zocher, K.\* , Rataj, R., Steuer, A. and Kolb, J. F.: Microalgal Protein and Cell Damage Analyses after Spark Discharge Treatment for Downstreaming Purposes, oral presentation, *3rd World Congress on Electroporation & Pulsed Electric Fields in Biology, Medicine, Food and Technology* in Toulouse, France, 2019

Zocher, K.\* , Rataj, R., Steuer, A. and Kolb, J. F.: Downstreaming of Valuable Compounds from Microalgae with Spark Discharges, Instigated by 100-ns High Voltage Pulses, oral presentation, *2019 IEEE Pulsed Power and Plasma Science Conference* in Orlando, USA, 2019

Kolb, J. F.\* , Rataj, R., Schulz, T., Barthel, N., Banaschik, R., Zocher, K., Schneider, M. and Bláha, L.: Cold Plasma - A New Technology for Water Cleaning, oral presentation, *NaToxAq Shareholder Meeting* in Barcelona, Spain, 2019

Schneider, M.\* , Rataj, R., Kolb, J. F. and Bláha, L.: Degradation of a Cyanobacterial Toxin by Non-thermal Plasmas, poster presentation, *NaToxAq Conference* in Brno, Czech Republic, 2020

Schmidt, M.\* , Hahn, V., Rataj, R., Hoffmann, U., Skowski, H. and von Woedtke, Th.: Non-thermal Plasma for Generation of Antimicrobial Aerosol, oral presentation, *9th Central European Symposium on Plasma Chemistry (CESPC9) + COST Action CA19110 Plasma Applications for Smart and Sustainable Agriculture (PLAgri)* in Vysoké Tatry, Slovakia, 2022

Schmidt, M.\* , Bansemer, R. and Rataj, R.: Power Measurement in an Inductively Coupled Pin-To-Liquid Discharge, poster presentation, *20th Plasma Technology Conference (PT20)* in Bochum, Germany, 2023

Kolb, J. F.\* , Brüser, V., Mousazadeh Borghei, S., Hahn, V., Schneider, M., Rataj, R. and Weltmann, K.-D.: Chemical Transformation by Atmospheric Pressure Discharges in Air with the Addition of Water, oral presentation, *23. International Conference on Gas Discharges and their Applications (GD 2023)* in Greifswald, Germany, 2023

\*presenter



# Appendix

## A1 Precision sharpening of tungsten needles

In a needle-to-plate arrangement for igniting discharges in water, the radius of curvature of the needle determines the electric field in the immediate vicinity of the tip and thus the ignition conditions of the discharge. Therefore, in order to ensure the most reproducible conditions possible for the generation of the discharges, a method was developed for sharpening the needle tip and for checking the sharpening result.

Brady *et al.*<sup>1</sup> published a procedure for the electrochemical sharpening of tungsten wires for the dissection of animal specimens. Here, this process was automated and the repeatability was improved by a mechanical apparatus. The apparatus is shown schematically in Figure A1.1.

The needle is placed above a graphite plate in a container filled with a 10% NaOH solution. The needle and plate are connected to a DC power supply that generates a current of approx. 2 A, which is responsible for the electrochemical removal of the material at the tip of the needle. The needle is clamped in an eccentric shaft via which a motor is used to generate a lifting motion of the needle tip. The filling level of the NaOH solution is adjusted so

<sup>1</sup>J. Brady. *Bulletin of the World Health Organization*, 32(1):143–144, 1965.

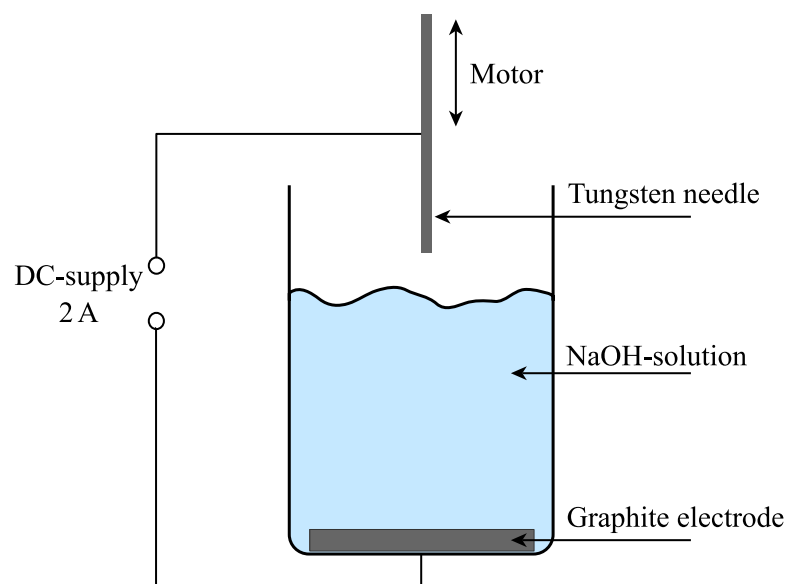
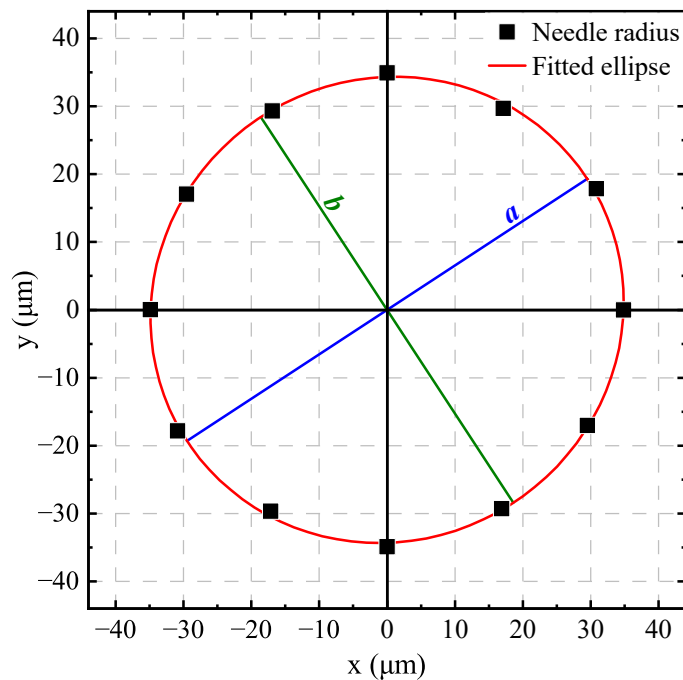


Abbildung A1.1: Scheme of the apparatus to sharpen tungsten needles.



**Abbildung A1.2:** Typical ellipse that was fitted to the needle radii. The width,  $a$ , on the semi-major axis (blue) and the height,  $b$ , on the semi-minor axis (green) are indicated.

that the needle is immersed 5 mm in the liquid at the lowest point of the stroke movement. The immersion frequency can be set via the power supply of the motor, and the frequency determines the shape of the needle.

After sharpening the needle, the radius of curvature was determined microscopically. Since the tip of the needle was not necessarily radially symmetric, it was imaged as a shadow image from six angles. For that, the needle was rotated by  $30^\circ$  along the needle axis between exposures, thus imaging the needle in a range of  $180^\circ$ . In each image, the contour of the needle shadow was determined and corrected for tilt with respect to the needle axis so that the tip of the needle was the lowest point of the contour. The points of the contour were fitted with a 14th degree axisymmetric polynomial and the curvature of the polynomial was determined at the minimum, i.e. the tip of the needle. The curvature radius was determined from the curvature of the polynomial. Since the radii of curvature of the different angles of view covered a range of  $180^\circ$  and an axis symmetry could be assumed due to the shadow image, an ellipse was fitted to the radii of curvature. A typical fitting result can be seen in Figure A1.2. The width,  $a$ , and the height,  $b$ , of the ellipse as well as its eccentricity were determined. The average of the height and width was defined as the radius of curvature of the needle tip, which was further characterized by the eccentricity.

## A2 Determine streamer lengths from ICCD images and 2D mapping error

The description of the algorithm to determine the length of all filaments that were generated by a single discharge is reprinted from the supplemental information of Article 2. It consists of a frame, where parameters as well as file-locations are initialized and images are loaded for the analysis one after the other. In this loop, a sub-routine is called for the actual analysis of each image. Frame and sub-routine are illustrated in the flow chart shown in Figure A2.3. The entire algorithm is shown for presentation in four columns with the continuous flow described by the interconnections A, B, C, and D. A describes, in particular, the loop for the analysis of individual images in the frame.

In detail, a reference image was loaded (first column), which was a record of the brightly illuminated discharge chamber showing the needle and counter electrode (but without discharge). The location of the needle tip, the direction of the needle axis and, optionally, an area of interest for the presumed propagation of the discharge were manually determined. The dimension of an image-pixel was characterized by the distance between reference

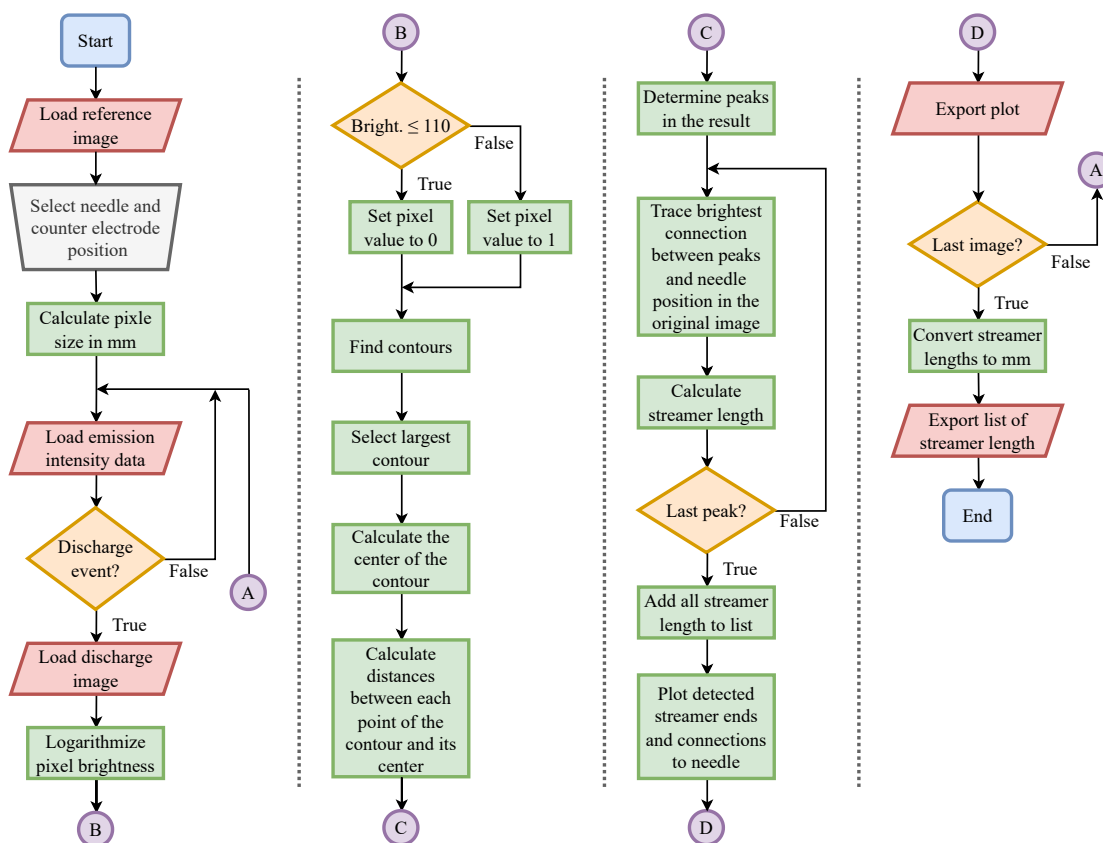


**Abbildung A2.3:** Flowchart of the algorithm to determine the streamer length  $L_{s,i}$ . Reprinted from the supplemental information of Article 2.

points. As the ICCD camera was triggered for every applied high-voltage pulse, regardless of a discharge ignition, a list containing light emission data for each pulse was loaded, from which an index array was generated. This index array contained an identifier that specified which pulses initiated a discharge. In the following main analysis-loop (interconnection ④ in Figure A2.3), images that were showing a discharge were loaded according to the index array. The intensity of each image was logarithmized to increase the contrast.

Next (second column), every pixel with an intensity of more than 110 was set to a value of one, while every other pixel value was set to zero. Within this binary image, contours were identified, the largest selected, and the center of this contour detected. The distance between each point on the contour and the center of the contour was calculated.

The distance information was then used for an automatic peak-search (third column), by which the points on the contour with the locally maximal distance to the center of the contour were determined. The identified peaks, hence, corresponded to the position of filament endings. The position of each filament ending was used to trace a path for the discharge channel within the original image, which connected the individual filament ending with the needle tip. This was done incrementally. Starting at the filament ending, the intensities of the surrounding pixel were evaluated. The pixel with the highest intensity was added to the path of the filament and used as the central pixel for the next iteration. If two or more surrounding pixel had the same intensity, the one closer to the needle electrode was selected. After the filament was traced entirely, the length,  $L_{s,i}$ , was calculated and stored in a list. After every filament of a discharge was traced, the average length and the maximum length were calculated, associated with the electrical and optical data, i.e. propagation time, pulse amplitude, light emission intensity and dissipated energy, and stored in a second list. For quality control, an image was plotted to show the discharge with all determined filament endings and paths and, optionally, stored.

Finally (fourth column), the main analysis-loop ended after all images were analyzed. Filament lengths in both lists were converted from pixel to millimeter. Those lists containing lengths and optical as well as electrical data for every discharge were stored. Then, the program was terminated.

The streamer lengths determined by the algorithm are inherently subject to error because the filaments spread out spatially and depth information relative to the focal plane of the camera is lost during imaging. This error can be estimated by assuming that the filaments are all of equal length and that their ends are uniformly distributed on a hemisphere of radius,  $R$ , whose origin is at the tip of the needle. Both assumptions are plausible since the filaments propagate at a constant velocity and their ends describe a semicircle in images (cf. Figure 2.3) with no apparent directional preference at least for 100 ns pulses (cf. Figure 2.4). Such a hemisphere can be seen in Figure A2.4.

To estimate the mapping error in determining the filament length, all points on the hemisphere surface

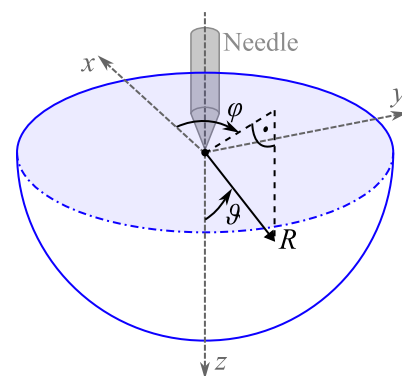


Abbildung A2.4: Sketch of the geometry used to estimate the aberration when determining the filament length.



are mapped to a plane which contains the location of the needle tip and is perpendicular to the top surface of the hemisphere. The average distance,  $\bar{R}'$ , between the needle tip and the projection points then corresponds to the average length for filaments observed in the images, which actually have a length of  $R$ .

Without limiting generality, the center of the hemisphere is placed at the coordinate origin so that its flat surface is in the  $x$ - $y$ -plane of the coordinate system. The surface points of the hemisphere are projected onto the  $y$ - $z$ -plane. The projection length,  $R'$ , i.e. the distance between the origin and the projection of any point of the hemisphere surface, is given by the following equation:

$$R' = \sqrt{y^2 + z^2}. \quad (\text{A2.1})$$

Using the coordinates  $\vartheta \in [0, \pi/2]$  and  $\phi \in [0, 2\pi]$ ,  $y$  and  $z$  can be specified in spherical coordinates

$$y = R \sin \vartheta \sin \phi \quad (\text{A2.2})$$

$$z = R \cos \vartheta. \quad (\text{A2.3})$$

The projection length can be expressed by Equation A2.4.

$$R' = R \sqrt{\sin^2 \vartheta \sin^2 \phi + \cos^2 \vartheta} = R \sqrt{1 - \sin^2 \vartheta \cos^2 \phi}. \quad (\text{A2.4})$$

The average distance between the needle tip and the projection points can be derived as the average projection length according to Equation A2.5.

$$\bar{R}' = \frac{\int_0^{\pi/2} \int_0^{2\pi} R' d\phi d\vartheta}{\int_0^{\pi/2} \int_0^{2\pi} d\phi d\vartheta} = \frac{R}{\pi^2} \int_0^{\pi/2} \int_0^{2\pi} \sqrt{1 - \sin^2 \vartheta \cos^2 \phi} d\phi d\vartheta. \quad (\text{A2.5})$$

The integral is a complete elliptic integral of the second kind, which cannot be expressed in terms of elementary functions. Therefore, the solution of the integral must be approximated numerically (see, for example, the following Python script).

```
import numpy as np
from scipy.integrate import dblquad

def integrand(phi, theta):
    return np.sqrt(1 - np.sin(theta)**2 * np.cos(phi)**2)

result, _ = dblquad(integrand, 0, 2*np.pi, lambda x: 0, lambda x:
    np.pi/2)

approximation = 1 / (np.pi**2) * result
```

As a numerical solution, an average projection length of  $0.84R$  was determined. Thus, on average, the actual length of the filaments appears to be shorter by 26% in the images due to the projection onto the focal plane of the camera.

### A3 Calibration method of the electrochemical hydrogenperoxide measurement

The electrochemical measurement system used in Chapter A3 for the determination of hydrogen peroxide had to be calibrated when the chip electrode was changed due to the design of the measurement electrodes (in particular the reference electrode made of silver).

First, a  $\text{H}_2\text{O}_2$  stock solution with a concentration of about  $10 \text{ mmol}\cdot\text{l}^{-1}$  was prepared by dilution of a commercialized, stabilized hydrogen peroxide solution (30 %, *Carl Roth*). The exact concentration of the stock solution was determined by titration with potassium permanganate ( $0.02 \text{ mol}\cdot\text{l}^{-1}$ , *Carl Roth*), which was repeated three times. For this purpose, 10 ml of the  $\text{H}_2\text{O}_2$  stock solution was mixed with 4 ml deionized water and 16 ml sulfuric acid (25 %, *Carl Roth*). Potassium permanganate was added until the solution became irreversibly colored. The concentration of hydrogen peroxide,  $c_{\text{H}_2\text{O}_2}$ , was calculated according to the Equation A3.6.

$$c_{\text{H}_2\text{O}_2} = \frac{a \cdot c_{\text{KMnO}_4} \cdot V_{\text{KMnO}_4}}{V_{\text{H}_2\text{O}_2}} \quad (\text{A3.6})$$

$c_{\text{KMnO}_4}$  and  $V_{\text{KMnO}_4}$  are the concentration and volume of the potassium permanganate solution, respectively,  $a = 5/2$  is the conversion ratio of hydrogen peroxide and potassium permanganate, and  $V_{\text{H}_2\text{O}_2}$  is the volume of the hydrogen peroxide solution. The concentration of the stock solution was checked weekly.

To prepare calibration standards, the stock solution was first diluted to a concentration of  $100 \mu\text{mol}\cdot\text{l}^{-1}$  by adding running buffer (cf. Section 3.1), and then the standards with concentrations of (1,2,4,6,8,10)  $\mu\text{mol}\cdot\text{l}^{-1}$  were prepared. The calibration standards were freshly prepared from the stock solution at the beginning of each day of an experiment.

At the beginning of an experiment, a new chip electrode was inserted into the flow chamber of the electrochemical measurement system and the system was rinsed with running buffer to remove air bubbles from the system. Cyclic voltamograms were repeatedly recorded until a stable signal was obtained. The functionality of the chip electrode was checked by measuring whether the characteristic oxidation and reduction current peaks of Prussian blue were present and well defined at a potential of 0.2 V and 0.1 V against a silver reference, respectively<sup>2</sup>.

If the functionality was verified, the calibration of the system was continued. Typical results of a calibration cycle are shown in Figure A3.5. In sequence, each calibration standard was injected at least twice and the reaction current was recorded over time. Such a signal is shown in Figure A3.5(A). Two peaks can be seen in pairs for the two injections for each of the standards. The measurement signal is superimposed by a background current that was approximated with a spline and subtracted from the signal. The result is shown in figure A3.5(B).

Each peak was separated, the pairs averaged, and the result smoothed with a Savitzky-Golay filter. Typical reaction currents are shown in Figure A3.5(C) for all calibration standards. The repeatability of the signals is clearly visible. The peak reaction currents were determined and plotted against the concentrations of the calibration standards (cf. Figure

<sup>2</sup>F. Ricci, and G. Palleschi. *Biosensors and Bioelectronics*, 21(3): 389-407, 2005.

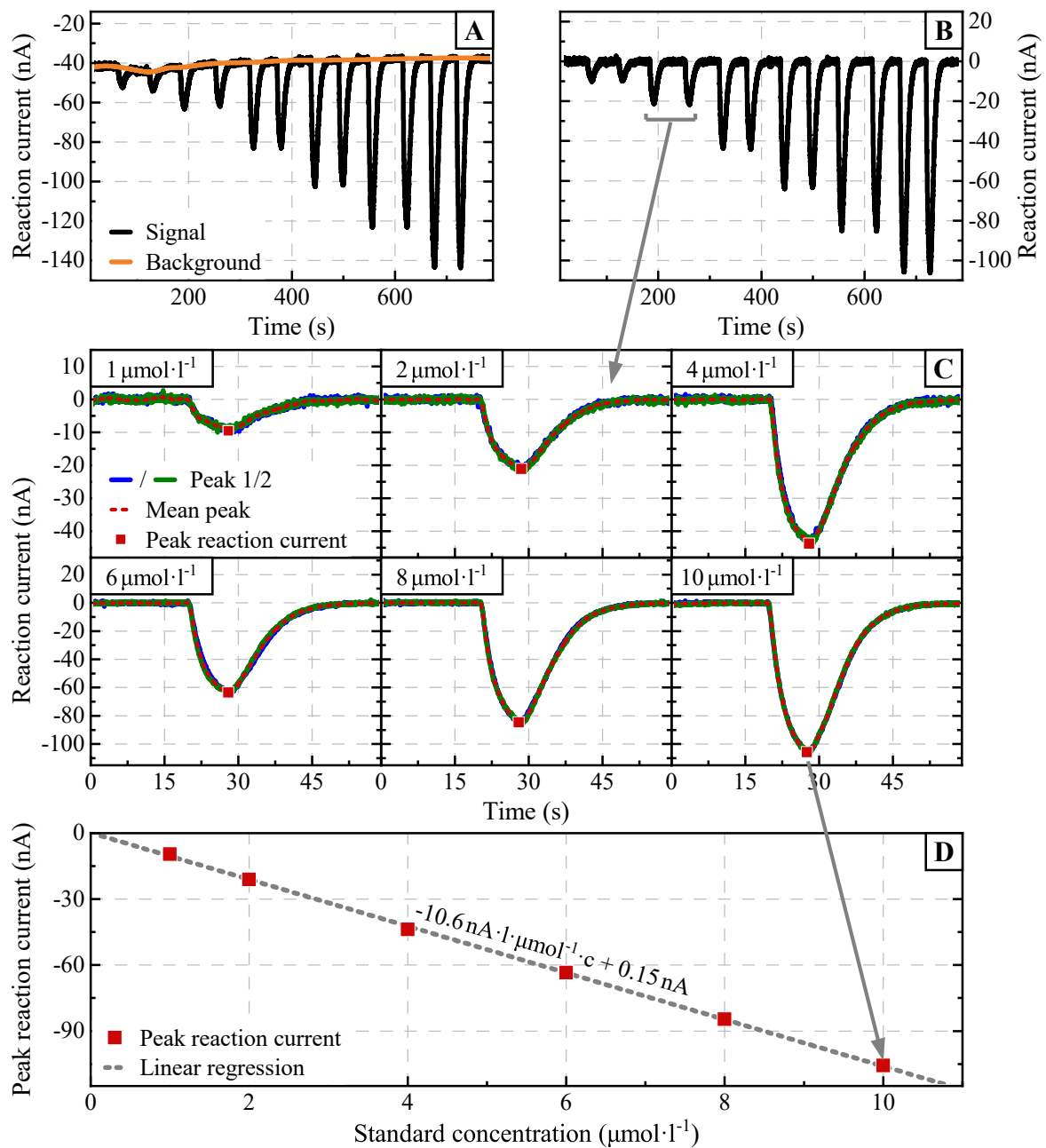


**Abbildung A3.5:** Results of a typical cycle to calibrate a new chip electrode of the electrochemical measurement system. Panel A shows the reaction current obtained after subsequent injection of calibration standards with concentrations of (1,2,4,6,8,10)  $\mu\text{mol}\cdot\text{l}^{-1}$  (each standard was injected twice). The superimposed background current was fitted and subtracted, resulting in the signal shown in panel B. Peak reaction currents were determined for each standard solution as shown in Panel C. The peak currents were related to the respective standard concentration and fitted with a linear function, as displayed in Panel D.

re A3.5(D)). A linear function was fitted to the result and used as a calibration curve for subsequent measurements.

# Curriculum Vitae

## Education

---

2004-2012	General qualification for university entrance at Edith-Stein-Gymnasium Erfurt
2012-2015	Undergraduate studies in technical physics at TU Ilmenau and graduation as „Bachelor of Science“
2015-2017	Graduate studies in physics at University of Greifswald and graduation as „Master of Science“
2017-2023 (exp.)	Doctorate in physics at University of Rostock and Leibniz-Institute for Plasma Science and Technology (INP)

## Professional Experience

---

2014-2017	Research assistant at TU Ilmenau, University Greifswald, Max-Planck-Institute for Plasma Physics Greifswald and Leibniz-Institute for Plasma Science and Technology (INP)
since Nov. 2017	Scientist at Leibniz-Institute for Plasma Science and Technology (INP)

## Teaching Assistance

---

2015-2017	PHYSICS LAB CLASS, University of Greifswald
2016-2017	MATHEMATICAL SEMINAR, University of Greifswald

Rostock, 14. September 2023

.....  
Raphael Rataj



**Erklärung gemäß § 4 Absatz 1 Buchstaben g und h der Promotionsordnung der  
Mathematisch-Naturwissenschaftlichen Fakultät der Universität Rostock**

Hiermit versichere ich, Raphael Rataj, dass ich eine Dissertation zum Thema "*Physical and Chemical Characterization of Nanosecond Pulsed Streamer Discharges in Water*" an der Mathematisch-Naturwissenschaftlichen Fakultät der Universität Rostock angefertigt habe. Dabei wurde ich von Herrn Prof. Dr. Jürgen F. Kolb betreut.

Ich gebe folgende Erklärung ab:

1. Die Gelegenheit zum vorliegenden Promotionsvorhaben ist mir nicht kommerziell vermittelt worden. Insbesondere habe ich keine Organisation eingeschaltet, die gegen Entgelt Betreuerinnen/Betreuer für die Anfertigung von Dissertationen sucht oder die mir obliegenden Pflichten hinsichtlich der Prüfungsleistungen für mich ganz oder teilweise erledigt.
2. Ich versichere hiermit an Eides statt, dass ich die vorliegende Arbeit selbstständig angefertigt und ohne fremde Hilfe verfasst habe. Dazu habe ich keine außer den von mir angegebenen Hilfsmitteln und Quellen verwendet und die den benutzten Werken inhaltlich und wörtlich entnommenen Stellen habe ich als solche kenntlich gemacht.

Rostock, 14. September 2023

.....  
Raphael Rataj





# Acknowledgment

An dieser Stelle möchte ich allen Personen danken, die direkt oder indirekt einen Teil zur Entstehung dieser Arbeit beigetragen haben.

Meinem wissenschaftlichen Betreuer Prof. Dr. Jürgen Kolb möchte ich einen besonderen Dank aussprechen. Trotz Ihrer Tätigkeit als Forschungsschwerpunktleiter und als Universitätsprofessor in Rostock fanden Sie immer Zeit für mich und meine Arbeit. Die regelmäßigen Treffen und die konstruktiven Gespräche waren mir ein großer Ansporn und haben mir über alle Herausforderungen geholfen. Auch wenn es manchmal eine zusätzliche Iteration gebraucht hat, habe ich viel für meinen zukünftigen Lebensweg von Ihnen mitgenommen.

Ein besonderer Dank gilt Dr. Hans Höft, der mir als wissenschaftlicher Mentor zur Seite stand. Ohne dein stetiges Hinterfragen meiner Experimente, deine Ideen zur Datenanalyse und deinen peniblen Blick für wissenschaftliche Konventionen wäre ich nicht zu dem Wissenschaftler geworden, der ich heute bin.

Der Arbeitsgruppe am Leibniz Institut für Plasmaforschung und Technologie in Greifswald sei an dieser Stelle ebenfalls gedankt. Vor allem Katja Zocher, Marcel Schneider und Tilo-Schulz wurden unserer Zusammenarbeit niemals müde. Ihr habt mich nach allen Kräften unterstützt und meine Arbeit vorangebracht.

Ich möchte insbesondere meiner besseren Hälfte Katharina für jeden Moment des Zuspruchs danken. Ohne die Kraft, die ich durch dich gewinnen konnte, wäre diese Arbeit nicht realisierbar gewesen. Für die zahllosen Stunden des geduldigen Zuhörens, für das beständige Aufmuntern und für die wunderbaren Ratschläge kann ich dir nicht genug danken.

Meinen Eltern, meinen beiden Schwestern und meiner Verwandtschaft gehört ebenso mein tiefer Dank. Durch euren Halt, Zuspruch und eure Unterstützung habt ihr diese Arbeit trotz der großen räumlichen Entfernung erst ermöglicht.

Zuletzt gilt auch meinen Freunden ein großer Dank. Zum Teil seit der Schulzeit haben mich unsere gemeinsamen Mittagessen, gemütlichen Abende, Kaffeepausen sowie die vielen besonderen Erlebnisse motiviert und waren mein Ausgleich in vielen Situationen.